THE UNIVERSITY OF CALGARY

THE ORIGIN OF THE ENIGMATIC BEAVER RIVER SANDSTONE

by

Brian Wing Bun Tsang

A THESIS

SUBMITTED TO THE FACULTY OF GRADUATE STUDIES

IN PARTIAL FULFILMENT OF THE REQUIREMENTS FOR THE

DEGREE OF MASTER OF SCIENCE

DEPARTMENT OF GEOLOGY AND GEOPHYSICS

CALGARY, ALBERTA

MARCH, 1998

Abstract

This thesis was undertaken with the goal of determining the origin of the Beaver River sandstone (BRS). The areal distribution of the BRS in the study area has a general north-south trend, and, if found, is always near the McMurray-Waterways contact. The matrix is composed of authigenic euhedral and subhedral microcrystalline quartz grains and a later phase of pore-filling anhedral quartz. Petrographic textures suggest *in situ* dissolution of both framework and microcrystalline quartz occurred. Textures also suggest episodic silica precipitation. Various analytical techniques were employed to determine the bulk rock and trace element geochemistry of the BRS. Thermodynamic equilibrium calculations of H_2S solubility using the method of Barta and Bradley (1985) were incorporated into a SOLMINEQ88 (Kharaka et al., 1988) model. Depending on salinity, 800 to 3300 mg/L of quartz can be dissolved by effervescing H_2S, through the reaction:

$$SiO_{2(s)} + 2H_2O + HS^-_{(aq)} \rightleftharpoons H_3SiO_4^-{}_{(aq)} + H_2S_{(g)}\uparrow.$$

Acknowledgements

I am greatly indebted to the many people who helped me throughout this study. I would like to thank all the people at the Geological Survey of Canada in Calgary. In particular, I would like to mention the following people: Daniel Lebel and Ron DaRoza for their help with getting me set up on MICROSTATION and their unfailing support when things went wrong; Steve Hinds for taking the time to help me make my map look like a map; Jenny Wong for all the time she spent with me on the SEM gathering a multitude of images; Vern Stasiuk for the help with the UV light microscopy; Glen DePaoli for being there to show things to; Brad Gorham, Bob Davidson, Jenny Wong (again), and Al Heinrich for their help gathering the analytical data; John McIsaac, Edward Lau, and Jo McClosky for their support with all the literature searches; Graham Lai, David Rose, and Ken Nairn for helping me keep my computer up and running. I would also like to thank the GSC-Calgary and NSERC for providing financial support throughout the study.

To my parents Peter and Irene, my sister Denise, and my wife Michele.

Table of Contents

List of Tables

List of Figures

List of Plates

Cleavage, bedding, plunge and thrust...

That's what geology's all about.

Anonymous

Chapter 1. Introduction

Early geological investigations of the area surrounding the confluence of the Athabasca and Clearwater Rivers were primarily directed at assessing the vast resources of the Athabasca tar sands (e.g. McConnell, 1891; McLearn, 1917; Ells, 1936). These early investigators described the McMurray Formation as typically bitumen saturated sand with local calcite or clay cement, while some areas being totally devoid of all bitumen. Other types of cements are reported only in passing. For example, a quartz cemented sandstone was reported by McConnell (1891), but he originally believed it to be a knoll of the Precambrian shield jutting up through Paleozoic sediments. Carrigy (1959) correctly identified the quartz cemented sediment as Cretaceous in age. Later investigators devoted more interest to the quartz cemented sand, but the study was focused towards an archeological interest (e.g. Fenton and Ives, 1990) and no work was aimed at determining the cause of the cementation. They named it the Beaver River sandstone (BRS), after studying an exposure near the Beaver River, Alberta. The Beaver River sandstone can be found in the area surrounding the confluence of the Muskeg and the Athabasca rivers, as shown by Fenton and Ives (1990, their Figure 11).

Although Fenton and Ives (1990) have successfully demonstrated the relationship of the BRS with the host McMurray Formation, there has not been an in-depth study regarding the origin of the Beaver River sandstone. This is the purpose of this study. The anomalous nature of the microcrystalline quartz cement brings several questions to the forefront. What is the nature of the microcrystalline cement found in the BRS? How

and/or why does silicification occur? Where is the Beaver River sandstone localized? Questions such as these can be answered by an in-depth study of the BRS.

1.1. Objectives

The objective of this thesis is to use field, laboratory and experimental calculations to determine the origin of the BRS. Geological mapping and field sampling was conducted to determine the distribution of the BRS, the thickness, and the upper and lower contacts. These aspects are critical in determining how the silicified sediments are related to the unsilicified McMurray Formation proper, as well as the underlying Devonian limestone. If a relation can be determined, a mechanism can be invoked to explain the relationship.

Petrographic examination of the BRS was done using optical microscopy and SEM to determine the nature of the microcrystalline matrix. The relations between textures are used to develop the paragenetic sequence for silicification of the Beaver River sandstone.

Analytical geochemistry was included to fully characterize the mineralogy, whole rock and trace element geochemistry of the BRS. Mineralogy was determined using optical microscopy, SEM, and XRD. Whole rock geochemistry was determined chiefly through XRF. Trace element geochemistry was out-sourced to external analytical laboratories for fire assay (FA-DCP), neutron activation (INAA), and total digestion inductively coupled plasma-mass spectroscopy (ICP-MS). In-house methods used for

trace element geochemistry included laser ablation-inductively coupled plasma-mass spectroscopy (LA-ICP-MS), total digestion ICP-MS, ion liquid chromatography (ILC), Rock Eval., and LECO-Sulfur. The results of these various analytical techniques help in developing a greater understanding of the chemical processes that may have contributed to the silicification of the BRS.

A review of the literature was done to determine whether other units similar to the BRS are known elsewhere. However, simply demonstrating similar physical characteristics between the BRS and another deposit already described in the literature is not sufficient to propose a similar classification for both deposits. It must be demonstrated that both types of deposits have similar mechanisms of formation. If this is not possible, then the BRS must be considered a unique deposit.

1.2. The study area

The study area is located approximately 50 km north of Ft. McMurray, near the confluence of the Muskeg and Athabasca rivers (Figure 1.1). Generally, the area is marshy, swampy and low-lying with poor surface drainage. The Muskeg River valley has steep banks about 20 meters high near its mouth with excellent exposures of Devonain Waterways Formation limestone. The area is generally accessible by vehicle except at the north end of the study area, east of the Muskeg River.

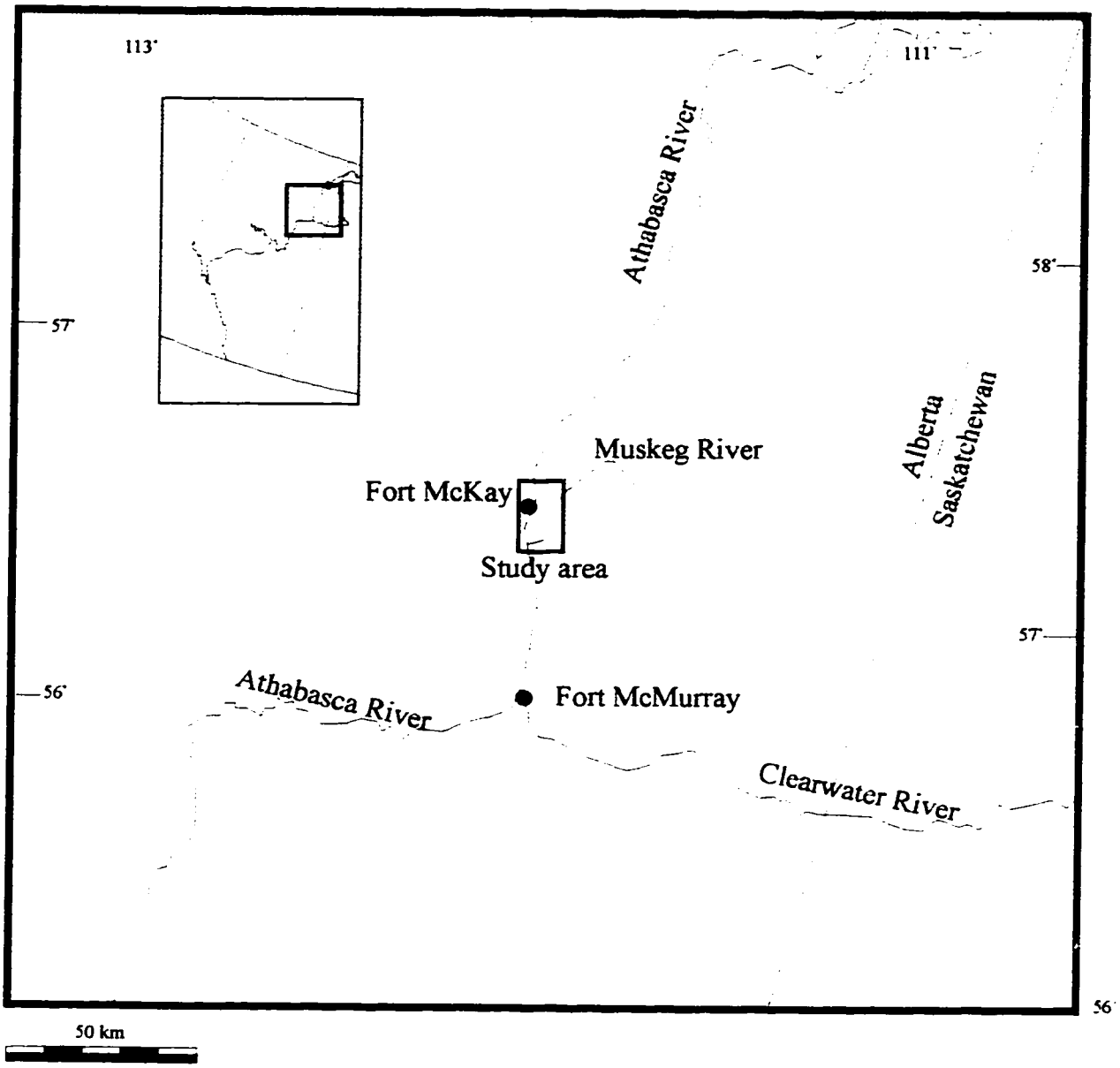

Figure 1.1. Location of study area.

Chapter 2. Geology of the Study Area

2.1. Geological Setting

2.1.1. Basin Evolution

2.1.1.1. Western Canada Sedimentary Basin

The study area is located near the eastern erosional edge of the Western Canada Sedimentary Basin (WCSB). Two main stages of tectonic evolution are important in the development of the WCSB: a Late Proterozoic to Middle Jurassic miogeocline-platform stage and a mid-Jurassic through Tertiary foreland basin stage.

The first stage has been correlated to continental rifting and Late Proterozoic through Early Mesozoic drifting associated with the creation of a passive margin along the western margin of the North American craton. Following this, Mesozoic through Tertiary deformation caused the formation of the Cordilleran mountain belt in response to subduction and accretion of oceanic terranes at the western margin of the North American plate. Uplift and erosion of the neoformed mountain belt provided sediment that accumulated in the foreland basin, part of which was uplifted and eroded. Deformation of the foreland fold and thrust belt terminated prior to crustal extension during Early and Middle Eocene (Price, 1994).

2.1.1.2. Peace River-Athabasca Arch

A number of structural features of crustal magnitude occur within the WCSB, one of which is the Peace River Arch (PRA). The PRA is a northeasterly trending structure that crosses the WCSB from the Alberta-B.C. border to near the fourth meridian in the east (Figure 2.1). O'Connell (1994) described the geological history of the Peace River Arch. The PRA was a high during Lower to Middle Devonian deposition of the Elk Point Group. It remained elevated in the early Late Devonian until the end of Slave Point deposition. Tectonic inversion of the Devonian arch was accompanied by general subsidence to the northwest and southeast of the arch, with differential subsidence having ceased by the end of the Devonian. Maximum subsidence occurred north of the crest of the arch. By the beginning of the Carboniferous, the PRA was no longer emergent. In the west, collapse occurred as a series of linked grabens, forming the Peace River Embayment. During the Permian, the embayment became broader and more tectonically stable. By the Triassic the feature had developed into a low-relief embayment, with local renewed subsidence of underlying graben structures that formed during Carboniferous time. Finally, Late Jurassic and Cretaceous time marked a period of regional loading and subsidence. Stelck (1975) suggested that the PRA extends eastward towards the study area. Control of sedimentation patterns by structures related to the PRA is suspected in the study area, and is likely related to evolution of the Peace River Arch.

The results of a recent high resolution aeromagnetic survey over the eastern end of the PRA by Birch Mountain Resources Ltd. show that the basement surface is highly

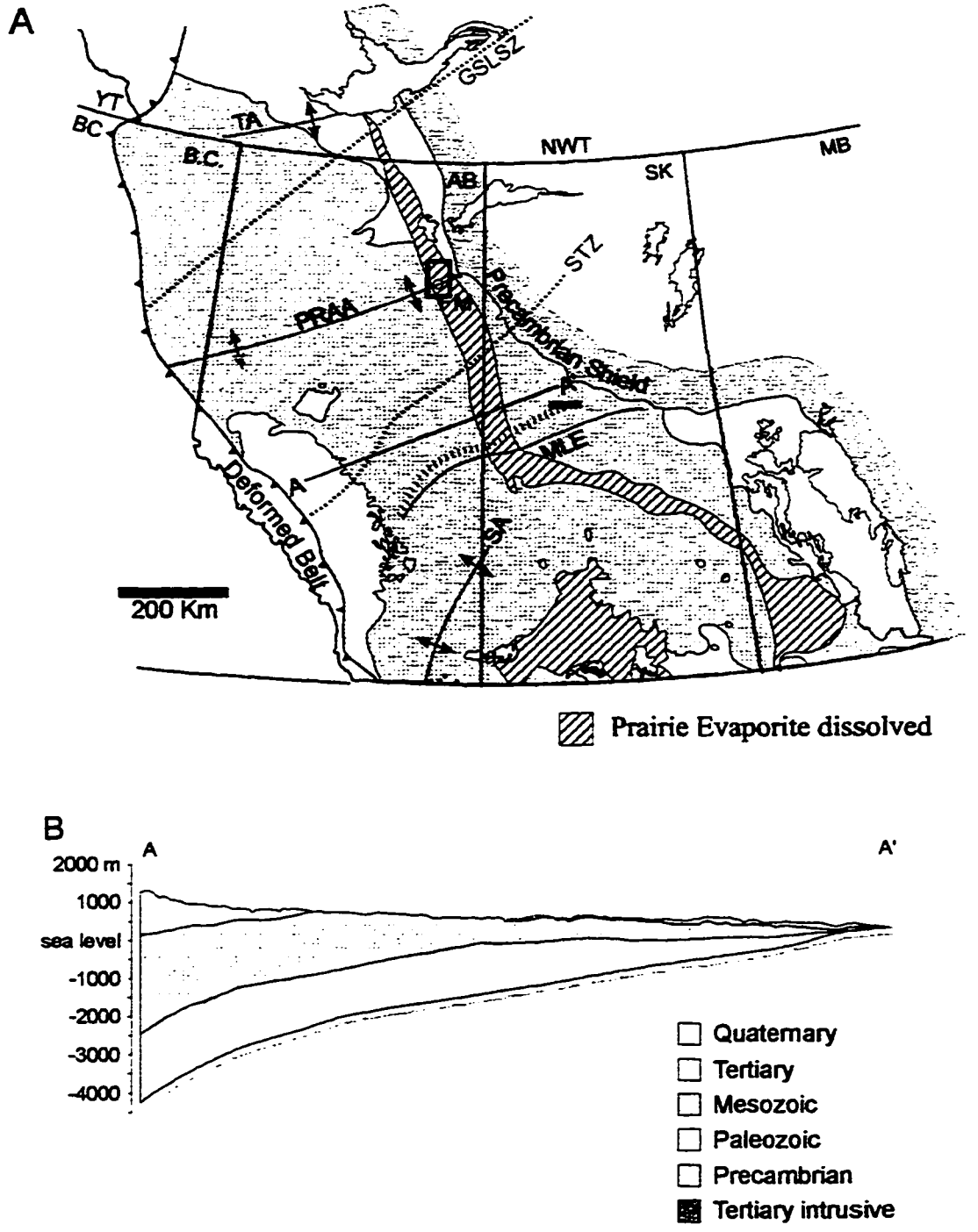

Figure 2.1. (A) The axis of the Peace River-Athabasca Arch and the salt dissolution edge coincide around the area surrounding the study area. (B) Cross section of the Western Canada sedimentary basin. TA = Taltson Arch; PRAA = Peace River-Athabasca Arch; GSLSZ = Great Slave Lake Shear Zone; STZ = Snowbird Tectonic Zone; SA = Sweetgrass Arch.

irregular in this area, possibly as a result of graben development involving basement structure along the eastern extension of the arch (H. Abercrombie, personal communication, 1997).

Benthin (1973) remarks on a northeast trending feature in northeastern Alberta, which he called the "Athabasca Arch". He presents a convincing argument that the feature is related to a tectonic arch, rather than a thinning of the strata due to salt collapse. The present day salt dissolution edge of the Prairie Formation has a similar trace to the Sewetakun Fault, a major northwest to north trending basement structure described by Hackbarth and Nastasa (1979).

Dufresne et al. (1994) suggest that reactivation of basement faults associated with uplift of the Peace River-Athabasca Arch likely occurred during the Late Devonian. Reactivation of the faults might explain the extremely complex Devonian erosional surface in the vicinity of Fort McKay, which is characterized by north, northeasterly, and northwesterly trending paleo-valleys and paleo-ridges.

2.1.2. General Stratigraphy

The stratigraphy of the study area has been described by Carrigy (1959) and Norris (1963) and recently by Cotterill and Hamilton (1995). Figure 2.2 shows a general stratigraphic column. The basement rocks are early Proterozoic granitoids of the Taltson magmatic arc (Ross and Stephenson, 1989). Basement is unconformably overlain by the Basal Red Beds, which are arkosic sandstone and conglomerate of Lower Devonian age.

The Basal Red Beds form the earliest deposits of the Lower to Middle Devonian Elk Point Group and conformably underlies the Beaverhill Lake Group. A major unconformity separates the Devonian Beaverhill Lake Group and the Cretaceous McMurray Formation of the Mannville Group.

Sherwin (1962) subdivided the Elk Point Group into lower and upper subgroups. Only the Contact Rapids Formation of the Lower Elk Point Group is found in the study area. These rocks are composed of dolomitic shale at the base, and grade to a grey to green, argillaceous dolostone at the top. The Winnipegosis, Prairie, and Watt Mountain formations of the Upper Elk Point Group subcrop in the study area. The Winnipegosis Formation, the equivalent of the Keg River Formation to the west and the Methy Formation to the east, is a tan, vuggy, reefal dolostone succession. Salt, anhydrite, and gypsum interbedded with carbonates and shales characterize the Prairie Formation. The Watt Mountain Formation disconformably overlies the Prairie Formation and conformably underlies the Beaverhill Lake Group. The Watt Mountain Formation is composed of distinctive, dolomitic shales, and, along with the Contact Rapids Formations, serve as a useful stratigraphic datum (Cotterill and Hamilton, 1995).

The Beaverhill Lake Group consists of the conformable Fort Vermillion, Slave Point and Waterways Formations. The Fort Vermillion Formation is a white or bluish-white anhydrite and dolomite and is absent in some areas (DePaoli, 1996). The Slave Point Formation is a pale brown to dark brown limestone, with interbedded dark brown shale laminae. The Waterways Formation is described in more detail in the following

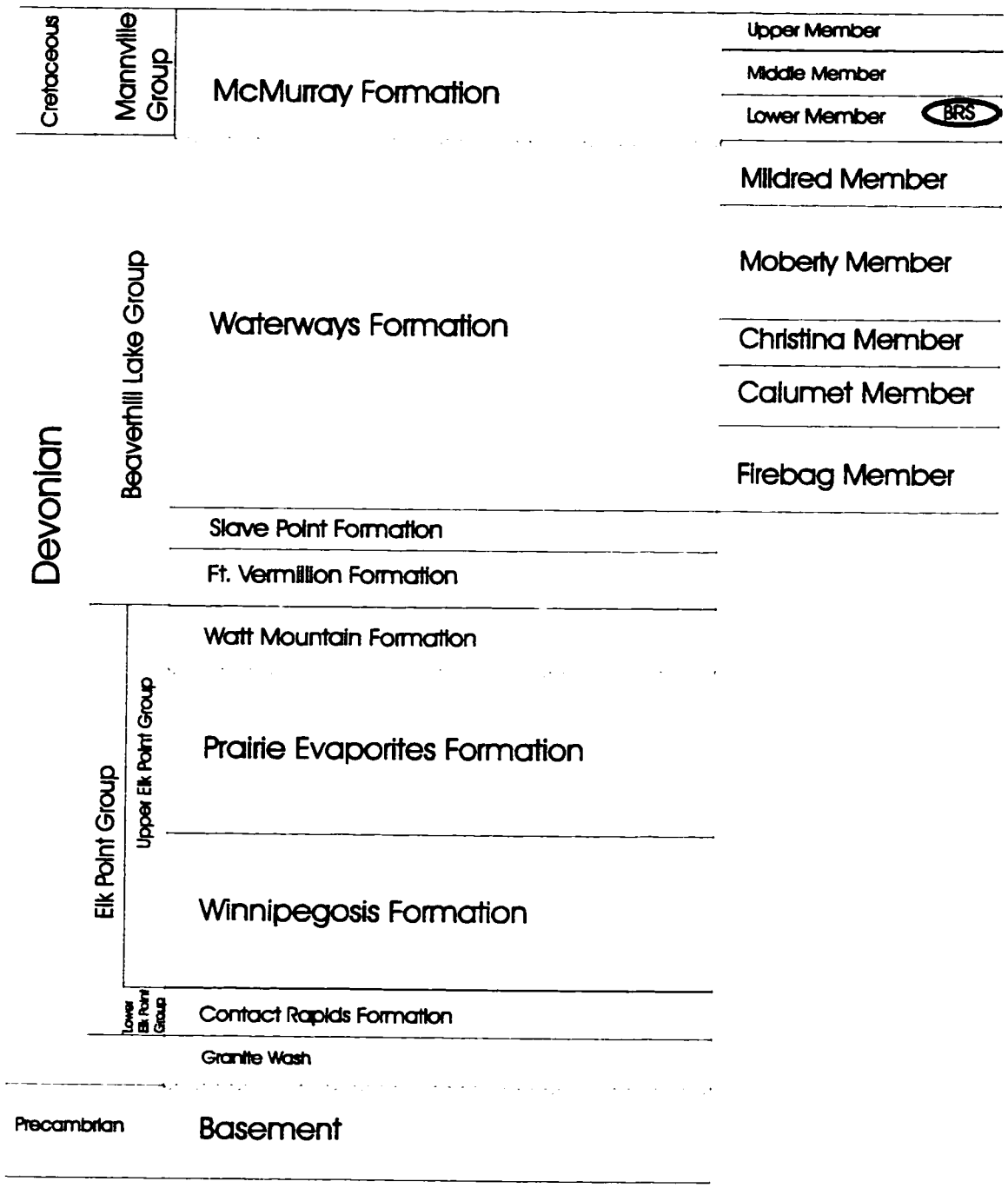

Figure 2.2. Stratigraphic column of the study area. The Beaver River sandstone (BRS) is not a formation. It is a microcrystalline quartz cemented sandstone withing the lower member of the McMurray Formation. The BRS is not shown as a sedimentary facies since it is not derived through sedimentary processes.

section, but is generally a light grey to light green grey argillaceous limestone to limey shale.

Sandstone of the Cretaceous McMurray Formation was deposited on a major unconformity surface developed on the surface of Devonian rocks within the study area. Flach and Mossop (1985) state that the McMurray Formation was deposited in a north-south trending depression caused by the removal of Devonian aged evaporites resulting in the collapse of younger sediments. The McMurray Formation is generally of uniform, quartzose lithology, with subordinate shaly interbeds. The sandstone is generally massive to thickly bedded and cross-bedded, but is never thinly bedded. The McMurray Formation is described in more detail in the following section.

2.2. Local stratigraphy

2.2.1. Waterways Formation

Crickmay (1957) and Norris (1963) described Devonian stratigraphy in the study area. Crickmay differentiated the Beaverhill Lake Formation into five members through field description and fossil content. Overall, the Waterways Formation is an alternating sequence of calcareous shale, argillaceous limestone and limestone. This formation can be fairly resistant to weathering, and forms steep cliff faces along the banks of the Muskeg River (Plate 2.1). The various members of the Waterways Formation were not

differentiated during mapping. Norris (1963) indicates that the Moberly and Christina members underlie the study area.

The upper erosion surface of Waterways Formation carbonates in the study area contains a number of rock types that are not representative of the Waterways Formation. These include a green shale of variable thickness developed on the surface of limestone and sulfide nodules found in a borrow pit near the mouth of the Muskeg River. During the field season of 1994, a trench was dug in a gravel pit near the mouth of the Muskeg River on the East Side of the Athabasca River, locally known as the Richardson Pit (Plate 2.2). This trench was approximately 10 m long x 3 m wide x 5 m deep. A 1.5 m thick layer of massive, decalcified greenish grey clay was observed at a depth of approximately 3 meters and is underlain by a rusty red weathering limestone. Although the limestone was not rusty when first excavated, the rock had weathered to its characteristic rustiness by the following field season. The green clay is a greasy, sticky ooze when wet, but is a hard, friable material when dry.

Cobble and coarse gravel sized marcasite and pyrite nodules were collected as float in a borrow pit near the mouth of the Muskeg River. They were easily differentiated from the limestone float by their characteristic hematitic-goethitic weathering. When exposed at the surface, the marcasite nodules weather to a bright orange-rust colour, whereas the limestone weathers to a buff yellow colour. Extreme weathering of marcasite clasts results in a residual pile of powdery, bright orange oxide. One sample assayed 400 ppb Au (H. Abercrombie, personal communication, 1997).

2.2.3. Pre-McMurray unit

Subangular to rounded, poorly sorted, quartz-rich coarse sand to coarse pebble, sandstone is found locally in the study area and the surrounding area. Generally these clasts are found in isolated layers scattered throughout the area and are always near the pre-McMurray-Devonian contact. These pockets are typically capped by a sulfide cemented, sideritized limestone pebble lag, suggesting a probable erosion surface. Although the McMurray Formation has various lithologies that traditionally have been homogenized as single members, this coarse quartz grained sand to conglomerate may have been deposited prior to the McMurray Formation proper (Carrigy, 1973; Cant and Abrahamson, 1996).

A quartz cemented unit is commonly given a pre-McMurray distinction in the literature (e.g. Dufresne et al., 1994; Cant and Abrahamson, 1996). It is necessary to distinguish these two units: there exists a coarse grained, angular to rounded, poorly sorted unit at the base of the McMurray Formation. This is the pre-McMurray unit proper. The quartz cemented unit should not be considered as part of the pre-McMurray unit. Rather, it is the Beaver River sandstone, which occurs within the lower member of the McMurray Formation.

2.2.3. McMurray Formation

McMurray Formation sands were deposited on an undulating pre-Cretaceous unconformity surface (Carrigy, 1973). The oldest McMurray sediments filled topographic lows and were subsequently covered by younger, essentially flat-lying sediments. However, the discussion in the previous section suggests that some of the depressions on this unconformity surface may have been infilled by sediments that predate the McMurray Formation proper.

Carrigy (1959) differentiated the McMurray Formation into the lower, middle and upper members. From the descriptions given, it is unclear whether or not the pre-McMurray unit discussed in the previous section is equivalent (or not) to the lower McMurray member of Carrigy (1959) since many unconformities exist within the formation. The lower member is a poorly sorted, lenticularly bedded conglomerate and sandstone, with local interbeds of finer grained shale and silt. This appears to be distinct from the sideritized limestone pebble lag that overlies the pre-McMurray unit. The top of the lower member is a black or dark-grey carbonaceous shale in most places, and contains wood fragments. The middle member is a quartz sand of uniform mineralogy that contains lenticular interbeds of finer grained silts, shales, and clays. Current bedding, plant remains, trace fossils and oil-impregnated woody material characterize the middle McMurray member. The upper member is similar to the middle member, except that the upper member is generally horizontally bedded.

Carrigy (1959) found various types of cements in the McMurray Formation. The major cement is obviously tar. Some areas can be devoid of bitumen, whereas other areas are either bitumen stained or fully bitumen saturated. Carrigy (1959) reported other cements found in the McMurray Formation include calcite, clay, iron (siderite and hematite and pyrite), and silica. Carrigy (1966) later reported an iron oxide cement in what he called a pre-McMurray(?) unit. He also reports the presence of silica cemented sandstone within the study area, and suggests a common origin for both the iron oxide cement and the silica cement. It is indeed this silica cemented unit which is the main focus of this thesis.

During field investigations, parts of the McMurray Formation were found to contain iron oxide (hematite), iron carbonate (siderite), or iron oxyhydroxide (goethite) cement. The lithology of these rocks ranges from silt, to very fine grained sand, to a well rounded, coarse grained sand. Abercrombie and Feng (1997) considered the iron bearing (siderite cemented) McMurray Formation as an iron rich Beaver River sandstone. The two lithologies are distinguished in this study, and only the silica cemented McMurray Formation is considered as true BRS.

2.2.4. Beaver River sandstone

The Beaver River sandstone (BRS) has been investigated by workers who were interested in finding the source for the rocks used by aboriginal North Americans to make arrowheads (Fenton and Ives, 1982, 1984, 1990; Ives and Fenton, 1983, 1985).

The BRS is not a formation. Rather, it is what Fenton and Ives (1982) call the rock that formed as a result of anomalous microcrystalline quartz cement found within the McMurray Formation. Although they report the cement occurs near the top of the lower member, recent unpublished data (G. DePaoli, personal communication, 1998; Table 2.1) shows that quartz cemented McMurray Formation can be found directly overlying Devonian limestone of the Waterways Formation. The BRS was found to contain root molds, coal laminae, and has a highly variable lithology which is characteristic of the lower member (Fenton and Ives, 1990). Fenton and Ives (1984) report finding oil sands both underlying and overlying the BRS in outcrop.

In outcrop, the BRS is a light to dark grey, silicified sandstone of variable thickness. Where it is thick (> 1 m), outcrop is characterized by massive, angular to rounded boulders that are usually vertically jointed. If it is poorly exposed or is thin, BRS outcrop is found as a flat lying, continuous rock floor. A sharp ring results from striking the rock with a hammer, as opposed to the dull thud that sounds when striking tar cemented McMurray sand. BRS outcrop is often found as a resistant cap on sandy knolls that rise above the surface of the swamps (Plate 2.3). The study area has many of these sandy knolls that rise up above the swamp, but few of them actually have a cap of BRS. Sandy knolls can be easily found (although are not necessarily easily accessible) while struggling through the swamp by finding the characteristic birch trees that grow on these well drained topographic highs. These areas often have a white to yellowish coloured moss covering the floor of the clearing, which is characteristically bright white in aerial photographs (Plate 2.3).

Table 2.1. Unpublished data of quartz cemented McMurray Formation in the Syncrude Aurora Mine (G. DePaoli, personal communication, 1998)

Hole #	Location	Depth (m)	Description
AA/13-16-96-9W4	475300E, 6354500N	122.55-128.20	Interbedded pyritic quartz, calcareous quartz, and pyritic, calcareous, quartz cemented sand.
AB/13-1-96-11W4	460600E, 6352400N	113.35-113.40	3 cm quartz cemented sand underlain by 2 cm pyrite cemented sand.
AB/5-9-96-10W4	465400E, 6352400N	135.26-135.40	3 to 4 cm thick interbedded pyrite and quartz cemented sand.
AB/7-11-96-10W4	469700E, 6352100N	77.35-77.75	Calcareous quartz cemented sand with heavy bitumen staining.
AC-5-12-96-10W4	470343E, 6352225N	111.50-112.30	Calcareous quartz cemented sand.

The BRS is a massively bedded, fine to coarse grained, microcrystalline quartz cemented quartz sandstone. It is characterized by poor sorting, with both well rounded and angular grains. Though sedimentary structures such as cross bedding have been observed in the BRS, they are not common. Organic material is present in low amounts in the BRS, but the content varies from sample to sample. The variation in light and dark colouring is due to a heterogeneous distribution of the bitumen, giving the rock a coarsely mottled appearance (Plate 2.4). A more detailed petrographic description of the BRS is presented in Chapter 3.

There is often a sharp contact between the silica alteration and the underlying oil sands (Plate 2.3). However, the BRS is not always found in contact with bitumen cemented sands. When found capping sandy knolls, the base of the BRS is often

observed, but the surrounding sand is typically unconsolidated and is believed to be the weathering product of previously tar impregnated sand.

2.3. Mapping

2.3.1. Distribution of the Beaver River sandstone, and the McMurray and Waterways Formations

In order to delineate possible outcrop areas of the BRS, Fenton and Ives (1990) used subcrop maps of the Waterways Formation, the McMurray Formation and overburden thicknesses to show that the BRS is likely to be found on both sides of the Athabasca River in the area surrounding Ft. McKay. However, as will be discussed below, they make a note that the distribution of the silicified McMurray Formation is discontinuous, and that the distribution of these silicified zones could not be predicted (Fenton and Ives, 1990).

Mapping results are shown in Figure 2.3. It is apparent that BRS outcrop is not common, and that outcrop is scattered throughout the study area. The BRS is found in a north-south trend that is approximately 1 km in width between Highway 63 and the Muskeg River. The northern limit of BRS exposure occurs along 6340250N, which coincides with the east-west cut line for power and pipeline. BRS samples taken north of this limit probably are not outcrop, and are more likely to be float boulders.

It is important to note that the distribution of BRS outcrop is highly localized. That is, the microcrystalline quartz cement is neither pervasive nor continuous throughout the McMurray Formation. However, interbedded quartz and pyrite cemented intervals near the base of the McMurray Formation have been found in drill cores from the Syncrude Aurora Mine (Table 2.1). A thin interval (less than 30 cm) of silica cemented sand in the McMurray formation was reported in a core drilled in the Birch Mountains, northwest of the study area (S. Sabag, personal communication, 1996).

During field excursions, the thickness of BRS outcrop was measured. The thickness and elevation are shown as bubble plots to appropriately represent the scattered distribution of the outcrop, as shown in Figure 2.4. The thickness of the BRS can vary anywhere from 30 cm to 175 cm thick, with an average thickness of approximately 70 to 100 cm. Generally, it is thicker towards the south and thinner towards the north. The elevation varies through 20 m, ranging from approximately 260 m to 280 m above sea level and an average elevation of 276 m. The outcrop is generally higher towards the north and lower towards the south.

The distribution of the Waterways and McMurray formations was also determined during field studies (Figure 2.3). Exposure is relatively scarce in the study area; the best exposure of limestone is along the banks of the Muskeg and Athabasca rivers. Limestone outcrop can also be found in scattered, isolated areas among the swamps, or in the gravel pits in the study area. Towards the southern region of the study area, Waterways limestones form steep, white to buff colored limestone cliff faces at the tops of the cliffs. The McMurray Formation outcrops towards the north end of the Muskeg River and in

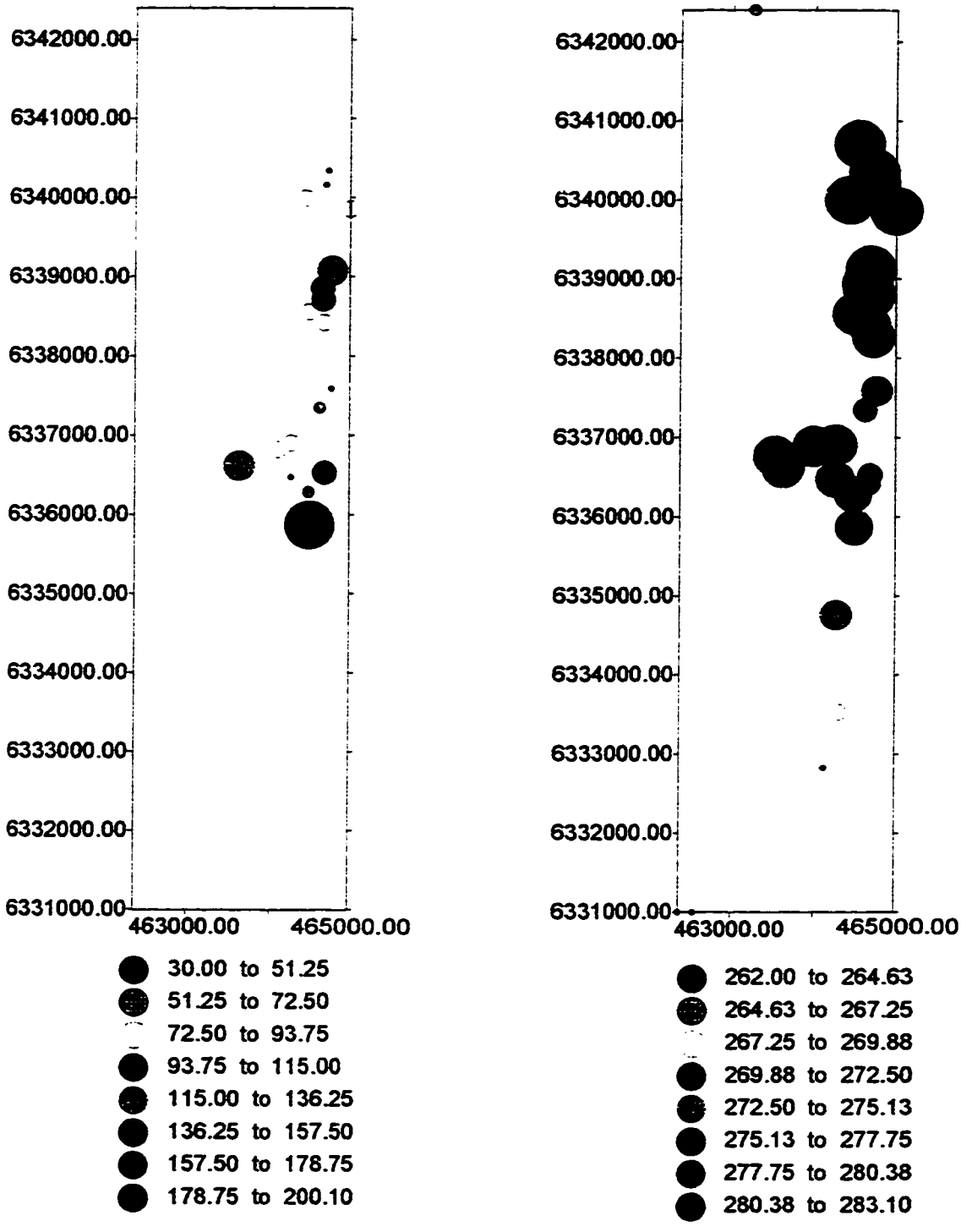

Figure 2.4. Bubble plots of BRS (a) thickness on the left and (b) elevation on the right, both in meters. Axes correspond to northings and eastings. Elevation values were generated using a digital elevation model. Thickness was measured in the field, although not all outcrops visited were measured.

isolated areas in the lower Muskeg River area, as discussed below. Usually, McMurray Formation tar sands are found as isolated knolls in the swamps, or as larger, well-drained sand ridges.

2.3.2. Unusual rock types found in the study area

The green clay found in the borrow pit at the mouth of the Muskeg River (Plate 2.2), immediately east of the Peter C. Lougheed Bridge, was never found as thick elsewhere in the study area. Rather, limestone with faint green discolouring and thin, green clay coatings are occasionally found lining < 1.0 to 1.5 meter high, marcasite-lined (or sideritized in some cases) vertical to contorted, smoothly weathered, subvertical faces (Plate 2.5). Fedikow et al. (1996) describe "solution chimney" structures at the Mafeking Quarry, Manitoba, that have green coloured clay and other physical characteristics that are similar to the features observed in the study area.

The vertical and subvertical features were found mainly at the top of resistant limestone cliffs along the Muskeg River and near the barge landing area on the Athabasca River (462500E 6337450N). These cliffs are hollowed into the cliff face, and have a smooth, dark surface, as though the result of water washing. Occasionally, calcite cemented, medium to coarse grained angular sand grains were found cemented within the "solution chimneys" in the study area.

Conversely, silica concretions in the Mafeking Quarry range from <1 cm diameter up to 60 cm wide and 30 cm thick are intrinsically related to the "solution chimneys"

(Fedikow et al., 1996). The silica concretions in Manitoba require further study, as the relation to the "solution chimneys" has not yet been determined.

Two areas of particular interest are found at 465000E 6332325 N and 465725E 6333450N along the lower end of the Muskeg River. At the southern location, two discrete structures were found hollowed through the height of the limestone cliffs. The walls of the features are wide at the top of the cliff and are angled towards the center at the bottom of the cliff, resulting in an overall funnel shape. These funnel-shaped features are filled with tar cemented sand (Plate 2.6). The structures are as tall as the cliff face, and are not slump features since sedimentary structures have been preserved. Rather, it is suggested to be a large scale "solution chimney" similar to the smaller, one meter tall "solution chimneys".

Carrigy (1959) noted that the limestone strata are prone to warping along the Athabasca River, and he attributed this undulatory nature to structure as a result of dissolution of the underlying evaporite deposits. Near the lower end of the Muskeg River, the limestone strata are also observed having an undulating, domed appearance, suggesting that dissolution likely occurred within the study area. This displacement results in a highly varied elevation for the contact between Cretaceous sandstone and Devonian limestone.

The dipping strata, however, are not the only indication of a highly variable unconformity surface. At one bend in the Muskeg River (6332500N, 465525E), oil sand outcrop is juxtaposed against limestone outcrop at the same elevation (Figure 2.3), instead of occurring above the limestone as would normally be expected. The elevation of the

contact can vary throughout the study area, as shown in cross section (Figure 2.5). In places, surface outcrops of the Waterways Formation occur at higher elevation than nearby outcrops of the McMurray Formation. Although this difference in elevation can be attributed to undulating topography on the pre-McMurray unconformity surface, it is also possible that this variation in elevation is due to faulting of underlying strata.

Plate 2.1. Steep cliff forming limestone outcrop along the Muskeg River. Notice how the beds drop down towards the water level. No strike or dip measurement was possible on these cliffs due to the irregular and highly jointed nature of the outcrop surface.

Plate 2.2. Trench dug in the Richardson Pit. The pit has approximate dimensions of 10 m long x 3 m wide x 5 m deep. The bottom 1.5 m of the pit exposed a thick layer of massive, decalcified green clay. This clay was underlain by a tan limestone which weathered to a bright re-orange colour upon exposure for a period of one to two years. The green clay is a greasy, sticky ooze when wet, but is a hard, friable material when dry.

Plate 2.3. Beaver River sandstone in outcrop

A. 30-40 cm thick BRS underlain by tar cemented, round to angular, poorly sorted sand (Lower member of the McMurray Formation). BRS outcrop is found as a weathering cap protecting the underlying tar sand. The tar sand is a knoll rising above the surrounding swamp.

B. Close up of A.

C. Similar to A, where the BRS is acting as a weathering cap for the underlying tar sand.

D. Close up of C. BRS is approximately 15-20 cm thick.

E. BRS outcrop from the same sandy knoll as C and D, approximately 50 m distance. Notice the drastic difference in thickness of the silicified unit. The BRS here is up to 80 cm thick and the sandy knoll is approximately 3 m high.

F. Beaver River sandstone in outcrop, approximately 80 cm thick.

Plate 2.3

A

B

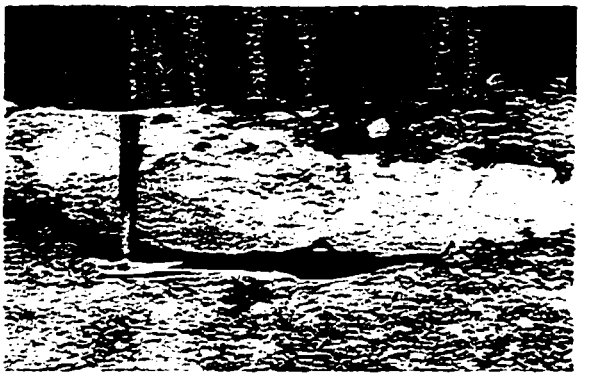

C

D

E

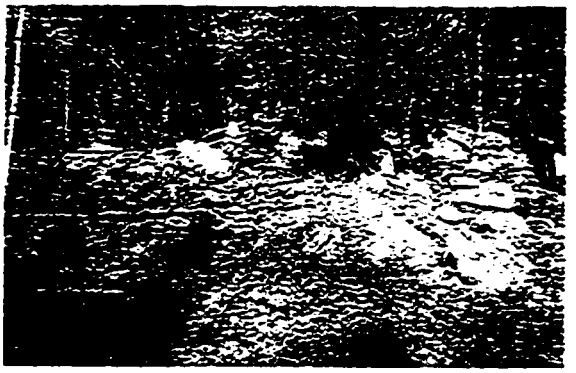

F

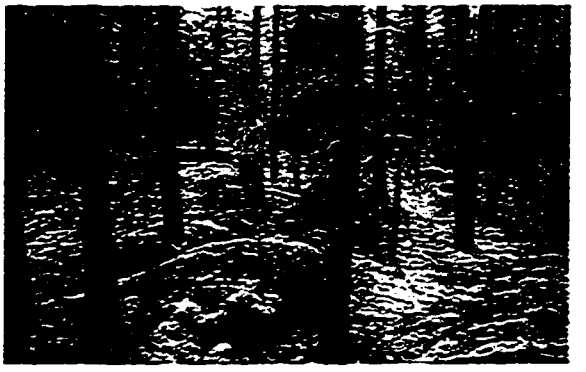

Plate 2.3. (Cont.) Beaver River sandstone in outcrop

G. Although not commonly present in the BRS, cross bedding is occasionally observed. Bedding is usually not present in the BRS; usually it has massive textures, with the detrital framework grains chaotically arranged.

H. White to yellowish coloured moss covering the floor of sandy knolls scattered throughout the swamps in the study area; reportedly named "Cladina" lichen.

Plate 2.3 (cont.)

G

H

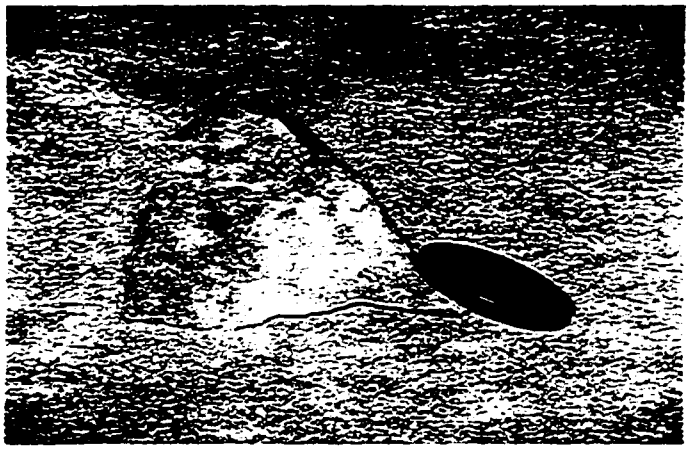

Plate 2.4 Hand sample of BRS showing coarsely mottled colouring.

Plate 2.5. Vertical "solution chimney" structure in outcrop along Athabasca River, just south of the barge landing site on the east bank of the Athabasca River (UTM 462500E 6337450N). Notice the rust stained surfaces along the walls of the feature. This is characteristic of "solution chimney" structures in the study area, as well as similar "solution chimney" structures in the Dawson Bay, Manitoba, area as described by Fedikow et al. (1997). Hammer for scale.

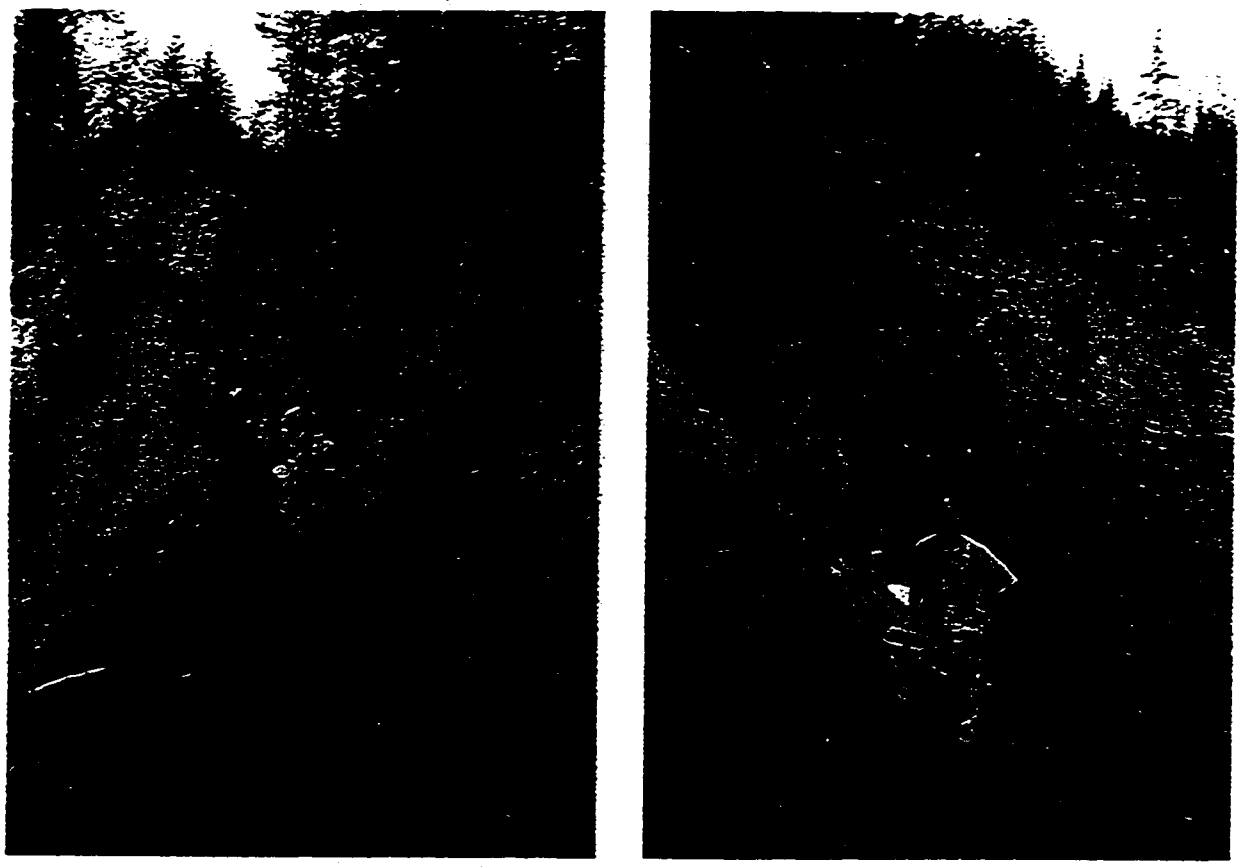

Plate 2.6 Tar sand filling in solution structure. Plate shows the same in-filled structure viewed from different angles.

Chapter 3. Mineralogy and Petrography

3.1. Petrography

Initial petrographic investigations of the BRS were conducted by optical microscopy and showed that the BRS was cemented by euhedral microcrystalline quartz. However, because of the very fine grained nature of the cement, the petrographic study of the cement and determination of the paragenetic sequence of the BRS was done mainly by use of a scanning electron microscope (SEM) using the backscattered electron (BSE) detector and energy dispersive x-ray (EDX) detector. One drawback of using the SEM for petrographic analysis is that a mineralogical determination is possible only by inference from the elemental analysis and observed textures. Mineralogy of bulk samples was determined by x-ray diffraction (XRD).

3.1.1. X-ray Diffraction (XRD)

X-ray diffraction data shows that quartz is the major mineral found in the BRS. In fact, other minerals are quite rare, with feldspars and anatase (TiO_2) being the only other minerals found above background levels, and only in trace amounts. No clay minerals were observed in thin section. XRD methods and results are discussed in greater detail in Section 4.1.

3.1.2. General petrographic observations

3.1.2.1. Framework grains

Plate 3.1 shows typical BRS textures observed in thin section. Over 99% of the coarse, fine and microcrystalline grains are composed of quartz. Framework grains are poorly sorted, ranging from angular to well rounded, fine to very coarse grained quartz. Detrital framework grains make up approximately 65-75% of the BRS in thin section, with the remainder of the rock composed of the microcrystalline quartz grains. Some detrital framework grains have inherited, syntaxial quartz overgrowths.

Grain size distribution determined through thin section observation reveals that the framework grains have a bimodal grain size distribution (Plate 3.1). The larger grains are generally rounded, but can be very angular, with an increase in angularity as grain size decreases. Microcrystalline quartz grains within the interstitial pore spaces of the detrital material also have a bimodal distribution, where the grains are either ≤ 5 μm or approximately 20 μm. Physical disaggregation of the samples for determination of grain size distribution was not attempted because of the extremely well indurated nature of the samples.

3.1.2.2. Matrix, opaques, and organics

The matrix is composed of microcrystalline quartz, which shows a mosaic texture

in thin section (Plate 3.1). These grains are closely packed, filling almost all of the original pore space. In general, microcrystalline quartz grains completely fill the interstitial pore spaces of the framework grains while, less commonly, other areas are oil-filled with a trace of microcrystalline quartz. Authigenic, euhedral syntaxial quartz overgrowths were not observed by optical microscopy, although some euhedral quartz crystals growing on the surface of detrital quartz grains are observed in detailed SEM examination (Plate 3.2).

Although fluid inclusions in the matrix grains are rare and extremely small when found, it was possible to determine that the fluid inclusions do not have a hydrocarbon phase using UV light microscopy (365 nm). This suggests that the fluid from which the cement grew was devoid of an organic phase (V. Stasiuk, personal communication, 1996).

Abundant fine grained opaque material is observed in transmitted light. Although some of the "opaque" material is actually dark, bitumen-filled pore spaces (Plate 3.1), most of the opaques are probably mineral phases. A high proportion of the fine grained opaque material is authigenic Ti-oxides (Plate 3.3), and not detrital grains. Ti oxide grains are found within cracks in detrital quartz grains and in the interstices between microcrystalline quartz grains. These occurrences of authigenic Ti-oxides can not be attributed to a detrital origin. Coarser grained, opaque detrital clasts are observed in both thin section and BSE and were found to be dominantly Ti- and minor Zr-oxides.

Organic material is ubiquitous in the BRS, but is found in low amounts (see Rock Eval. data, Section 4.8). Organic material is primarily bitumen, which has a heterogeneous distribution, giving the BRS a blotchy colour in both hand samples and thin section. In thin section, where some of the pore spaces are saturated with the organic

material, the host rock does not appear to be well cemented. It is likely that areas with a higher degree of oil saturation are inherently less well cemented, and for this reason, microcrystalline grains are lost during thin section preparation. It can be shown that oil impregnation postdates growth of the authigenic quartz (Plate 3.4). The organic material was found as a solid or semi-solid material under the SEM, as shown in Plate 3.5.

3.1.3. Matrix textures

Typical petrographic textures observed in the BRS were discussed above. This section describes textures that are anomalous compared to the rest of the McMurray Formation proper. Characteristic textures observed in the matrix in the BRS are euhedral and subhedral microcrystalline quartz grains, pore-filling anhedral quartz, euhedral pockmarks, and dissolution textures.

3.1.3.1. Early microcrystalline quartz grains

Detailed inspection of the BRS using SEM revealed the fine grained matrix is composed of euhedral and subhedral microcrystalline quartz grains (Plates 3.6 and 3.2). Microcrystalline matrix grains vary in size from <5 μm to 20 μm. Generally, the larger grains are euhedral, and the finer grains appear to be both euhedral and subhedral. Unbroken crystal faces of the microcrystalline quartz grains are smooth and unabraded,

and dust rims are not observed within the microcrystalline quartz grains in thin section. These observations suggest that the euhedral microcrystalline quartz grains are formed *in situ*, as opposed to a detrital origin because surface abrasion and dust rims characteristic of detrital grains are not observed.

3.1.3.2. Later pore filling anhedral quartz

Anhedral microcrystalline quartz is abundant in the BRS. Generally, this phase has a massive texture, filling the pore spaces between the euhedral microcrystalline quartz grains. This implies that the anhedral quartz phase postdates growth of the euhedral grains. Plates 3.7 and 3.8 show examples of typical textures of anhedral quartz. The earlier-forming microcrystalline quartz grains can be found encased in this later pore filling, anhedral quartz cement, resulting in the well indurated nature of the BRS. In fact, the cementation is so strong that framework grains often fracture rather than separate along the grain boundaries during rock chip preparation.

An interesting observation made during SEM studies is shown on Plate 3.8. A pore is partly filled with microcrystalline quartz grains. As would be predicted, these grains are embedded in a late pore filling anhedral quartz matrix. However, because the pore is only partly filled, the planar surface suggests the formation of a geopetal fabric. The crystals at the bottom of the pore are finer grained and the interstices of these subhedral grains do not appear to be infilled to as great an extent as the euhedral crystals at the top of the pore. This is persuasive evidence that a later, pore-filling silica phase

cemented the microcrystals that formed *in situ*.

3.1.3.3. Euhedral pockmarks

An interesting feature observed in the BRS is the abundance of equant pockmarks. These pits range in size from <5 μm to 20 μm, similar to the microcrystalline quartz grains. Pockmarks are flat-bottomed pits, or narrow towards the bottom, forming angular pits. Generally, pockmarks are flat bottomed when found forming on framework grains; flat-bottomed pockmarks can also be found in the anhedral quartz matrix. Conversely, angular pits are found only in the anhedral quartz matrix, and not on the framework grains. Examples of the euhedral pockmarks are shown on Plate 3.7.

These pockmarks are formed during sample preparation for the SEM. Before the rock is broken, the euhedral microcrystalline quartz grains were able to grow into open pore spaces (Plate 3.6) during initial silicification. Later formation of the anhedral quartz matrix encased the microcrystalline quartz grains (Plate 3.8). When the rock is broken, the euhedral grains are plucked from the encasing cement, forming positive relief features such as the euhedral microcrystalline quartz and negative relief features such as the pockmarks.

3.1.3.4. Dissolution textures

Fenton and Ives (1990) described the edges of some of the framework grains in the

BRS as ragged and pitted. Framework grains with irregular and convoluted edges such as those observed in thin section (Plate 3.9) are not generated through normal abrasion during sedimentation. Scanning electron microscopy revealed similar textures (Plate 3.10) showing detrital grains, and even some euhedral microcrystalline quartz grains, captured in the process of corroding. These observations are characteristic of dissolution textures. Irregularly shaped grains are often observed in thin section, suggesting that local dissolution occurred in much of the proto-BRS sediments.

3.1.3.5. Non-silicate minerals

Base metal oxides, which are mainly Ti-oxides with a minor fraction of Zr-oxides, are abundant in the BRS (Plate 3.11). Ti-oxide grains are often found concentrated as streaks composed of many tiny crystals along framework grain edges. Textures suggesting some of the finer Ti- and Zr-oxide grains have a diagenetic origin are observed in the BRS. For example, Plate 3.11 shows geopetal textures of TiO_2 grains filling the bottom of a pore.

Fenton and Ives (1990) suggest that these opaques are rutile, sphene, and tourmaline. XRD analysis shows that the Ti-oxides are likely anatase. Mellon (1956) studied the heavy mineral content found in the McMurray Formation, and reported only two or three grains of rutile in each of his samples, and it is therefore a very minor constituent of the heavy mineral fraction.

Rock chips and polished uncovered thin sections of all BRS samples were studied

in detail using BSE-SEM and EDX to document mineral phases present. Abundant native Ni grains were observed in most of the samples (Plate 3.10). These grains can vary in size from ≤1 μm to >30 μm. Native Pt was found as discrete grains as well as rimming Ni grains (Plate 3.10). Pt also varies in size from ≤1 to 20 μm. Ni and Pt grains are irregularly shaped, usually with sharp edges (Plate 3.10). These native metal grains were occasionally found embedded in the bitumen, with only a small portion protruding from the surface (Plate 3.11). Other native metals observed by SEM in the BRS include Cr, Fe, Ag, Cu, and Pb.

Although precious metals are observed readily on rock chips, they are usually not observed in thin section. The simplest reason for this discrepancy is that the metals were lost during thin section preparation. Similar discrepancies were noted by Feng and Abercrombie (1994) and in unpublished results generated in 1994 by Craig Ford, then of Lac North America Ltd. (H. Abercrombie, personal communication, 1998).

3.2. Paragenetic Sequence

Petrographic observations must be organized into a paragenetic sequence to represent the various stages that occurred during formation of the BRS. These are (i) the growth of microcrystalline quartz grains, (ii) the formation of anhedral, pore filling quartz, (iii) dissolution textures, (iv) infiltration of hydrocarbons, (v) growth of authigenic base metal oxides, and (vi) enrichment of precious metals. Figure 3.1 is a schematic representation of the paragenetic sequence of the cementation of the BRS.

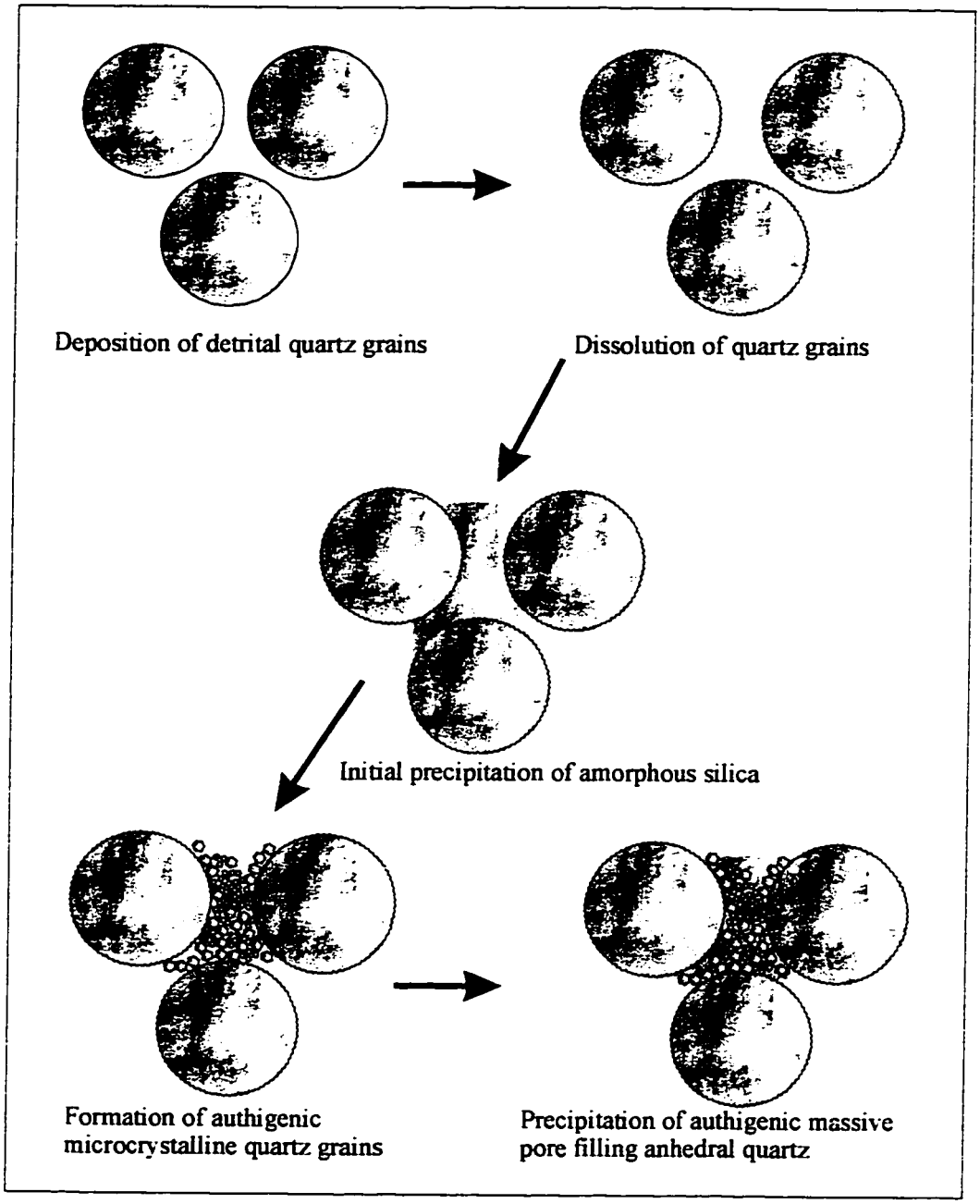

Figure 3.1 Schematic diagram showing the paragenetic sequence of the Beaver River sandstone. After deposition of the quartz grains , dissolution of the framework grains occurs, followed by the formation of euhedral and subhedral microcrystalline quartz crystals. These formed either through recrystallization of amorphous silica, or through the initial precipitation of quartz. Microcrystalline quartz forms with a bimodal size distribution, possibly due to varying pore fluid chemistry. A later pore-filling anhedral quartz develops during later episodes of quartz precipitation. Dissolution of framework grains and pirating of neoformed microcrystalline quartz supplies this period of later silica precipitation.

Generally, amorphous silica precipitates from hydrothermal solutions (White et al. 1956; Fournier, 1984) which can be followed by recrystallization to quartz through a dissolution-reprecipitation mechanism (Stein and Kirkpatrick, 1976; Kastner et al., 1978; Rimstidt and Barnes, 1980; Dove, 1995). Quartz is the only silica polymorph present in the BRS (Section 3.1.1.).

Is it possible that amorphous silica or other lower forms of silica precipitated directly from solution, and then completely recrystallized to quartz? Bjorlykke and Egeberg (1993) suggest that recrystallization of amorphous silica or opal-CT results in a microcrystalline chert-like texture. Moreover, original fabrics are destroyed during recrystallization (Ernst and Calvert, 1969; Hesse, 1989; S. Cady, written communication, 1997). However, the absence of amorphous silica does not necessarily mean that recrystallization has destroyed the lower silica polymorph. Rather, it could simply mean that recrystallization was never a step in the silicification of the BRS. Quartz is also known to precipitate directly from solution, without the opal-CT step (Morey et al, 1962; MacKenzie and Gees, 1971; Kastner et al, 1977; Hesse, 1989; M. Kastner, written communication, 1997). Therefore, it is possible that one of two things occurred: either silica was precipitated as a low silica polymorph (i.e. amorphous, opal, or chalcedony) which later recrystallized to quartz, destroying all original textures or, quartz was initially precipitated from solution, without a recrystallization stage.

Growth of microcrystalline quartz in proto-BRS sediments occurred postdepositionally since the crystal faces show no sign of abrasion. However,

recrystallization of a low silica polymorph also results in unabraded crystal faces through *in situ* growth. Silica precipitation is not only controlled by the kinetics of the system, but is also affected by the nucleation and growth of crystals. The type of nuclei available may control the type of neoformed silica polymorph. For instance, Renders and Barnes (1989) showed that laboratory growth of cristobalite is probably controlled by cristobalite nuclei. Similarly, MacKenzie and Gees (1971) demonstrate that authigenic quartz can grow on quartz nuclei from seawater at earth-surface conditions. This makes it difficult to determine whether quartz formed through recrystallization of a lower silica polymorph or whether quartz is the original polymorph. These authors suggest that quartz can precipitate directly from solution without recrystallization from a lower silica polymorph, and there is no direct evidence for a precursor silica polymorph in the BRS. Therefore, either silica initially precipitated as the microcrystalline quartz observed today, without recrystallization of other silica polymorphs, or amorphous silica was initially precipitated, followed by rapid recrystallization to microcrystalline quartz.

The pore-filling nature of the anhedral quartz is evidence that this stage postdates growth of euhedral and subhedral quartz grains. Moreover, the anhedral, pore-filling cement preserves outlines of quartz crystals, proving that the euhedral quartz crystals formed prior to the anhedral cement.

The timing of dissolution of the framework grains, and whether it occurred as a single event, is unclear, but textures suggest that multiple phases of both silica solution and precipitation occurred. This is demonstrated in Plate 3.10 where a primary quartz overgrowth is in the process of dissolving while proximal overgrowths are pristine,

suggesting multiple growth phases separated by an interval of dissolution. At the same time, one can observe framework grains that have undergone dissolution prior to growth of euhedral overgrowths, suggesting possible multiple dissolution phases. Plate 3.11 shows possible multiple growth phases of quartz, suggesting that proto-BRS sediments experienced variable chemical conditions or cyclic dissolution and precipitation of silica.

There are conflicting reports regarding the conditions under which Ti- and Zr-oxides are soluble. For example, Tugarinov et al. (1975) reports that the reaction of TiO_2 (rutile) and PbS (galena) forming $PbTiO_3$ (macedonite) is favored under basic conditions. Alternatively, Gibling and Rust (1992) suggest that authigenic TiO_2 is present in ganisters in the Waddens Cove Formation as a result of acidic conditions. King (1994) reports that TiO_2 is soluble only in HF, hot HCl, hot HNO_3 and hot concentrated H_3PO_4. Therefore, it is difficult to say whether authigenic Ti-oxides implies acidic conditions during BRS formation or whether these minerals precipitated under the same conditions which silicification occurred. Nevertheless, the geopetal textures suggest that these oxides formed after the onset of silicification.

Thin section examinations show that the introduction of bitumen postdates growth of microcrystalline quartz. Further investigations did not reveal any textures that would contradict this earlier finding. In fact, UV light examination determined that fluid inclusions in microcrystalline quartz do not have an organic phase, which supports earlier findings that the infiltration of organic material did not occur until after silicification of McMurray Formation sediments. It is impossible to determine the relationship between oil infiltration and authigenic base metal oxides. It was noted that precious metals are

sometimes embedded in organic material. These textures suggest that the introduction of metals occurred prior to the infiltration of bitumen into the McMurray Formation.

Plate 3.1. Typical BRS textures in transmitted light

A. AU94-017 taken at 40x magnification, crossed nicols. Notice the variation in grain size and the infrequent grains with abraded quartz overgrowths. The matrix is composed of fine grained quartz grains with bimodal distribution (image width 90 μm).

B. Same sample and magnification as A. Note the drastic difference in grain size and sorting (image width 90 μm).

C. AU94-007 taken at 100x magnification, crossed nicols. Notice the lack of fine grained material as compared to A and B (image width 35 μm).

D. AU95-013 taken at 40x magnification, plane light. Notice the "opaque" material in the matrix. This material is actually fine oil pockets trapped in the interstices of the matrix (image width 90 μm).

Plate 3.1

A

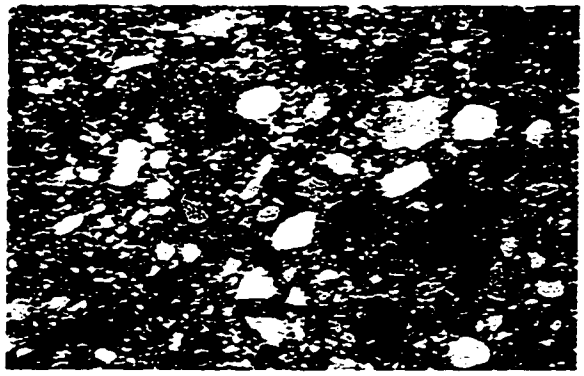

B

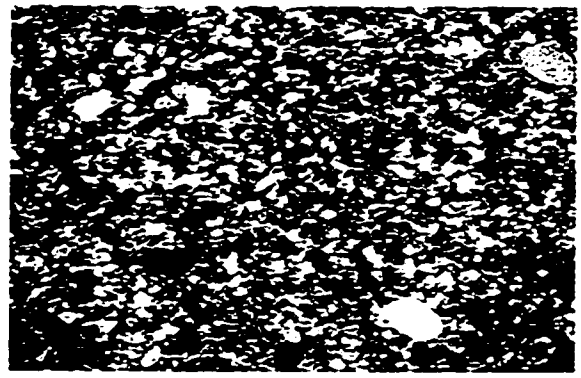

C

D

Plate 3.2. Dissolution and precipitation textures found on grains in the BRS

A. Euhedral microcrystalline quartz grain 10 μm in diameter sitting on the surface of a framework grain. The framework grain shows pitting textures indicative of dissolution.

B. Euhedral quartz overgrowths on framework grains. Notice how some of the overgrowths have partially dissolved while other overgrowths have not. This suggests multiple stages of quartz precipitation with an intermediary dissolution stage.

C. Euhedral to subhedral microcrystalline quartz grains settled at the bottom of a pore space and forming a geopetal texture.

D. Close-up of C. Note how the grains at the top of the pile of quartz grains are embedded in anhedral quartz cement whereas the grains below the surface are not cemented.

Plate 3.2

A

B

C

D

Plate 3.3. Base metal oxides

A. Backscattered secondary electron image of a thin section. Light grey grain is Ti-oxide (probably anatase). Irregular grain shape may be indicative of partial dissolution.

B. Detrital Ti- and Zr-oxide grains.

C. Partially dissolved(?)Ti- and Zr-oxide grains. Note the euhedral quartz overgrowths sharing the same porespace with these grains.

D. Geopetal texture of very fine grained Ti- and Zr-oxide grains. The brighter grains are composed of Zr.

E. Very fine crystals of Ti-oxide arranged along grain edges or fractures.

F. Very fine grains of Ti-oxide intermixed with microcrystalline quartz matrix.

Plate 3.3

A

B

C

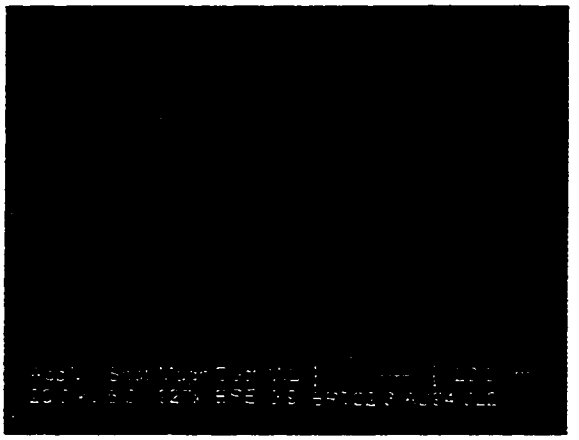

D

E

F

Plate 3.4. AU95-016 taken at 100x magnification, plane light showing oil postdating authigenic silica (image width 37 μm).

Plate 3.4

A

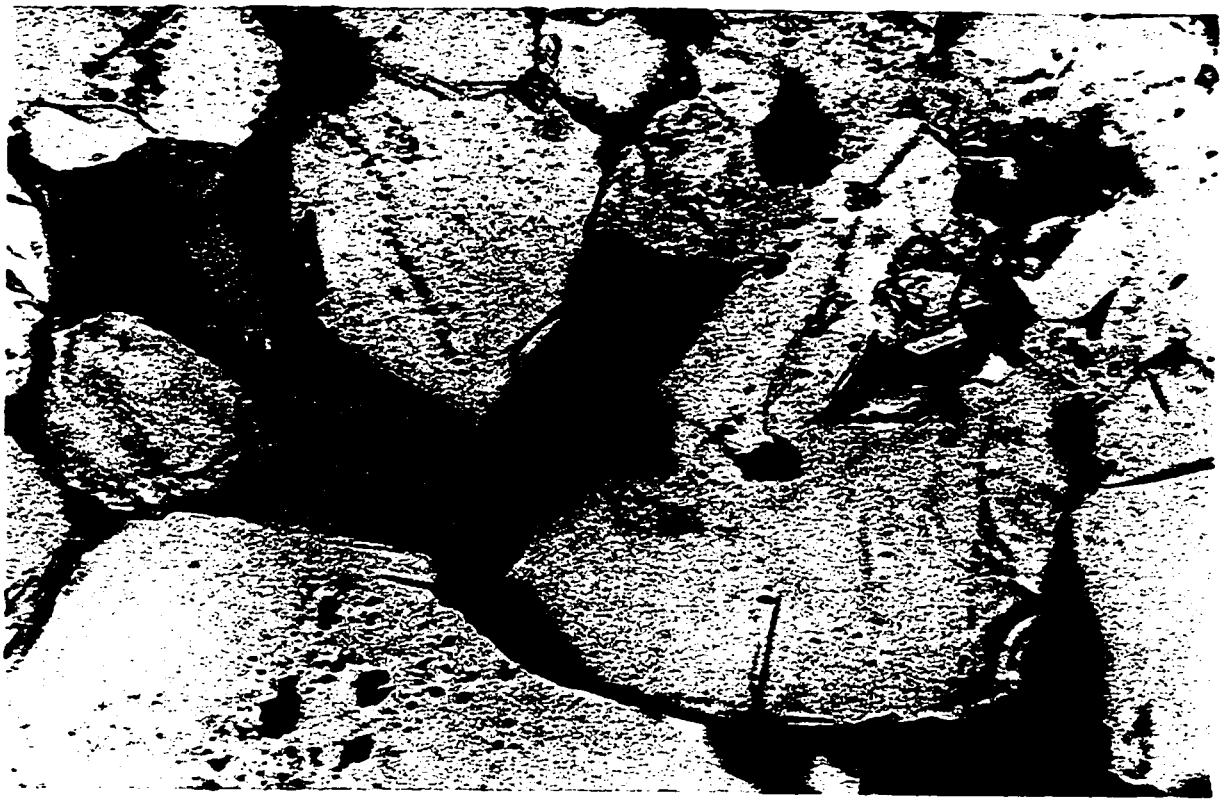

Plate 3.5. Solid or semi-solid nature of the organic material

A. Typical backscattered secondary electron image of the organic material found in the pore spaces.

B. Detail of inset shown on A. Notice how the organic material appears to have desiccation cracks.

C. Typical backscattered secondary electron image of the organic material (dark gray) found in the pore spaces.

Plate 3.5

A

B

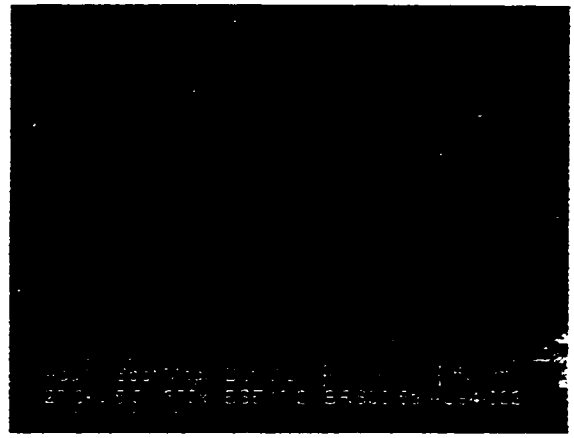

C

Plate 3.6. Euhedral and subhedral microcrystalline quartz grains

A. One type of microcrystalline quartz matrix found in the BRS. Notice the size of the grains is approximately 20 μm in diameter.

B. The second type of microcrystalline quartz grains found in the BRS. These grains are fairly uniform in size, generally <2 μm in diameter. Notice the pockmark texture on the unbroken surface of the detrital grain.

C. Similar subhedral microcrystalline quartz grains as in B. However, these grains are slightly larger than the grains shown in the previous image.

D. Close-up of the tight packing of the microcrystalline quartz grains. Notice the meniscus-like texture between the surface of the framework grain and the subhedral quartz matrix grains.

E. More typical subhedral microcrystalline quartz matrix grains.

F. Scanning electron image of microcrystalline quartz grains in thin section. The grains are not as tightly packed the grains shown in the previous images.

Plate 3.6

A

B

C

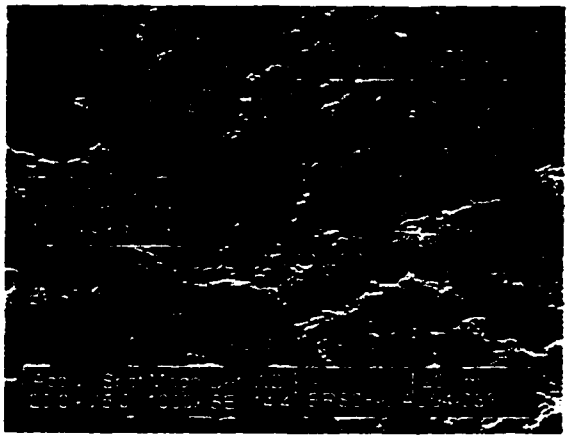

D

E

F

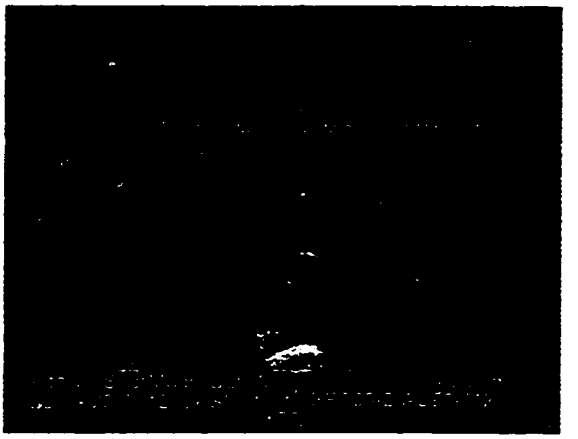

Plate 3.6. (Cont.)

G. Typical euhedral microcrystalline quartz grains. Notice the size of the grain shown in comparison to the one shown in A-F.

H. Euhedral microcrystalline quartz grains. Note the pristine, unabraded crystal faces and the tight packing of these grains.

I. More typical euhedral microcrystalline quartz grains. Grains shown range in size from 20 μm to 40 μm.

J. More typical euhedral microcrystalline quartz grains. Grains shown range in size from 5 μm to 100 μm.

K. Twinned quartz crystal shown in center of image. Notice the abraded grain surfaces shown to the left of center demonstrating the authigenic growth of quartz in the BRS.

Plate 3.6 (Continued)

G

H

I

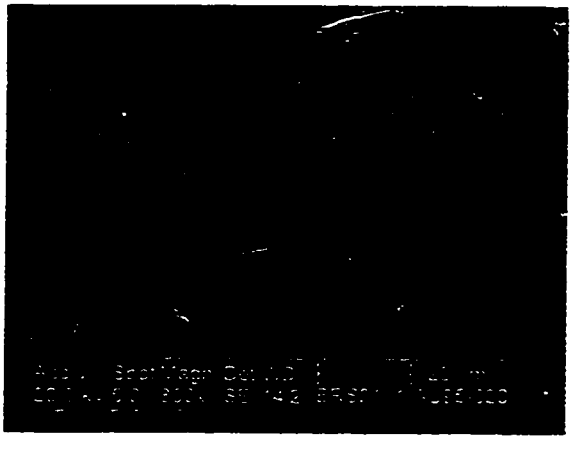

J

K

Plate 3.7. Euhedral pockmark textures

A. Hexagonal pockmark textures found in the BRS. These are likely formed during sample preparation when euhedral quartz grains embedded in the anhedral quartz are plucked out of the mold. Holes shown are generally 20 μm in diameter.

B. More hexagonal pockmarks found in the BRS. Notice the similar sized subhedral microcrystalline quartz grains shown at the bottom center of the image.

C. Sharp-edged polygonal pockmarks ranging in size from approximately 25 μm to 5 μm in diameter.

D. Less well developed polygonal pockmarks formed on the surface of a detrital grain. Notice the variable size of the pockmarks.

E. Same as D. Notice the difference in size and number of pockmarks as shown in the previous image.

F. Polygonal pockmarks shown at top of image. Euhedral to subhedral, closely packed quartz grains shown at bottom of image. Notice the similar size between the pockmarks and the grains. Also notice how the grains generally increase in size away from the detrital grain.

Plate 3.7

A

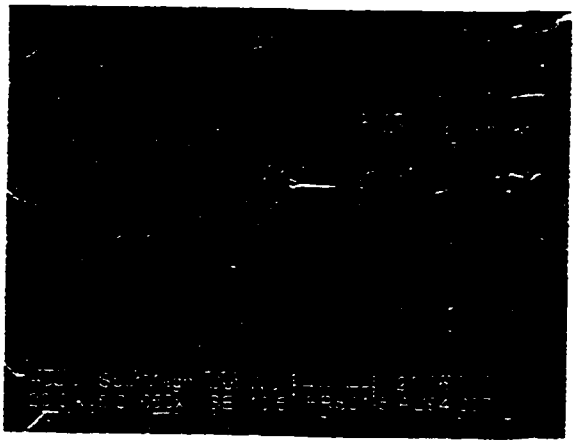

B

C

D

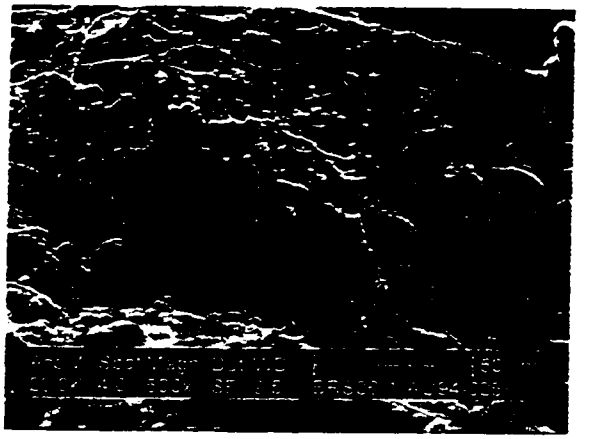

E

F

Plate 3.8. Late, pore filling anhedral quartz

A. Euhedral microcrystalline quartz grain embedded in a later, pore filling anhedral quartz.

B. More microcrystalline quartz grains embedded in the later, pore filling anhedral quartz.

C. Both euhedral pockmarks and anhedral quartz cast. Outlined is a euhedral microcrystalline quartz grain embedded in the anhedral quartz showing persuasive evidence that the anhedral quartz is a phase occurring after the formation of the original euhedral quartz grains.

Plate 3.8

A

B

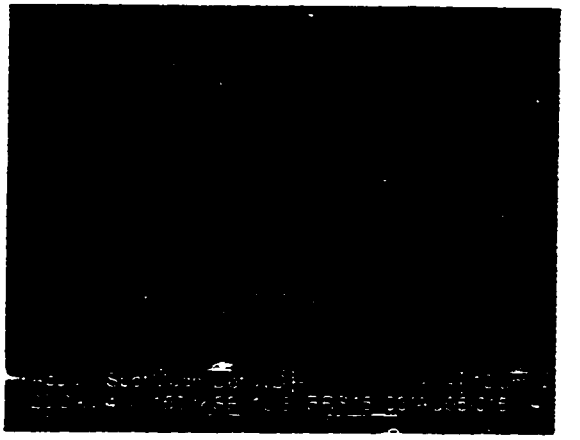

C

Plate 3.9. Framework grains showing dissolution textures in transmitted light

A. AU95-016 taken at 100x magnification, crossed nicols. Notice the ragged and pitted grain edges of bottom left grain. Textures indicate that the grain is in the process of dissolution (image width 37 μm).

B. Identical to A; plane polar light (image width 37 μm).

C. AU94-024 taken at 100x magnification, crossed nicols. Notice the highly degraded grain. The grain edge is diffuse, due to dissolution of the grain (image width 37 μm).

D. AU94-002 taken at 200x magnification, crossed nicols. Notice the solution pits and ragged edges of the grain at the top of the image (image width 18 μm).

E. AU95-002 taken at 200x magnification, crossed nicols. Notice the solution pits on the grain edges and the irregularly shaped grain, which are not typical of detrital processes (image width 18 μm).

F. Close-up of E, taken at 500x magnification. Notice the euhedral and subhedral hexagonal shaped grains within the solution pit (image width 7 μm).

Plate 3.9

A

B

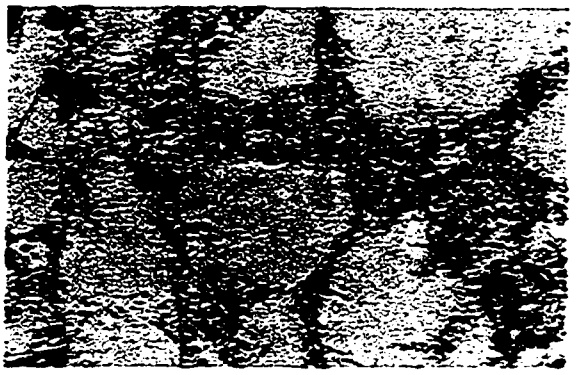

C

D

E

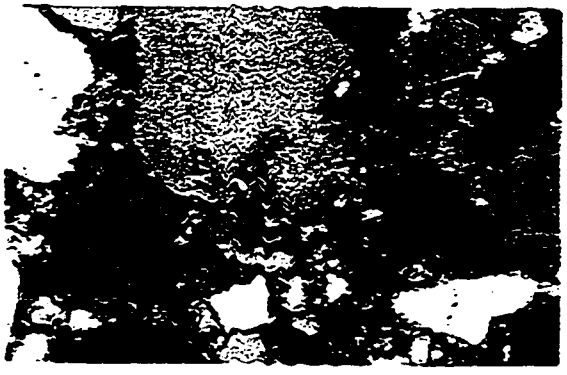

F

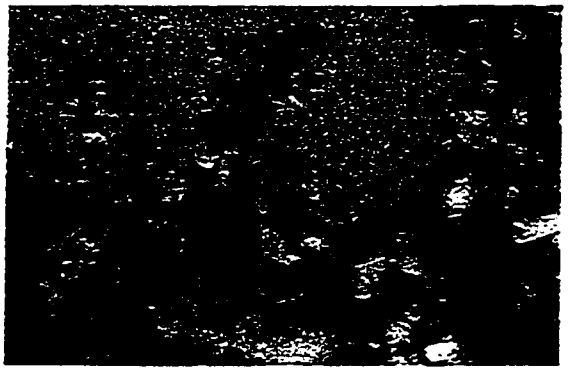

Plate 3.10. Trace and precious metals

A. Low magnification view of native Ni and Pt grains.

B. Inset shown in previous image. Native Ni and Pt-rimmed Ni grain.

C. Low magnification showing native Ni, Pt and Pt-rimmed Ni grains. This image was used to estimate the amount of native metals in the BRS.

D. Inset shown in previous image. Native Pt grain approximate 50 μm in diameter.

E. Inset shown in C. Native Ni and Pt-rimmed Ni grain, one approximately 40 μm in diameter and the other 25 μm in diameter.

F. Native Ag grain approximately 20 μm in diameter. Notice the different texture between this grain and the grains shown in the two previous images.

Plate 3.10

A

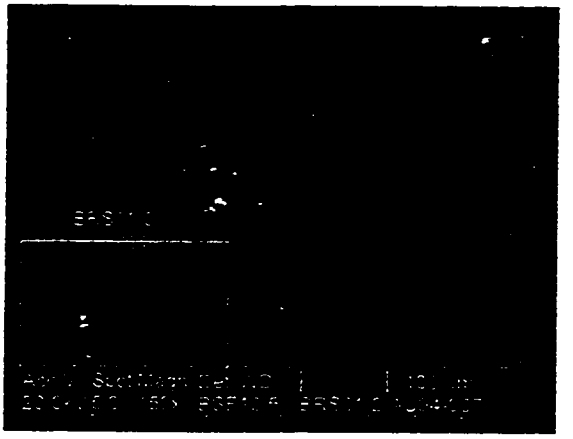

B

C

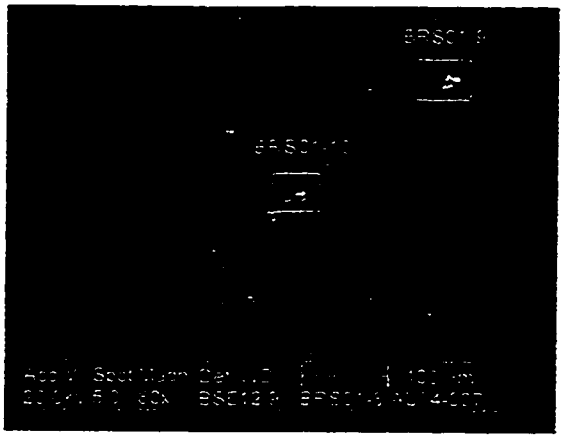

D

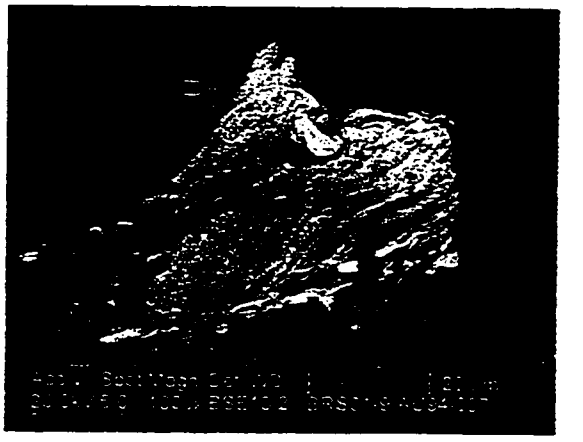

E

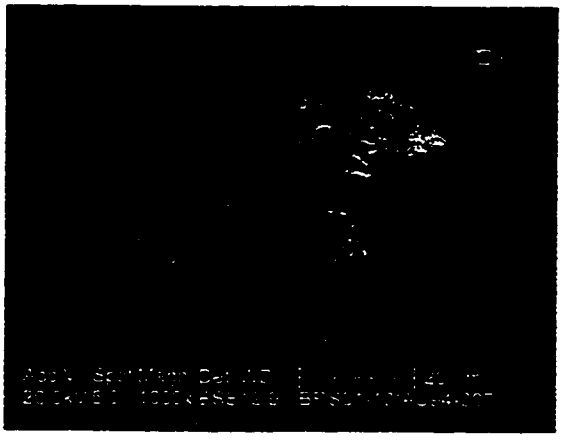

F

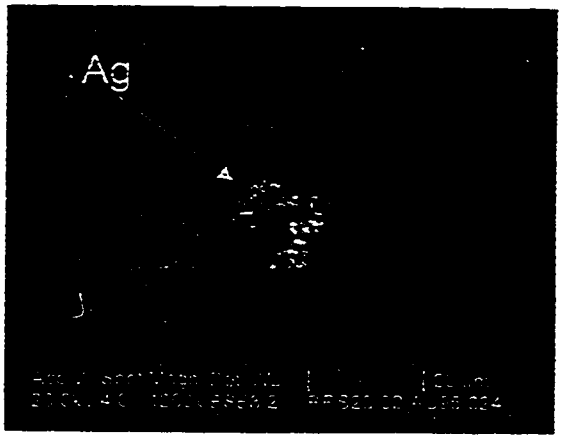

Plate 3.10. (Cont.)

G and H. BSE and SE images of a grain containing Cu>Ni>Zn sulfide. The grain is approximately 10 μm in diameter.

I and J. BSE and SE images of Pt grains. Grains are approximately 10 to 15 μm in diameter.

K. Very fine grained Sn oxide (?) grain containing trace amounts of Na, S, and Cl found in a pore space in thin section.

L. Low magnification view of several native Ni grains. Grains are <50 μm in diameter.

Plate 3.10 (Continued)

G

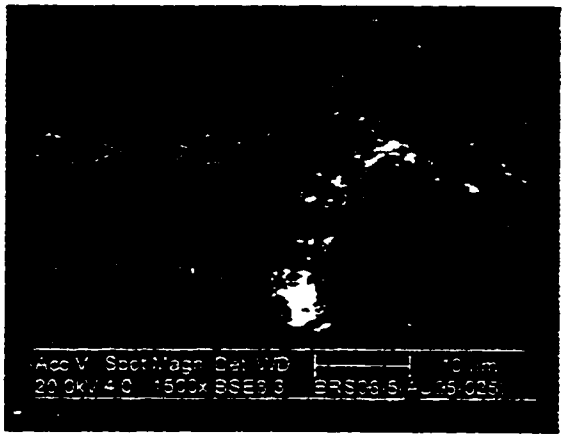

H

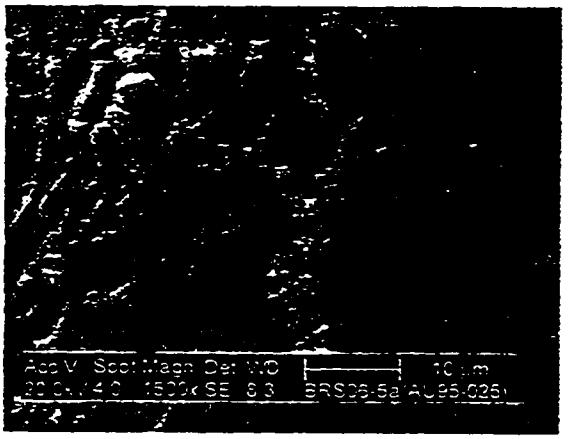

I

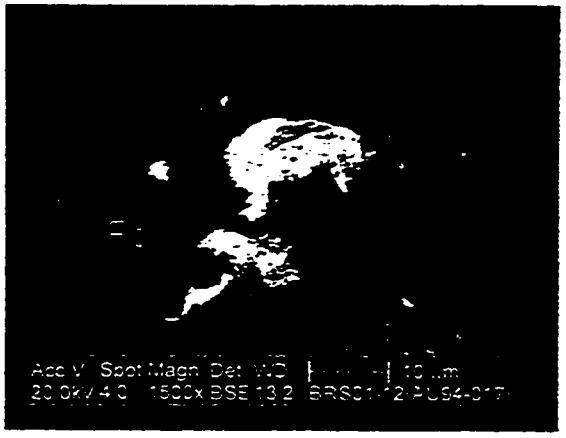

J

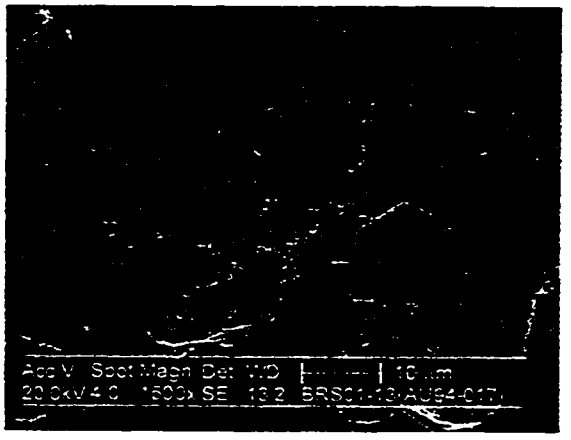

K

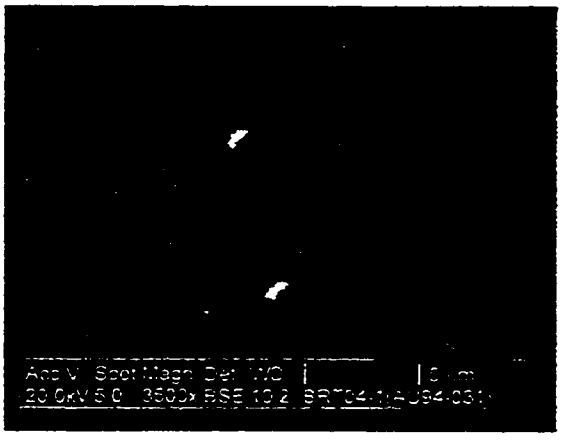

L

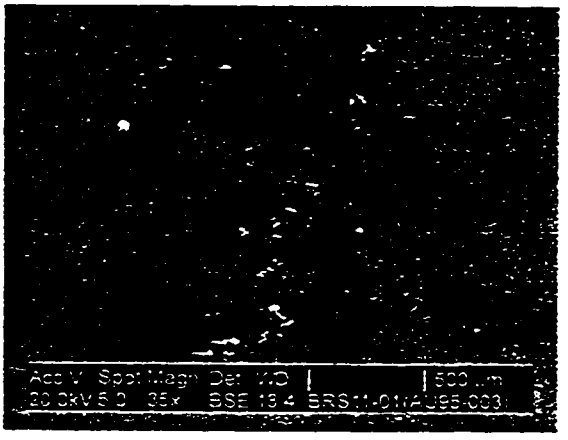

Plate 3.10. (Cont.)

M. Native Pb grain approximately 5 μm in diameter.

N. Low magnification view of native metal grains.

O and P. BSE and SE of inset shown in previous image. A native Ni grain containing Fe, Cu and Pb approximately 75 μm in diameter.

Q and R. BSE and SE of inset shown in N. Native Pt-rimmed Ni grain approximately 70 μm in diameter.

Plate 3.10 (Continued)

M

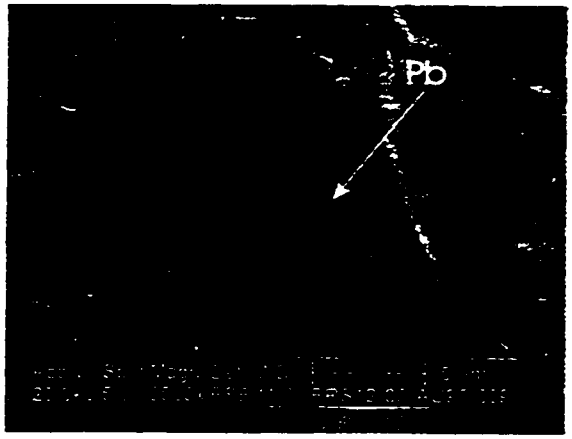

N

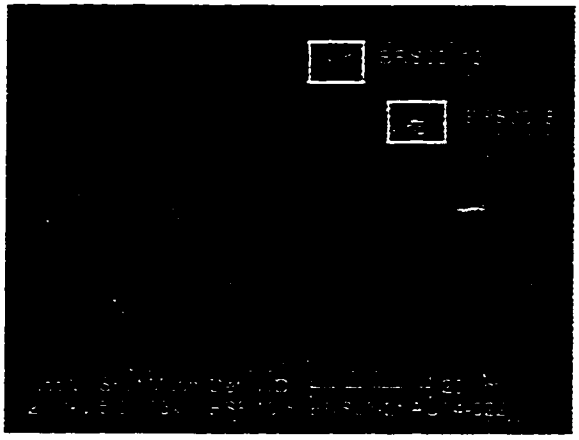

O

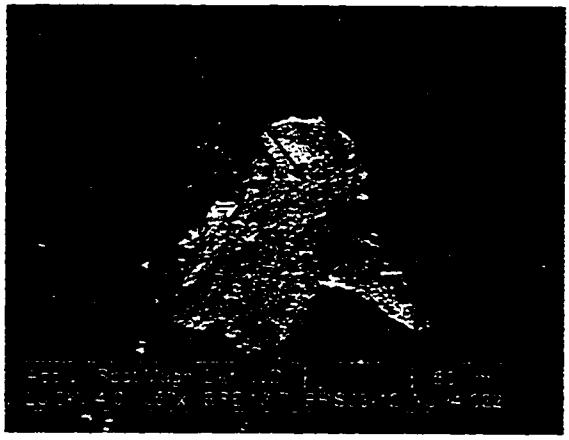

P

Q

R

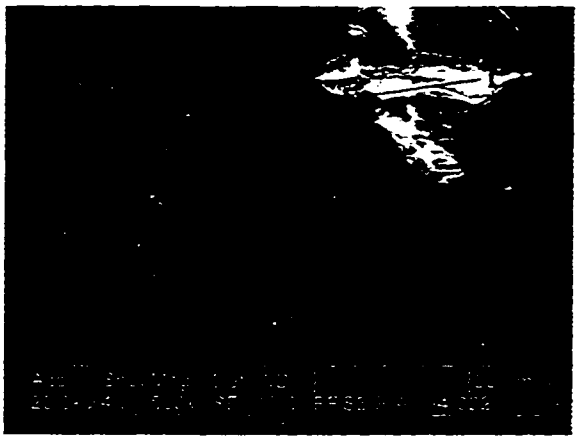

Plate 3.10. (Cont.)

S. Pyrite framboid found in porespace in thin section.

T. Native Ni grains approximately <5 to 20 μm.

Plate 3.10 (Continued)

S

T

Plate 3.11. Trace and precious metals associated within organic material.

A. Pt grain embedded in organic material. Pockmarks on the surface of the organic material due to volatalization or organic material during image collection.

B. Native Ni grains embedded in organic material.

C. A very fine grained Ag sulfide containing trace amounts of Cu and Ni.

D. Native Ni grains embedded in organic material.

E. More native Ni grain embedded in organic material.

Plate 3.11

A

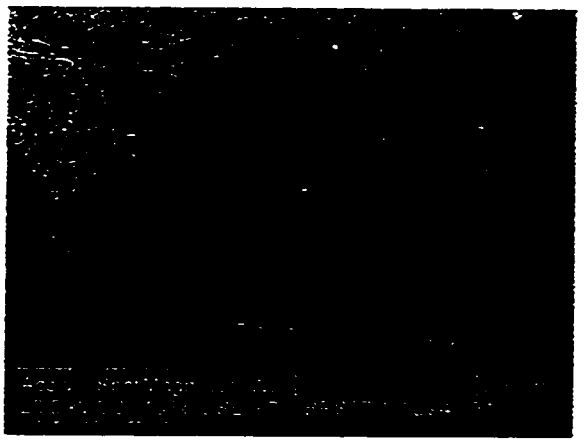

B

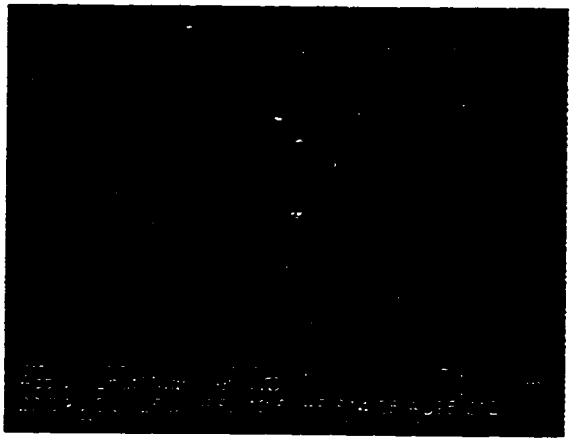

C

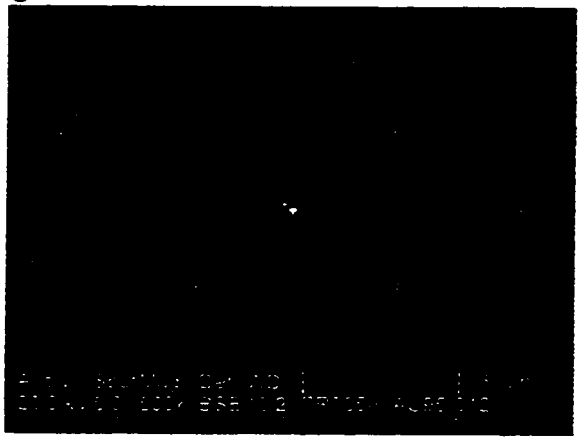

D

E

Chapter 4. Analytical geochemistry

This chapter reports the various methods used to analyze BRS samples collected during field activities. The sample suite used for analysis is found in Appendix 3. Several analytical techniques were used to characterize the sample suite. XRD was done to determine a semi-quantitative mineralogy. XRF was used to determine the major element composition. Minor and trace elements were analyzed by LA-ICP-MS for those elements not analyzed by XRF. An acid digestion method was developed to determine trace and precious metals found in the BRS during SEM study. ICP-MS was used to analyze these acid digested samples. Samples were analyzed externally by FA-DCP and INAA as standard analytical techniques for trace and precious metals. A method to leach water soluble salts was developed and ILC was used for the analysis.

Preparatory crushing and grinding of whole rock samples was done to ensure sample homogeneity. Samples were crushed to pea-sized grains with a hammer and anvil. Between 20 and 25 grams of sample was pulped with a "Bleuler" swing mill apparatus for one minute or until the powdered sample had the fineness of flour. These powders were used for all the analytical techniques except for those that were done externally. Pea-sized chips and larger pieces were sent to the external labs for FA-DCP and INAA analyses. Those labs were responsible for any additional sample preparation required.

4.1. X-Ray Diffraction

Samples selected for X-ray diffraction are tabulated in Table 4.1. The pulped samples were pressed into the sample holders by hand. To do this, a sample holder is placed upside down on a glass slide. More and more pulped sample is then pressed into the sample holder using a metal spatula until the powder forms a coherent mass in the sample holder. This ensures, not only that a flat surface exposed to the x-rays for proper analysis, but also so that the sample does not fall apart during analysis.

Table 4.1. Sample suite analyzed by XRD

AU94-007	AU95-009	AU95-017
AU94-017	AU95-011	AU95-019
AU94-022	AU95-012	AU95-020
AU94-023	AU95-013	AU95-021
AU94-024	AU95-014	AU95-023
AU95-002	AU95-015	AU95-024
AU95-003	AU95-016	AU95-025

Parameters for the x-ray diffractometer and d-spacings obtained for powdered samples are tabulated in Appendix 4. The raw data shows that the BRS is composed mainly of quartz, which is the only silica polymorph found. In accordance with petrographic observations, the spectra demonstrate the rareness of other minerals in the BRS. Feldspars and anatase (TiO_2) are also found, but only in trace amounts.

4.2. X-Ray Fluorescence

An attempt was made to pelletize the pulped samples for analysis, but the pellets shattered once the pressure was removed because of the high quartz content in the matrix. Therefore, it was necessary to fuse the samples in a glass bead. This was done by mixing 1 g of pulped BRS sample with 0.3 g of LiF and 5 g of $Li_2B_4O_7$ in a ceramic crucible. This mixture was then heated to 1000°C using a propane torch until the sample reached a molten liquid state. This melt was poured into an aluminum dish to cool into a glass bead, which was used for analysis.

Table 4.2 shows the composition of the major elements in the BRS as determined by XRF. The uniformity of the data suggests that this select sample suite is representative of all the samples. As expected, the most abundant oxide is SiO_2. TiO_2 and Fe_2O_3 are consistently found at levels higher than other elements, but only slightly above the other trace constituents. Sample AU94-017 is elevated in iron compared to other samples, which is consistent with the observation of pyrite in this sample and not in the others. Samples AU94-062 and AU94-079 are high in both CaO and Fe_2O_3, which is consistent with SEM and field descriptions, which suggest that siderite is a major portion of these samples.

4.3. Laser Ablation-Inductively Coupled Plasma-Mass Spectrometry

Laser ablation-inductively coupled plasma-mass spectrometry (LA-ICP-MS) was used as an additional method for the elemental analysis of a select number of samples. Samples found to contain native Ni and Pt by SEM analysis were chosen for analysis by LA-ICP-MS. The instrumental parameters used for the Fisons PQ2 with laser probe and electrothermal vaporizer are listed in Tables 4.3 and 4.4.

Rock chips were broken from hand samples using a hammer and anvil. The samples were mounted in a quartz glass chamber swept with high purity Ar gas. The flow rates for the gas are listed in Table 4.3. As the Nd-YAG laser is fired through the glass, a small amount of the sample vaporizes, condenses, and flows as an aerosol in the Ar gas stream to the ICP-MS.

National Institute of Science and Technology (NIST) standard glass 612 was used for standardization of Fe, Ni, Rb, Sr, Ag, Pb, Th, and U. In-house values were used for B, S, In, and Au. Se, Rh, Pd, Te, Re, Os, and Ir are only semi-quantitative because there is no internal standard used in this method. A sequence of blank, sample, then standard was run for each sample.

Table 4.2 XRF results (%).

Sample	Fe_2O_3	MnO	Cr_2O_3	TiO_2	BaO	CaO	K_2O	P_2O_5	SiO_2	Al_2O_3	MgO	Na_2O	SO_3	LOI	Total
AU94-007	0.23	0.00	0.03	0.54	0.01	0.10	0.00	0.01	97.98	0.69	0.05	0.00	0.00	0.41	100.05
AU94-017	6.42	0.08	0.02	0.88	0.01	0.44	0.05	0.02	87.02	0.66	0.46	0.00	0.00	3.96	100.02
AU94-022	0.18	0.00	0.01	0.18	0.00	0.05	0.00	0.01	98.38	0.04	0.07	0.00	0.00	1.13	100.05
AU94-023	0.24	0.00	0.02	0.28	0.00	0.04	0.00	0.00	99.19	0.04	0.05	0.00	0.00	0.25	100.11
AU94-024	0.20	0.00	0.01	0.22	0.00	0.05	0.00	0.00	99.21	0.05	0.05	0.00	0.00	0.27	100.06
AU94-025	0.28	0.00	0.02	0.43	0.00	0.05	0.00	0.00	99.02	0.06	0.07	0.00	0.00	0.18	100.11
AU94-030	0.31	0.00	0.03	0.28	0.00	0.08	0.00	0.01	97.56	0.05	0.07	0.00	0.00	1.62	100.01
AU94-037	0.22	0.00	0.02	0.37	0.00	0.08	0.00	0.00	98.98	0.04	0.07	0.00	0.00	0.32	100.10
AU94-046	0.30	0.00	0.01	0.74	0.01	0.06	0.00	0.00	96.16	0.29	0.09	0.00	0.00	2.40	100.06
AU94-062	0.64	0.04	0.00	0.04	0.00	52.64	0.11	0.01	3.27	0.49	0.66	0.00	0.00	42.16	100.06
AU94-078	28.72	0.13	0.02	0.06	0.01	0.47	0.00	0.21	57.26	2.91	0.34	0.00	0.00	9.93	100.06
AU94-079	2.28	0.04	0.00	0.07	0.00	48.90	0.31	0.04	4.17	1.18	1.93	0.00	0.00	41.19	100.11
AU95-002	0.38	0.00	0.04	0.61	0.00	0.06	0.00	0.01	98.34	0.09	0.09	0.00	0.00	0.45	100.07
AU95-003	0.33	0.00	0.03	0.17	0.00	0.05	0.00	0.01	98.89	0.03	0.06	0.00	0.00	0.55	100.12
AU95-009	0.43	0.00	0.05	0.52	0.00	0.05	0.00	0.01	98.85	0.04	0.06	0.00	0.00	0.05	100.06
AU95-011	0.53	0.00	0.06	0.40	0.01	0.05	0.00	0.01	98.48	0.06	0.06	0.00	0.00	0.42	100.08
AU95-012	0.34	0.00	0.04	0.51	0.01	0.05	0.00	0.00	98.46	0.10	0.07	0.00	0.00	0.58	100.16
AU95-013	0.37	0.00	0.04	0.16	0.00	0.05	0.00	0.01	97.57	0.50	0.07	0.00	0.00	1.33	100.10
AU95-014	0.42	0.00	0.04	0.25	0.00	0.05	0.00	0.01	98.14	0.03	0.09	0.00	0.00	1.00	100.03
AU95-015	0.28	0.00	0.03	0.21	0.00	0.06	0.00	0.00	98.86	0.04	0.07	0.00	0.00	0.51	100.06
AU95-016	0.36	0.00	0.04	0.87	0.11	0.05	0.00	0.01	98.32	0.07	0.07	0.00	0.00	0.22	100.12
AU95-017	0.56	0.00	0.06	0.69	0.00	0.05	0.00	0.01	98.54	0.09	0.07	0.00	0.00	0.00	100.07
AU95-019	0.52	0.00	0.06	0.37	0.00	0.06	0.00	0.01	98.79	0.05	0.06	0.00	0.00	0.11	100.03
AU95-020	0.41	0.00	0.05	0.78	0.01	0.05	0.00	0.01	98.63	0.07	0.06	0.00	0.00	0.01	100.08
AU95-021	0.45	0.00	0.05	0.63	0.01	0.05	0.00	0.00	98.47	0.07	0.09	0.00	0.00	0.25	100.07
AU95-023	0.37	0.00	0.04	0.54	0.01	0.05	0.00	0.01	98.14	0.58	0.07	0.00	0.00	0.30	100.11
AU95-024	0.27	0.00	0.03	0.12	0.00	0.05	0.00	0.01	97.68	0.02	3.07	0.00	0.00	1.73	102.98
AU95-026	0.13	0.00	0.01	0.19	0.00	0.06	0.00	0.00	95.51	0.46	0.05	0.02	0.00	3.61	100.04
AU96-002	0.12	0.00	0.02	0.01	0.00	0.04	0.00	0.01	99.82	0.04	0.04	0.00	0.00	0.00	100.10
AU96-009	0.32	0.00	0.04	0.89	0.01	0.05	0.00	0.01	98.42	0.08	0.07	0.00	0.00	0.12	100.01

Table 4.2 (Continued) XRF results (%).

Sample	Fe_2O_3	MnO	Cr_2O_3	TiO_2	BaO	CaO	K_2O	P_2O_5	SiO_2	Al_2O_3	MgO	Na_2O	SO_3	LOI	Total
AU96-011	0.24	0.00	0.03	0.27	0.00	0.05	0.00	0.00	99.03	0.04	0.05	0.00	0.00	0.32	100.03
AU96-012	0.19	0.00	0.02	0.30	0.00	0.04	0.00	0.00	98.86	0.04	0.07	0.00	0.00	0.58	100.10
AU96-014	0.16	0.00	0.02	0.20	0.00	0.05	0.00	0.01	98.41	0.17	0.07	0.00	0.00	0.92	100.01
AU96-015	0.28	0.00	0.03	0.52	0.00	0.05	0.00	0.01	98.38	0.06	0.07	0.00	0.00	0.71	100.11
AU96-041	15.14	0.36	0.01	0.22	0.03	3.40	0.28	0.15	62.63	2.18	0.23	0.00	0.00	15.42	100.05

Table 4.3 Instrumental parameters used for ICP-MS

Plasma Power (forward)	1348 watts
Plasma Power (reflected)	<3 watts
Gas flow (coolant)	14.5 L/min
Gas flow (auxiliary)	0.5 L/min
Gas flow (sample)	1.15 L/min
Sample cone	Ni, 1.0 mm diameter
Skimmer cone	Ni, 0.7 mm diameter
Acquisition time	80 s/repeat
Acquisition type	Peak hop mode
Channels per AMU	20
Dwell time	10.24 ms/channel/sweep
Detector	Channeltron, in dual mode
Tuning	on ^{197}In

The raw LA-ICP-MS data (Appendix 5) demonstrates how trace elements are distributed within each rock chip. Many of the trace elements have both relatively high values and relatively low values within the same rock chip, suggesting a heterogeneous distribution. This is in accord with the microdisseminated metallic grains observed by SEM. For example, native metals such as Fe, Ni, and Pt are often dispersed randomly throughout the BRS, but only as discrete metallic grains.

Table 4.4 Instrumental parameters used for laser probe

Type	Nd-YAG with laser oscillator, VG Model SL282
Wave length	1064 nm
Pulse energy	280 mJ minimum
Dial setting	5.5
Operating mode	Q-switched
Repetition rate	8 shots/sec
Time/spot	1 sec
Shot pattern	5 x 5, with 500 m spacing

LA-ICP-MS was used to quantify the metal content of this select set of samples, which is not possible through SEM analysis. However, it is difficult to determine a quantitative content because it is difficult to overcome the problems associated with accurately determining concentrations of heterogeneously distributed microdisseminated metals. Although the raw data for this method has been averaged for each sample analyzed (Table 4.5), it is unknown whether an average value is representative of the trace metal content in the BRS.

Table 4.5. Average elemental concentrations (ppm) for BRS rock chips as determined by LA-ICP-MS

Sample	Li 7	Be 9	B 11	Na 23	Mg 26	Al 27	Si 29
AU95-012	10.09	1.09	6	120	20	1847	460596
AU94-017	16.30	0.29	150	543	533	1346	421424
AU94-022	11.09	0.18	16	211	760	1848	414866
AU94-007	10.59	0.15	34	334	470	760	432976
AU94-025	15.70	0.28	25	187	155	2102	452693
AU95-019	14.85	0.09	20	106	223	2575	452733
Detection Limit	0.67	0.93	28	3328	18	65	3341

Sample	S 34	K39	Ca 43	Sc 45	Ti 49	V 51	Cr 52
AU95-012	4670	47	2707	20	738.8	122.53	15.8
AU94-017	1017	746	6419	28	77203	179.85	102.1
AU94-022	58202	865	20746	21	12062	512.36	45.4
AU94-007	28204	833	13818	24	18536	253.45	41.1
AU94-025	8340	771	4528	12	8324.9	52.62	15.4
AU95-019	1471	614	7489	12	6411.1	23.84	12.1
Detection Limit	2741	343	2529	19	5	0.62	5.3

Table 4.5. (Continued) Average elemental concentrations (ppm) for BRS rock chips as determined by LA-ICP-MS

Sample	Mn 55	Fe 57	Co 59	Ni 60	Zn 64	Cu 65	Ga 69
AU95-012	10.8	154	38	12.3	2.9	5	3.5
AU94-017	52	1849	2	10	76.2	42	20.6
AU94-022	86.8	2658	1	185.7	50.1	22	5.6
AU94-007	21.8	1046	1	93.3	69.4	35	5
AU94-025	170.3	1459	0	18.7	21.4	22	1.6
AU95-019	10	4381	-3	16.7	17	22	4.1
Detection Limit	2.9	347	14	7.4	4.2	15	1.8

Sample	Ge 73	As 75	Se 82	Rb 85	Sr 88	Y 89	Zr 90
AU95-012	3.6	0	0	1.17	8.559	22.051	378.12
AU94-017	1.9	7	0	0.93	25.832	67.488	755.72
AU94-022	1.5	2	0	2.14	54.619	18.047	402.28
AU94-007	1.7	3	0	1.21	13.701	183.14	634.43
AU94-025	0.8	1	0	0.86	4.531	8.793	217.52
AU95-019	5	3	0	0.77	4.048	4.762	204.58
Detection Limit	1.6	51	19	0.44	0.019	0.043	0.062

Sample	Nb 93	Mo 95	Rh 103	Pd 108	Ag 109	Cd 111	In 115
AU95-012	67.39	3.83	0.056	0.061	38.23	3.15	0.261
AU94-017	232.74	16.32	0.001	0.234	0.5	0.63	0.301
AU94-022	38.5	25.31	0.006	0.086	0.76	0.37	0.165
AU94-007	61.39	13.04	0.007	0.148	0.62	0.7	0.186
AU94-025	36.31	3.39	-0.04	0.077	0.14	0.27	0.041
AU95-019	25.03	2	0.004	0.067	0.79	0.27	0.057
Detection Limit	0.1	0.54	0.041	0.041	0.18	0.58	0.066

Sample	Sn 118	Sb 121	Te 125	Cs 133	Ba 138	La 139	Ce 140
AU95-012	5.78	1.71	2.88	0.43	40.61	3.164	6.174
AU94-017	42.48	4.93	0.13	0.07	84.367	23.904	52.772
AU94-022	10.32	1.04	0.07	0.14	437.2	3.567	8.837
AU94-007	15.93	2.07	0.05	0.06	128.97	2.107	6.45
AU94-025	4.44	0.7	0	0.04	21.06	2.124	5.033
AU95-019	3.69	0.81	-0.02	0.06	41.061	1.793	6.36
Detection Limit	0.59	0.22	0.29	0.11	0.045	0.05	0.011

Table 4.5. (Continued) Average elemental concentrations (ppm) for BRS rock chips as determined by LA-ICP-MS

Sample	Pr 141	Nd 146	Sm 147	Eu 151	Gd 157	Tb 159	Dy 163
AU95-012	0.991	5.29	2.881	0.35	5.19	0.658	4.84
AU94-017	6.665	24.28	6.774	1.87	8.9	2.038	14.35
AU94-022	0.828	3.61	1.226	0.3	1.9	0.493	4.58
AU94-007	0.667	3.37	1.145	0.32	1.65	0.425	3.31
AU94-025	0.434	1.71	0.495	0.09	0.77	0.151	1.27
AU95-019	0.592	2.22	0.468	0.12	0.583	0.097	0.73
Detection Limit	0.046	0.1	0.088	0.11	0.17	0.025	0.12

Sample	Ho 165	Er 166	Tm 169	Yb 174	Lu 175	Hf 177	Ta 181
AU95-012	1.461	4.36	0.651	4.497	0.914	15.416	6.089
AU94-017	3.1	9.785	1.581	11.796	1.529	29.556	19.596
AU94-022	0.877	3.083	0.052	3.745	0.568	15.732	3.936
AU94-007	0.817	2.9	0.515	4.179	0.675	24.844	5.772
AU94-025	0.314	1.221	213	1.562	0.233	7.075	2.522
AU95-019	0.176	0.633	0.111	0.986	0.139	6.564	1.554
Detection Limit	0.036	0.055	0.019	0.016	0.028	0.034	0.023

Sample	W 182	Re 185	Os 192	Ir 193	Pt 195	Au 197	Hg 200
AU95-012	6.513	-0.007	0.0666	0.036	0.0079	0.05	1.1
AU94-017	30.241	0.004	0	0	0.001	0	5
AU94-022	6.462	0.207	0.0135	0	0.0011	0.3	27.6
AU94-007	7.226	0.09	0.0187	0	0.0031	0.03	3.4
AU94-025	3.983	0.009	0	-0.001	0.0008	0	1.5
AU95-019	2.478	-0.01	0	0.015	0.0016	0.01	1.1
Detection Limit	0.028	0.033	0	0.037	0	0.35	3.5

Sample	Tl 205	Pb 208	Bi 209	Th 232	U 238
AU95-012	0.48	4.89	0.683	6.1574	8.2849
AU94-017	0.081	60.57	1.869	25.017	23.681
AU94-022	0.072	14.68	0.445	5.2404	5.1223
AU94-007	0.06	21.46	0.596	5.9816	11.842
AU94-025	0.038	6.58	0.211	2.6789	3.9348
AU95-019	0.01	7.03	0.181	1.9136	2.8569
Detection Limit	0.01	0.26	0.063	0.0049	0.0074

4.4. Inductively Coupled Plasma-Mass Spectrometry

4.4.1. Method

Initially, the efficiency of several preparatory methods were investigated using acid digestion of powdered BRS samples with the object of developing a fast, efficient method for analysis of bulk, powdered samples for trace and precious metals by ICP-MS. However, the turn-around time for analyses turned out to be slow and problem-filled. Regardless, a method was developed and is described below.

Various combinations of doubly distilled, concentrated HNO_3 and HF and 30% H_2O_2 were used as reagents for treating powdered BRS samples for microwave digestion as tabulated in Table 4.6. Incorporation of metals through biomineralization can occur (e.g. Urrutia and Beveridge, 1994; Konhauser et al., 1993; Ferris, 1990; Ferris, Beveridge, Fyfe, 1988), which may present problems in freeing material for analysis. For this reason, pretreatment with H_2O_2 was done to oxidize any organic material in the rocks.

The first set of bombs, 1 to 4, was preheated on a hot plate overnight to digest any organic material present. A MDS 2100 industrial microwave unit was used to speed up the digestion of the samples. The samples were run at 66% power and 80 psi for 15 minutes, with the time-at-pressure (TAP) set at 10 minutes. The samples were then vented to allow for escape of NO_2. It is necessary to cool the bombs before opening because the samples are extremely hot and the excess HF can be dangerous.

Table 4.6 Reagent volumes used for digestion method for AU94-046

Bomb #	Sample (g)	H_2O_2 (mL)	HNO_3 (mL)	HF (mL)
1	0.1	0	3.5	0.5
2	0.1	0.2	3.3	0.5
3	0.1	0	3.0	1.0
4	0.1	0.2	2.8	1.0
5	0.1	0	3.0	1.0
6	**0.1**	**0.4**	**2.6**	**1.0**
7	0.1	0	2.0	2.0
8	0.1	0.4	1.6	2.0

This set of bombs had to be heated a second time in the microwave because sample remained after the first digestion. No sample remained in bombs 1, 3, 4 after the second run, but refractory black specks, which are possibly carbides (S. Wu, written communication; Wu et al, 1996), were found in all bombs. The samples were run a third time in an attempt to digest the refractories but this extra step was ineffective.

To neutralize excess HF after microwave digestion, samples can be taken to dryness or a saturated boric acid quench can be added. It was decided to take the sample to incipient dryness since the quench would overwhelm subsequent detection of B in the ICP instrument. The residue was then solvated in 1 mL concentrated doubly distilled HNO_3 and again taken to dry. The samples were reconstituted to 22.5 mL with concentrated aqua regia[1] and made to a final volume of 25 mL with doubly distilled 18MΩ H_2O for ICP-MS analysis. Taking the samples to incipient dryness and making up in

[1] Aqua regia is 1 part HNO_3 to 3 parts HCl. 1 part H_2O can be added if the solution is to sit for extended periods of time.

comparable volumes ensures similar dilution for the samples so that no matrix effect occurs during analysis.

The second set of bombs, 5 to 8, was run with the same microwave method. This set had twice as much H_2O_2 as the first set, but was not preheated on the hotplate. Again, sample remained after heating so the samples were run a second time. Both sample and refractories remained in bombs 5 and 6 while only refractories remained in bombs 7 and 8. After a token third run, the samples were taken to dry with open vessels in the microwave at low temperature. Only bomb 6 had no sample or refractory material remaining. 1 mL of doubly distilled concentrated HNO_3 was added to the bombs and the solutions were taken to incipient dryness on a hot plate at low heat, redissolved in 22.5 mL aqua regia and made up to 25 mL with doubly distilled H_2O. Based on this work, method 6 was selected as the optimal method for sample preparation. However, scheduling and instrument problems delayed the analyses to such an extent that the samples aged[2] and were unsuitable for analysis.

A select number of samples were also sent to Activation Laboratories for total digestion ICP analysis. Their procedure is reported as follows:

"A 0.25 gram aliquot of sample is digested in 10 mL $HClO_4$-HNO_3-HCl-HF at 200°C to fuming and is diluted to 10 mL with dilute aqua regia.

---

[2] It is best to take up the samples in aqua regia for ICP-MS analysis on the day of analysis to avoid aging of the samples.

This leach is partial for magnetite, chromite, barite, spinels, zircon and massive sulfides. The solution are read on a simultaneous Jarrell Ash ICP spectrometer." (E. Hoffman, written communication)

4.4.2. Results

The results for total digestion ICP analysis from Activation Laboratories are summarized in Table 4.7. Most of the major elements analyzed are found at relatively low values, which is consistent with petrographic observations that silica is the predominant mineral phase in the BRS.

4.5. Fire Assay-Direct Coupled Plasma

Samples were sent to Bondar Clegg for fire assay analysis. The samples were dried and crushed to -10 mesh with a jaw crusher. From this, 250 g of the sample was pulped with a ring and puck grinding bowl to -150 mesh and 50 g of this was analyzed by FA-DCP using a Beckman Spectroscan 6.

The results shown in Table 4.8 are not consistent with the number of platinum grains observed in the BRS through SEM observations. Gold was never observed in the rock chips under BSEM investigation yet gold is consistently reported in the assay. Conversely, many Ni, Pt, and Pt-rimmed Ni grains were found in the BRS and yet the

Table 4.7 Total Digestion ICP analytical results

Sample	Mo (ppm)	Cu (ppm)	Pb (ppm)	Zn (ppm)	Ag (ppm)	Ni (ppm)	Mn (ppm)	Sr (ppm)	Cd (ppm)	Bi (ppm)	V (ppm)
AU94-023	<2	12	<5	3	<0.4	13	55	4	<0.5	<5	5
AU94-025	<2	37	<5	4	<0.4	17	52	5	<0.5	<5	5
AU94-033	<2	8	<5	2	<0.4	6	23	3	<0.5	<5	5
AU94-037	2	8	<5	2	<0.4	8	48	3	<0.5	<5	5
AU94-062	<2	4	5	31	0.6	3	247	302	<0.5	<5	6
AU94-079	<2	5	<5	9	0.6	6	243	311	<0.5	<5	9
AU95-002	2	9	<5	2	<0.4	7	31	5	<0.5	<5	7
AU95-003	<2	5	<5	2	<0.4	4	31	2	<0.5	<5	3
AU95-009	2	7	<5	2	<0.4	5	38	2	<0.5	<5	4
AU95-010	2	5	8	2	0.5	12	20	7	<0.5	<5	22
AU95-012	<2	6	<5	2	0.8	6	20	2	<0.5	<5	7
AU95-013	2	8	<5	2	<0.4	7	31	2	<0.5	<5	6
AU95-014	2	5	<5	2	<0.4	6	21	2	<0.5	<5	6
AU95-015	<2	6	<5	2	<0.4	3	18	2	<0.5	<5	3
AU95-016	2	7	<5	2	<0.4	6	27	3	<0.5	<5	8
AU95-017	2	7	<5	2	<0.4	4	22	3	<0.5	<5	7
AU95-019	<2	6	<5	2	0.6	3	15	2	<0.5	<5	2
AU95-020	2	6	<5	2	<0.4	6	28	3	<0.5	<5	6
AU95-021	<2	7	<5	2	0.8	4	17	3	<0.5	<5	4
AU95-023	4	7	<5	3	0.6	5	28	3	<0.5	<5	5
AU95-025	<2	7	<5	2	<0.4	3	25	2	<0.5	<5	5
AU95-043	<2	4	<5	2	0.4	5	12	3	<0.5	<5	12

Table 4.7 (Continued) Total Digestion ICP analytical results

Sample	Y (ppm)	Be (ppm)	Ca %	P %	Mg %	Ti %	Al %	K %
AU94-023	2	<2	0.05	0.002	0.05	0.11	0.04	0.01
AU94-025	2	<2	0.07	0.002	0.09	0.16	0.04	0.01
AU94-033	2	<2	0.02	0.002	0.02	0.21	0.03	0.01
AU94-037	2	<2	0.05	0.002	0.01	0.14	0.02	0.01
AU94-062	10	<2	49.45	0.01	0.35	0.02	0.29	0.12
AU94-079	6	<2	41.44	0.01	0.93	0.03	0.59	0.26
AU95-002	4	<2	0.16	0.002	0.01	0.22	0.05	0.01
AU95-003	2	<2	0.05	0.002	0.01	0.06	0.02	0.03
AU95-009	2	<2	0.02	0.002	0.01	0.23	0.03	0.01
AU95-010	2	<2	0.04	0.003	0.03	0.04	0.48	0.01
AU95-012	4	<2	0.01	0.003	0.01	0.02	0.04	0.01
AU95-013	2	<2	0.02	0.002	0.01	0.17	0.02	0.01
AU95-014	2	<2	0.02	0.002	0.01	0.09	0.03	0.01
AU95-015	2	<2	0.01	0.004	0.01	0.12	0.02	0.01
AU95-016	4	<2	0.01	0.002	0.01	0.26	0.03	0.03
AU95-017	4	<2	0.01	0.002	0.01	0.21	0.03	0.01
AU95-019	2	<2	0.02	0.002	0.01	0.11	0.03	0.01
AU95-020	4	<2	0.02	0.002	0.01	0.25	0.04	0.03
AU95-021	4	<2	0.05	0.002	0.01	0.19	0.03	0.02
AU95-023	2	<2	0.02	0.002	0.01	0.19	0.04	0.01
AU95-025	2	<2	0.01	0.002	0.01	0.18	0.03	0.02
AU95-043	2	<2	0.01	0.002	0.01	0.16	0.04	0.03

fire assay numbers do not confirm these observations. There apparently is a discrepancy between SEM observations and standard analytical techniques.

4.6. Instrumental Neutron Activation Analysis (INAA)

Samples were sent to Activation Laboratories for neutron activation analysis. Their procedure is reported as follows:

> "30 gram aliquot is encapsulated in a polyethylene vial and irradiated with flux wires and a run standard (1 for 11 samples) at a thermal neutron flux of $7x10^{11}n/cm^2s$. After a 7 day decay to allow ^{24}Na to decay the samples were counted on a high purity Ge detector with resolution of better than 1.7 KeV for the 1332 KeV Co-60. Using the flux wires the decay corrected activities are compared to a calibration developed from multiple certified international reference materials. The run standard present is only a check on accuracy of the analysis and is not used for calibration purposes. From 10-30% of samples were rechecked by remeasurement."
>
> (E. Hoffman, written communication, 1997)

Tabulated results are found in Table 4.9. Generally, most elements are below detection limit, or are found at very low abundance.

Table 4.8 FA-DCP values for Au, Pt, and Pd

Sample	Au (ppb)	Pt (ppb)	Pd (ppb)
AU94-017	4	<5	<1
AU94-022	5	<5	<1
AU94-023	4	<5	<1
AU94-024	<1	7	<1
AU94-025	1	6	<1
AU94-031	2	<5	<1
AU94-037	2	<5	<1
AU94-078	1	<5	<1
AU95-002	3	9	1
AU95-003	1	<5	<1
AU95-009	4	<5	<1
AU95-011	3	5	<1
AU95-012	<1	<5	<1
AU95-013	2	<5	<1
AU95-014	2	5	<1
AU95-015	<1	<5	<1
AU95-016	4	<5	<1
AU95-017	3	<5	1
AU95-019	2	<5	<1
AU95-020	<1	<5	<1
AU95-023	13	<5	3
AU95-024	<1	<5	2
AU95-025	<1	<5	10

Table 4.9 Combination INAA/Total Digestion - ICP

Sample	Au (ppb)	Ag (ppm)	As (ppm)	Ba (ppm)	Br (ppm)	Ca %	Co (ppm)	Cr (ppm)	Cs (ppm)	Fe %	Hf (ppm)	Hg (ppm)
AU94-023	3	<5	0.8	<50	<.5	<1	2	61	<1	0.58	12	<1
AU94-025	<2	<5	0.5	<50	<.5	<1	1	27	<1	0.5	10	<1
AU94-033	<2	<5	<.5	<50	<.5	<1	<1	14	<1	0.22	9	<1
AU94-037	3	<5	0.5	<50	<.5	<1	<1	14	<1	0.58	8	<1
AU94-062	<2	<5	1.6	79	2.2	38	1	8	<1	0.53	<1	<1
AU94-079	<2	<5	<.5	62	3.4	40	3	15	<1	1.68	<1	<1
AU95-002	<2	<5	<.5	56	<.5	<1	<1	35	<1	0.37	10	<1
AU95-003	<2	<5	<.5	<50	<.5	<1	<1	30	<1	0.2	5	<1
AU95-009	<2	<5	<.5	150	<.5	<1	<1	25	<1	0.45	12	<1
AU95-010	<2	<5	0.5	<50	<.5	<1	<1	11	<1	0.31	2	<1
AU95-012	<2	<5	0.5	<50	<.5	<1	<1	17	<1	0.23	11	<1
AU95-013	<2	<5	0.6	<50	<.5	<1	<1	34	<1	0.47	8	<1
AU95-014	<2	<5	<.5	<50	<.5	<1	<1	14	<1	0.27	7	<1
AU95-015	<2	<5	<.5	<50	<.5	<1	<1	16	<1	0.22	8	<1
AU95-016	<2	<5	<.5	<50	<.5	<1	<1	24	<1	0.27	10	<1
AU95-017	<2	<5	1.7	<50	<.5	<1	<1	25	<1	0.28	6	<1
AU95-019	<2	<5	<.5	<50	<.5	<1	<1	15	<1	0.21	9	<1
AU95-020	<2	<5	0.7	<50	<.5	<1	<1	28	<1	0.28	11	<1
AU95-021	<2	<5	<.5	<50	<.5	<1	<1	32	<1	0.23	12	<1
AU95-023	<2	<5	0.7	<50	<.5	<1	<1	39	<1	0.33	9	<1
AU95-025	<2	<5	0.6	<50	<.5	<1	<1	18	<1	0.33	8	<1
AU95-043	<2	<5	<.5	<50	<.5	<1	<1	6	<1	0.16	6	<1

Table 4.9 (Continued) Combination INAA/Total Digestion - ICP

Sample	Ir (ppb)	Mo (ppm)	Na %	Ni (ppm)	Rb (ppm)	Sb (ppm)	Sc (ppm)	Se (ppm)	Sn %	Sr %	Ta (ppm)	Th(ppm)
AU94-023	<5	<1	0.01	<20	<15	0.2	1	<3	<0.01	<0.05	0.8	1
AU94-025	<5	1	0.01	<20	<15	0.2	0.2	<3	<0.01	<0.05	0.7	1.1
AU94-033	<5	1	<.01	<20	<15	0.2	1.1	<3	<0.01	<0.05	0.8	1.3
AU94-037	<5	3	<.01	<20	<15	0.2	0.8	<3	<0.01	<0.05	0.6	0.7
AU94-062	<5	1	0.03	<20	<15	<.1	1.3	<3	<0.01	<0.05	<.5	0.7
AU94-079	<5	<1	0.03	<20	<15	<.1	2.2	<3	<0.01	<0.05	<.5	1.2
AU95-002	<5	3	0.01	<20	<15	0.4	1.3	<3	<0.01	<0.05	0.7	1.5
AU95-003	<5	3	<.01	<20	<15	0.1	0.4	<3	<0.01	<0.05	<.5	0.7
AU95-009	<5	3	0.01	<20	<15	0.4	1.3	<3	<0.01	<0.05	0.7	1.2
AU95-010	<5	2	0.01	<20	<15	0.1	1.2	<3	<0.01	<0.05	<.5	2
AU95-012	<5	2	0.01	<20	<15	0.3	1.4	<3	<0.01	<0.05	0.9	1.4
AU95-013	<5	<1	0.01	<20	<15	0.5	0.9	<3	<0.01	<0.05	0.5	1
AU95-014	<5	3	<.01	<20	<15	0.2	0.6	<3	<0.01	<0.05	<.5	0.6
AU95-015	<5	2	<.01	<20	<15	0.1	0.8	<3	<0.01	<0.05	<.5	0.7
AU95-016	<5	3	<.01	<20	<15	0.2	1.4	<3	<0.01	<0.05	0.8	1.4
AU95-017	<5	2	<.01	<20	<15	0.5	1.1	<3	<0.01	<0.05	0.8	1.3
AU95-019	<5	2	0.01	<20	<15	0.2	0.8	<3	<0.01	<0.05	0.6	0.8
AU95-020	<5	3	0.01	<20	<15	0.4	1.2	<3	<0.01	<0.05	0.6	1.3
AU95-021	<5	1	0.01	<20	<15	0.2	1	<3	<0.01	<0.05	0.7	1.3
AU95-023	<5	1	0.01	<20	<15	0.9	1.1	<3	<0.01	<0.05	0.6	1.4
AU95-025	<5	2	0.01	<20	<15	0.2	0.9	<3	<0.01	<0.05	0.5	3
AU95-043	<5	2	0.01	<20	<15	0.3	0.8	<3	<0.01	<0.05	0.5	3

Table 4.9 (Continued) Combination INAA/Total Digestion - ICP

Sample	U (ppm)	W(ppm)	Zn (ppm)	La (ppm)	Ce (ppm)	Nd (ppm)	Sm (ppm)	Eu (ppm)	Th (ppm)	Yb (ppm)	Lu (ppm)
AU94-023	1.2	<1	<50	0.6	<3	<5	0.2	<0.2	<0.5	1.1	0.18
AU94-025	0.8	<1	<50	0.9	<3	<5	0.2	<0.2	<0.5	1.2	0.2
AU94-033	1.4	<1	<50	0.9	<3	<5	0.2	<0.2	<0.5	1.1	0.22
AU94-037	0.7	<1	<50	0.6	<3	<5	0.1	<0.2	<0.5	0.9	0.16
AU94-062	<0.5	<1	<50	4.6	10	<5	0.9	0.3	<0.5	0.6	0.1
AU94-079	<0.5	<1	<50	4.6	8	<5	0.8	0.2	<0.5	0.5	0.07
AU95-002	1.5	<1	<50	1.2	3	<5	0.3	<0.2	<0.5	1.4	0.25
AU95-003	0.6	<1	<50	<0.5	<3	<5	0.1	<0.2	<0.5	0.5	0.08
AU95-009	1.4	<1	<50	0.7	<3	<5	0.2	<0.2	<0.5	1.4	0.23
AU95-010	<0.5	<1	<50	7.4	13	<5	0.5	<0.2	<0.5	0.3	<.05
AU95-012	1.3	<1	<50	0.8	<3	<5	0.2	<0.2	<0.5	1.5	0.25
AU95-013	1.4	<1	<50	0.6	<3	<5	0.1	<0.2	<0.5	0.9	0.14
AU95-014	0.7	<1	<50	<0.5	<3	<5	0.1	<0.2	<0.5	0.7	0.12
AU95-015	0.8	<1	<50	0.5	<3	<5	0.1	<0.2	<0.5	0.9	0.15
AU95-016	1.3	<1	<50	0.9	<3	<5	0.2	<0.2	<0.5	1.4	0.23
AU95-017	1	<1	<50	2.1	4	<5	0.3	<0.2	<0.5	1.3	0.19
AU95-019	1	<1	<50	<0.5	<3	<5	0.1	<0.2	<0.5	1	0.16
AU95-020	1.3	<1	<50	0.8	<3	<5	0.2	<0.2	<0.5	1.3	0.24
AU95-021	1.1	<1	<50	0.7	<3	<5	0.2	<0.2	<0.5	1.6	0.27
AU95-023	1.3	<1	<50	0.9	<3	<5	0.2	<0.2	<0.5	1.2	0.2
AU95-025	0.6	<1	<50	0.7	<3	<5	0.2	<0.2	<0.5	1	0.17
AU95-043	0.8	<1	<50	1.3	<3	<5	0.2	<0.2	<0.5	0.9	0.15
									<2	0.2	<5

4.7. Ion Liquid Chromatography

4.7.1. Method

Sylvite was found in thin section during BSEM work. If a brine fluid played some part in the formation of the BRS then it stands to reason that salts might be found in the samples. Pulped BRS samples were leached with 18MΩ doubly distilled water to determine the soluble salt content of the rocks.

2 g of pulped sample was subjected to three separate ultrasonic treatments lasting 45 minutes each. 8.5 mL of 18 MΩ H_2O was used as the leachant with a small amount of acetone to dissolve soluble organic material. After each ultrasonic treatment the samples were centrifuged, decanted and collected. Samples were centrifuged at 800 rpm for at least 1 hour before collecting the supernatant in a separate Nalgene bottle. 8.5 to 9 mL of fresh 18 MΩH_2O was added to the pulp for the following ultrasonication. Once all ultrasonication steps were completed the samples were centrifuged for at least 60 minutes at 4000 rpm to settle the pulped sample. Some fine grained material was still suspended in the final solution so it was necessary to filter an aliquot before ILC analysis. The cloudy sample was drawn into a 10 mL syringe, injected through a filter adapted to screw onto the mouth of the syringe, and collected for analysis.

A Dionex 500 liquid chromatograph system with a Dionex Anion Self-regenerating Suppressor ASRS-I at a current setting of 100 mA was used for anion analysis. An ED40

Electrochemical Detector and an AD20 Absorbance Detector operating at 215 nm were used for the detectors. Anions were separated on a Dionex IONPAC AS4A-SC 4 mm column with a sodium carbonate/bicarbonate eluent at a flow rate of 2.0 mL per minute and sample volume of 20 μL.

A Dionex 500 liquid chromatograph system with a Dionex Cation Self-regenerating Suppressor CSRS-I at a current setting of 100 mA was used for cation analysis. An ED40 Electrochemical Detector was used as the detector. Cations were separated on a Dionex IONPAC CS-12 4mm column with 16 mM methanesulfonic acid eluent at a flow rate of 1.0 mL per minute and sample volume of 20 μL.

4.7.2. Results

The raw analytical results of anions and cations can be found in Appendix 6 and the soluble ion content values are tabulated in Table 4.10. Generally, the leachates produced from the samples were quite fresh since many of the ions were found in low amounts. These results are in accord with the low analytical values obtained by XRF for the alkaline earth elements. Both XRF and this selective 18MΩ H_2O leach method find Na, K, Ca, and Mg at relatively low amounts. Soluble salts that might be found in the BRS would likely be halite or gypsum/anhydrite since these minerals are first to precipitate from a Na^{-}, Ca^{-2}, Cl^{-}, SO_4^{-2} rich water.

Table 4.10. Soluble ion content in leached samples (ppm-rock)

sample	Cl	Br	NO3	PO4	SO4	Li	Na	NH4	K	Mg	Ca
94-007	0.004	< D.L.	< D.L.	< D.L.	0.015	< D.L.	0.004	0.001	0.007	0.005	0.180
94-017	0.002	0.001	0.001	< D.L.	0.023	0.001	0.003	0.002	0.013	0.059	0.167
94-022	0.002	0.001	0.001	< D.L.	0.026	< D.L.	0.002	0.001	0.006	0.002	0.018
94-023	0.002	< D.L.	0.000	< D.L.	0.008	< D.L.	0.002	0.002	0.006	0.002	0.015
94-024	0.002	< D.L.	0.003	< D.L.	0.009	< D.L.	0.001	0.001	0.003	0.003	0.019
94-030	0.004	< D.L.	0.006	< D.L.	0.061	< D.L.	0.011	0.003	0.011	0.008	0.090
94-031	0.002	< D.L.	0.003	< D.L.	0.012	< D.L.	0.002	0.004	0.006	0.003	0.034
94-037	0.002	< D.L.	0.001	< D.L.	0.018	< D.L.	0.002	0.002	0.007	0.005	0.143
94-046	0.005	< D.L.	0.001	< D.L.	0.055	0.001	0.007	0.003	0.009	0.007	0.039
94-078	0.006	< D.L.	0.000	< D.L.	0.285	0.001	0.008	0.002	0.012	0.042	0.340
95-002	0.006	< D.L.	0.002	< D.L.	0.011	0.001	0.010	< D.L.	0.013	0.011	0.055
95-003	0.003	< D.L.	0.001	< D.L.	0.026	< D.L.	0.004	< D.L.	0.009	0.009	0.053
95-009	0.003	< D.L.	< D.L.	< D.L.	0.038	< D.L.	0.003	0.001	0.009	0.005	0.024
95-011	0.004	< D.L.	< D.L.	< D.L.	0.018	0.002	0.008	< D.L.	0.008	0.004	0.011
95-012	0.003	< D.L.	0.001	< D.L.	0.011	0.001	0.004	0.003	0.007	0.002	0.007
95-013	0.004	< D.L.	0.000	< D.L.	0.029	0.001	0.004	0.003	0.003	0.002	0.016
95-014	0.003	< D.L.	0.000	< D.L.	0.041	0.001	0.004	0.003	0.007	0.003	0.028
95-015	0.003	< D.L.	0.001	< D.L.	0.027	0.001	0.004	0.003	0.008	0.003	0.018
95-016	0.003	< D.L.	< D.L.	< D.L.	0.007	0.001	0.005	0.002	0.006	0.003	0.010
95-020	0.003	< D.L.	< D.L.	< D.L.	0.009	0.001	0.004	0.002	0.007	0.002	0.009
95-021	0.003	< D.L.	< D.L.	< D.L.	0.010	0.001	0.004	0.002	0.007	0.002	0.012
95-023	0.004	< D.L.	< D.L.	< D.L.	0.008	0.001	0.006	0.002	0.007	0.003	0.025
95-024	0.003	< D.L.	< D.L.	< D.L.	0.049	< D.L.	0.007	< D.L.	0.004	0.002	0.036
95-025	0.003	< D.L.	0.001	< D.L.	0.063	0.001	0.004	0.004	0.007	0.004	0.042
94-007	0.003	< D.L.	< D.L.	< D.L.	0.012	0.001	0.003	0.002	0.007	0.004	0.193
95-017	0.003	< D.L.	< D.L.	< D.L.	0.006	0.000	0.002	0.002	0.007	0.004	0.071
95-011	0.003	< D.L.	< D.L.	< D.L.	0.026	0.001	0.003	< D.L.	0.008	0.003	0.021
95-026	0.004	< D.L.	< D.L.	< D.L.	0.044	< D.L.	0.002	0.001	0.007	0.004	0.051
96-002	0.009	< D.L.	< D.L.	< D.L.	0.001	0.001	0.006	0.002	0.005	0.002	0.013
96-009	0.003	< D.L.	< D.L.	< D.L.	0.013	0.001	0.003	0.001	0.008	0.003	0.014
96-011	0.004	< D.L.	< D.L.	< D.L.	0.014	0.001	0.002	0.002	0.006	0.005	0.017
96-012	0.002	< D.L.	< D.L.	< D.L.	0.008	0.000	0.003	0.002	0.003	0.002	0.006
96-014	0.003	< D.L.	< D.L.	0.001	0.022	< D.L.	0.004	0.002	0.006	0.002	0.017
96-015	0.003	< D.L.	< D.L.	< D.L.	0.012	0.000	0.002	0.002	0.007	0.005	0.025
96-041	0.007	< D.L.	< D.L.	< D.L.	2.000	0.002	0.023	0.004	0.035	0.068	1.403

4.8. RockEval

Since it was not possible to estimate the amount of organic material by petrographic observation, RockEval (Espitalie et al., 1980) was used to find this analytical value. Several values are determined by RockEval and total organic carbon (TOC). S1 expresses the amount of preexisting organic material in the sample. S2 is the residual organic material in the rocks. In other words, it is the potential amount of hydrocarbons that can be generated from the rock with further maturation. Both S1 and S2 are reported in milligrams of hydrocarbons/gram of rock. S3 is the amount of organic CO_2 in the sample, and is reported as milligrams of CO_2/gram of rock. However, this value can be affected by carbonates that readily decompose with heat, such as siderite. Total organic content (TOC) is the sum of S1, S2, and residual TOC and is expressed in weight %.

A RockEval II/TOC Analyzer was used for this analytical technique. Approximately 100 mg of sample was weighed into the sample crucibles and heated to 600°C on a heating ramp of 300°C/minute.

RockEval data show that the BRS has a low organic content. Averaged TOC data is tabulated in Table 4.11 and the raw data is found in Appendix 7. Detection limit is estimated at 0.01 wt%. Most of the samples analyzed at values below the detection limit.

Table 4.11 Average total organic content (TOC) as determined by RockEval

SAMPLE	TOC wt%
AU94-007	0.25
AU94-017	0.21
AU94-022	0.8
AU94-023	0.13
AU94-024	0.18
AU94-030	1.22
AU94-037	0.21
AU94-046	1.62
AU94-062	0.03
AU94-078	0.32
AU94-079	0.07
AU95-002	0.39
AU95-003	0.42
AU95-009	0.06
AU95-011	0.33
AU95-012	0.4
AU95-013	1.06
AU95-014	0.72
AU95-015	0.35
AU95-016	0.17
AU95-017	0
AU95-019	0.12
AU95-020	0.05
AU95-021	0.20
AU95-023	0.18
AU95-024	1.28
AU95-025	2.93

4.9. LECO sulfur

Since the exsolution of H_2S gas is invoked to explain the silicification of proto-BRS sediments (Chapter 5), it is important to determine whether there was a significant amount of sulfur in these rocks. A LECO sulfur determinator SC-32 was used to determine the sulfur content of the BRS.

Ceramic crucibles were placed into the 1500°C furnace to ensure that any contaminant sulfur is burned off. Once the crucibles are cooled, approximately 0.2 g was sample is weighed into the tared crucible, which was then replaced in the hot furnace and the instrument measures the amount of sulfur that is generated from the sample. The analysis cutoff was set at 180 seconds or at 0.391% of the highest peak.

Analytical results for LECO sulfur analysis are found in Table 4.12 Analysis for sulfur content by the LECO method shows that the BRS has a low sulfur content. This again is in accord with petrographic observations, where native sulfur, sulfides, and sulfates were not found in great abundance. Detection limit for this technique is estimated at 0.391 weight % .

Table 4.12 Sulfur content as determined by LECO analysis

Sample	wt % S
AU94-007	0.00548
AU94-017	0.01371
AU94-022	0.04274
AU94-023	< D.L.
AU94-024	< D.L.
AU94-030	0.07482
AU94-031	< D.L.
AU94-037	< D.L.
AU94-046	0.12508
AU94-078	0.05392
AU95-002	0.01262
AU95-003	0.01548
AU95-009	< D.L.
AU95-011	0.00779
AU95-012	0.01215
AU95-013	0.05842
AU95-014	0.03750
AU95-015	0.01226
AU95-016	< D.L.
AU95-024	0.08657
AU95-025	0.18493
AU95-026	0.17529
AU96-012	0.00770
AU96-014	0.02907
AU96-015	0.01307
AU96-041	3.54870

Chapter 5. Experimental Calculations and Chemical Modeling

The question that remains to be answered is why the McMurray Formation has locally undergone silicification to produce the Beaver River sandstone, while the rest of the formation has remained unsilicified. In general, intensely quartz cemented sandstones, such as the BRS of the McMurray Formation, are extremely unusual in rocks that have never been buried below about 1-2 km (Bjorlykke and Egeberg, 1993; Abercrombie et al., 1994). Furthermore, petrographic work has revealed both dissolution and precipitation of silica within a single sample. In order to develop a model that attempts to explain the silicification, it is necessary to understand the conditions under which silica is dissolved, transported and ultimately precipitated. Using experimentally derived expressions for silica solubility, this thesis will attempt to show how temperature, pH, H_2S fugacity, and pressure affect the dissolution and precipitation of silica.

Modern day, vertical fluid flow discharges fluids from depth in the study area, such as a newly discovered spring near the mouth of the Muskeg River (Figure 2.3), and elsewhere in the Athabasca River valley (e.g. Borneuf, 1983). Formation waters from the Elk Point Group have high salinities and are sulfate-rich (Hitchon, 1993). Conversely, fluids from the Beaverhill Lake Group are less saline than those presently discharging in the Athabasca River valley. Therefore, springs discharging fluids more saline than those typical of the Beaverhill Lake Group in the Athabasca River valley likely originated from the Elk Point Group rather than the Waterways Formation of the Beaverhill Lake Group.

Springs in the Athabasca River valley (Ells, 1926; Carrigy, 1959), such as the Saline Lake spring (Borneuf, 1983), and possibly the Muskeg River spring, are elevated in H_2S, implying that the sulfur in these fluids is in the reduced form and is not oxidized as sulfate. There are other factors that are consistent with near-surface waters being in a reduced state. Bitumen (Tsang, 1996), pyrrhotite and marcasite after pyrite are present in the Waterways Formation (Peirce et al., 1998) and an overall vertical change is observed from oxidized evaporites and red beds in the Elk Point Group to reduced marine carbonates in the Beaverhill Lake Group. Therefore, as fluids pass vertically through this redox gradient, sulfate-rich waters originating in the Elk Point and discharging at surface must be reduced. Reduction of SO_4^{-2} to HS^- can occur through bacterial sulfate reduction (BSR) at temperatures below 80 to 100°C with accompanying oxidation of immature organic detritus (Abercrombie and Feng, 1997). The sulfur species most likely to be found in these reducing conditions would be in the –2 oxidation state. Under conditions of near-neutral to basic pH expected in a carbonate-buffered (Waterways Formation) system, the dominant reduced sulfur species in solution is HS^- (Figure 5.1).

As fluids move vertically upwards, pressure decreases, causing volatile species such as H_2S to effervesce. Consider what happens if pressure is reduced in a fluid saturated with HS^- causing effervescence of $H_2S_{(g)}$. The fluid responds through the reaction:

$$HS^-_{(aq)} + H^-_{(aq)} \rightleftharpoons H_2S(g)\uparrow \qquad (1)$$

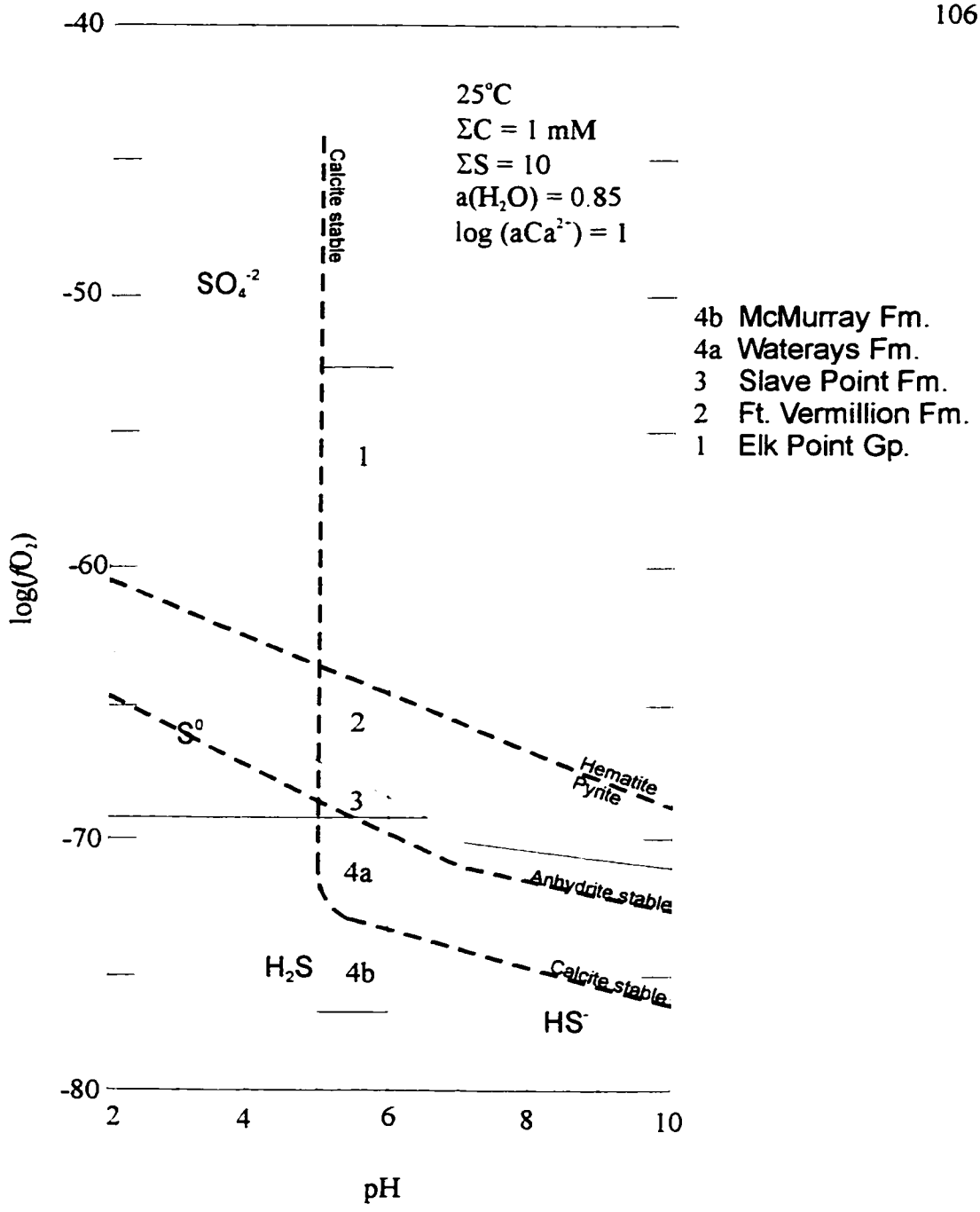

Figure 5.1. pH versus log (fO_2) showing mineral-fluid phase relations in the Fe-C-O-H-S system at 25°C calculated to show the redox conditions throughout the stratigraphic column in the study area. Thin sold lines show the boundaries between predominance fields for sulfur species including native sincerely. Dashed lines show the stability limits for minerals. Numbered regions illustrates conditions prevailing through the stratigraphic column and shows that strong redox contrasts are evident within the stratigraphic column. (Modified after Abercrombie and Feng, 1997).

where the pH of the fluid increases as exsolution of $H_2S_{(g)}$ consumes protons.

The possibility that these reduced fluids have some effect on silica solubility must be considered. As H^- is consumed by H_2S effervescence, there is a corresponding increase in pH. However, the surrounding rock mass acts as a buffer against the change in pH. If this process were to occur within the silica rich matrix of the McMurray Formation, quartz would dissolve in response to H^- consumption. The question at hand is, under the appropriate conditions, how much authigenic silica is produced in response to the resultant shift to higher pH as a result of H_2S effervescence? Equilibrium thermodynamic calculations are used to test this proposed model for the silicification of the McMurray Formation. An additional step would be to model the hydrological consequences of what is proposed. This, however, is beyond the scope of this thesis.

5.1. Silica solubility

Krauskopf (1959) summarizes early experimental work done on the effect of pH on the solubility of silica. He notes that although silica solubility is essentially independent of pH for values below 9 and rises abruptly at higher values, polymerization of dissolved silica is slower at lower pH and therefore the rate at which equilibrium is reached is slower under laboratory conditions. Okamoto et al. (1957) in particular studied the solubility of silica over a wide range of pH and temperature. Their results can be duplicated using equilibrium thermodynamic calculations.

The method used to calculate the relation between the activity of silica as a function of pH is as follows. The three governing reactions for the SiO_2-H_2O system are:

$$SiO_{2(s)} + 2H_2O \rightleftharpoons H_4SiO_4^0{}_{(aq)} \quad (2)$$

$$H_4SiO_4^0{}_{(aq)} \rightleftharpoons H_3SiO_4^-{}_{(aq)} + H^-{}_{(aq)} \quad (3)$$

$$H_3SiO_4^-{}_{(aq)} \rightleftharpoons H_2SiO_{4(aq)}^{-2}{}_{(aq)} + H^-{}_{(aq)} \quad (4)$$

Therefore the mass action equations for the above reactions are:

$$K(SiO_2) = a(H_4SiO_4) \quad (5)$$

$$K(H_4SiO_4) = \frac{a(H^-) \cdot a(H_3SiO_4^-)}{a(H_4SiO_4)} \quad (6)$$

$$K(H_3SiO_4^-) = \frac{a(H^-) \cdot a(H_2SiO_4^{-2})}{a(H_3SiO_4^-)} \quad (7)$$

where a is the activity of the indicated species and K is the equilibrium constant for the corresponding reactions. The equation for the mass balance is:

$$m(SiO_2) = m(H_4SiO_4) + m(H_3SiO_4^-) + m(H_2SiO_4^{-2}) + \ldots \quad (8).$$

However, assuming that the activity coefficients for silica species are unity,

$$m(H_2SiO_4^{-2}) = \frac{K(H_3SiO_4^-) \cdot m(H_3SiO_4^-)}{m(H^-)} \quad (9).$$

Therefore,

$$m(SiO_2) = m(H_4SiO_4) + m(H_3SiO_4^-) + \frac{K(H_3SiO_4^-) \cdot m(H_3SiO_4^-)}{m(H^-)} \quad (10).$$

Because

$$m(H_3SiO_4^-) = \frac{K(H_4SiO_4) \cdot m(H_4SiO_4)}{m(H^-)} \quad (11),$$

then

$$m(SiO_2) = m(H_4SiO_4) + \frac{K(H_4SiO_4) \cdot m(H_4SiO_4)}{m(H^-)} + \frac{K(H_3SiO_4^-) \cdot K(H_4SiO_4) \cdot m(H_4SiO_4)}{m(H^-)} \quad (12).$$

Substituting in (5) gives:

$$m(SiO_2) = K(SiO_2) + \frac{K(H_4SiO_4) \cdot K(SiO_2)}{m(H^-)} + \frac{K(H_3SiO_4^-) \cdot K(H_4SiO_4) \cdot K(SiO_2)}{m(H^-)} \quad (13).$$

The expression is valid where the assumption that the activity coefficients for ali species are unity is valid. Activity coefficients must be calculated for the more general case where $\gamma \neq 1$ and is most easily done using a computer code such as SOLMINEQ88 (Kharaka et al., 1988).

Thermodynamic data from the SOLMINEQ88 database (Kharaka et al., 1988) are used to calculate the activity of silica as a function of acidity and these have been tabulated in Appendix 1. Solubilities of quartz and amorphous silica were calculated to constrain minimum and maximum amounts of silica dissolution, respectively. Chalcedony, cristobalite-a, and cristobalite-b were included for intermediate values between these limits. SiO_2 concentrations for all species increases abruptly at values just below pH 8 (Figures 5.2-5.6), which is similar to the experimental results of Okamoto et al. (1957). Below pH 8, the concentration of silica changes insignificantly at constant temperature for all the silica polymorphs used in this calculation.

Figure 5.2 Activity of silica vs pH for quartz

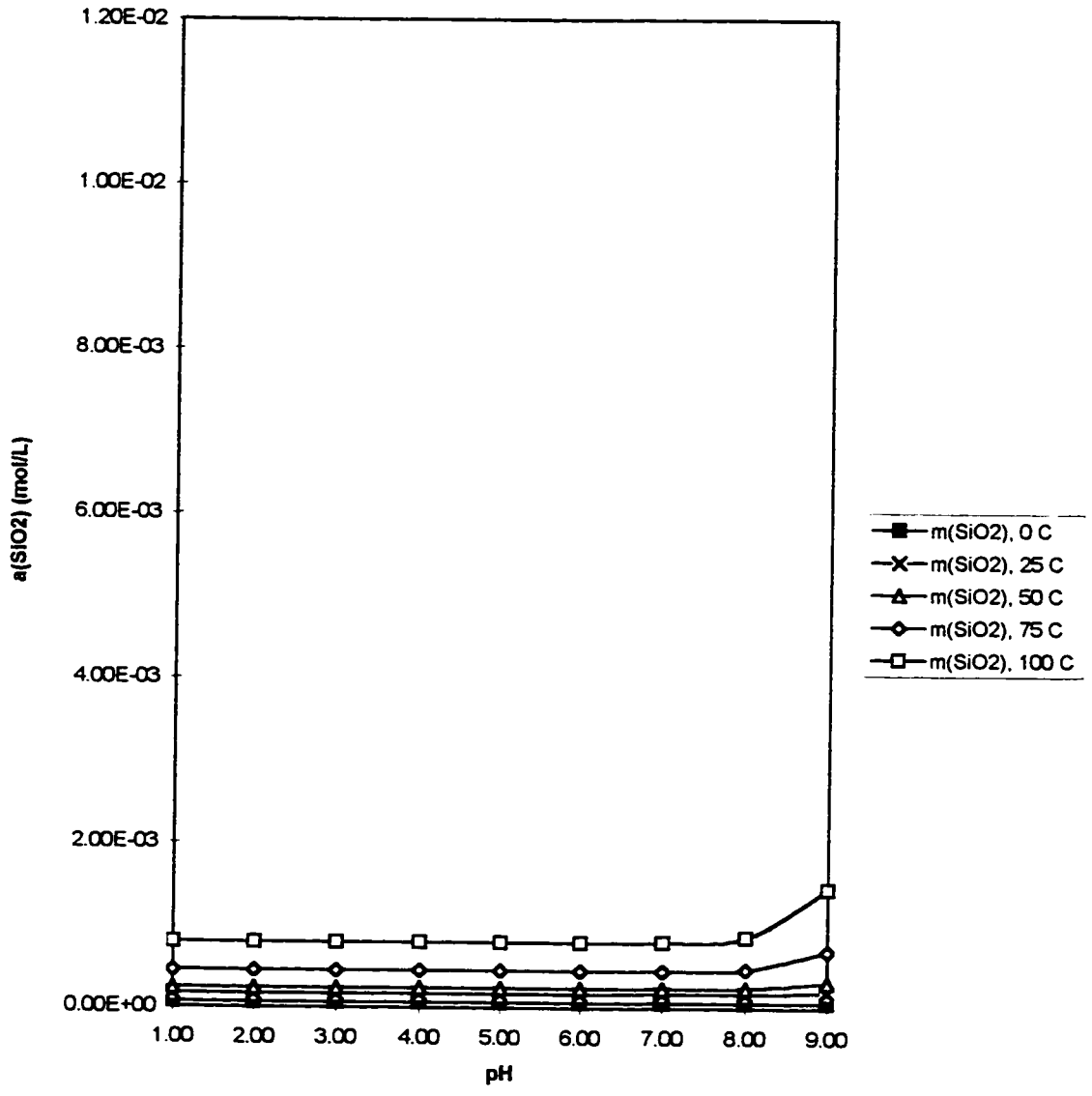

Figure 5.3 Activity of silica vs pH for cristobalite-a

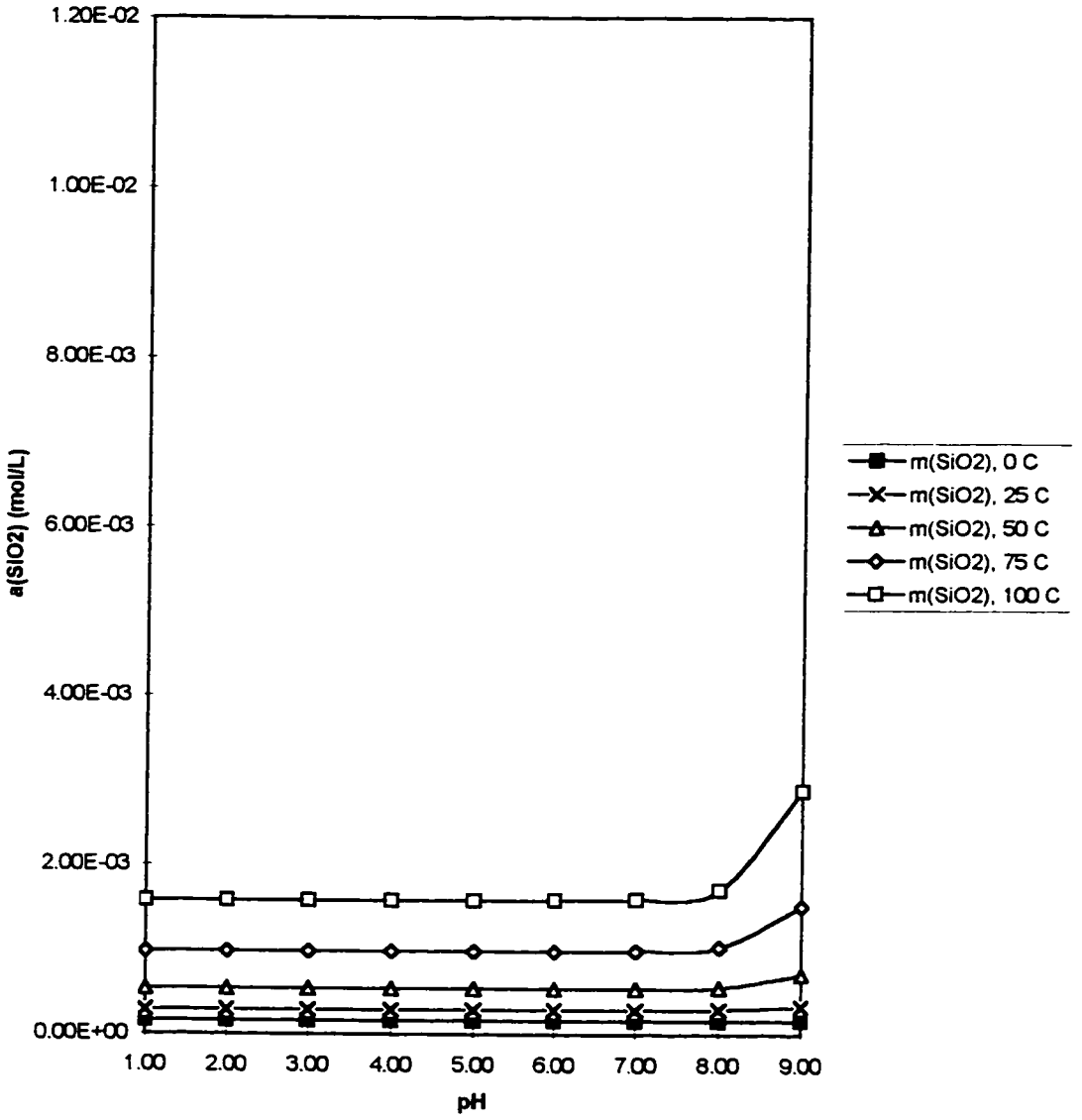

Figure 5.4 Activity of silica vs pH for chalcedony

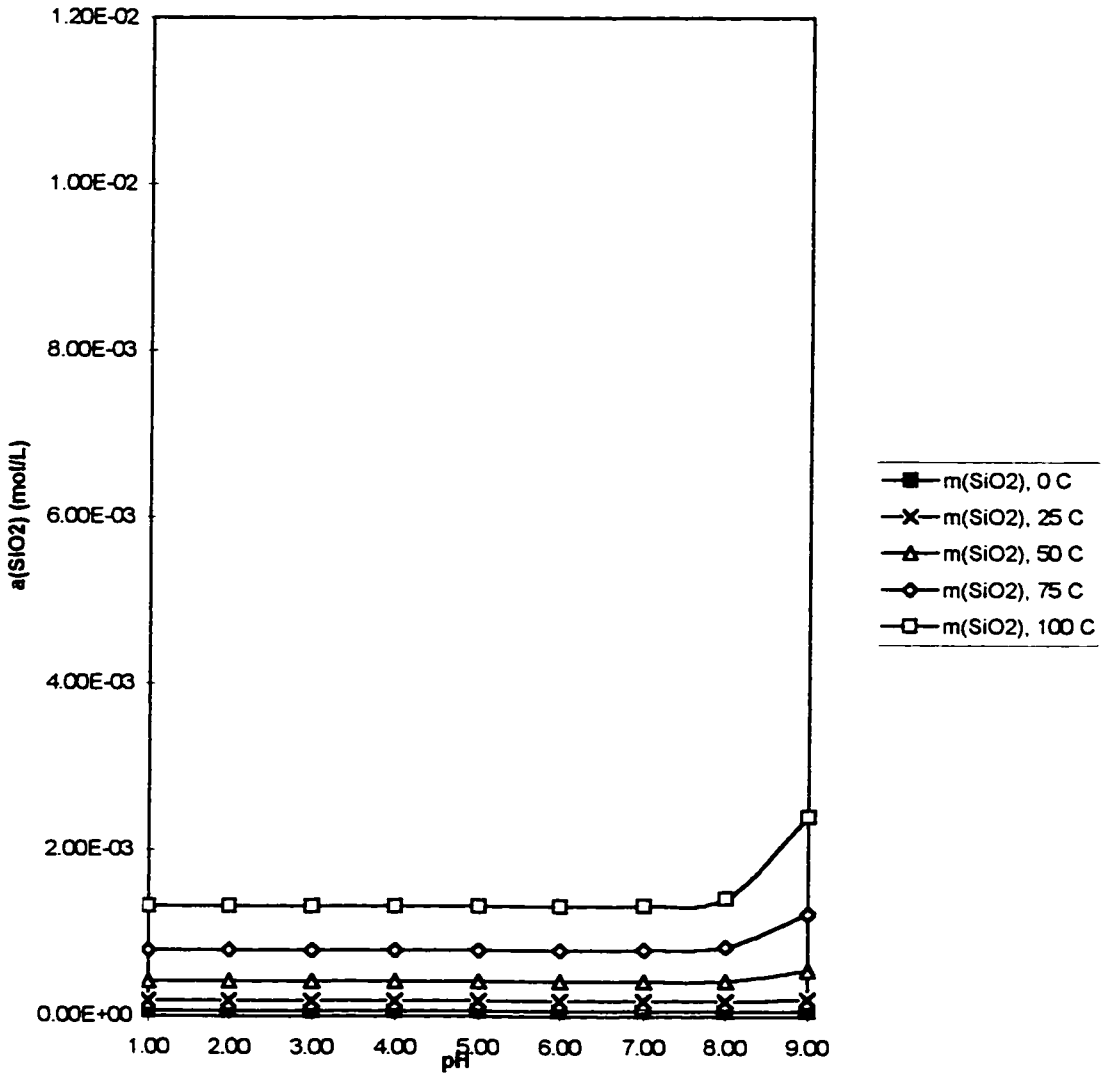

Figure 5.5 Activity of silica vs pH for cristobalite-b

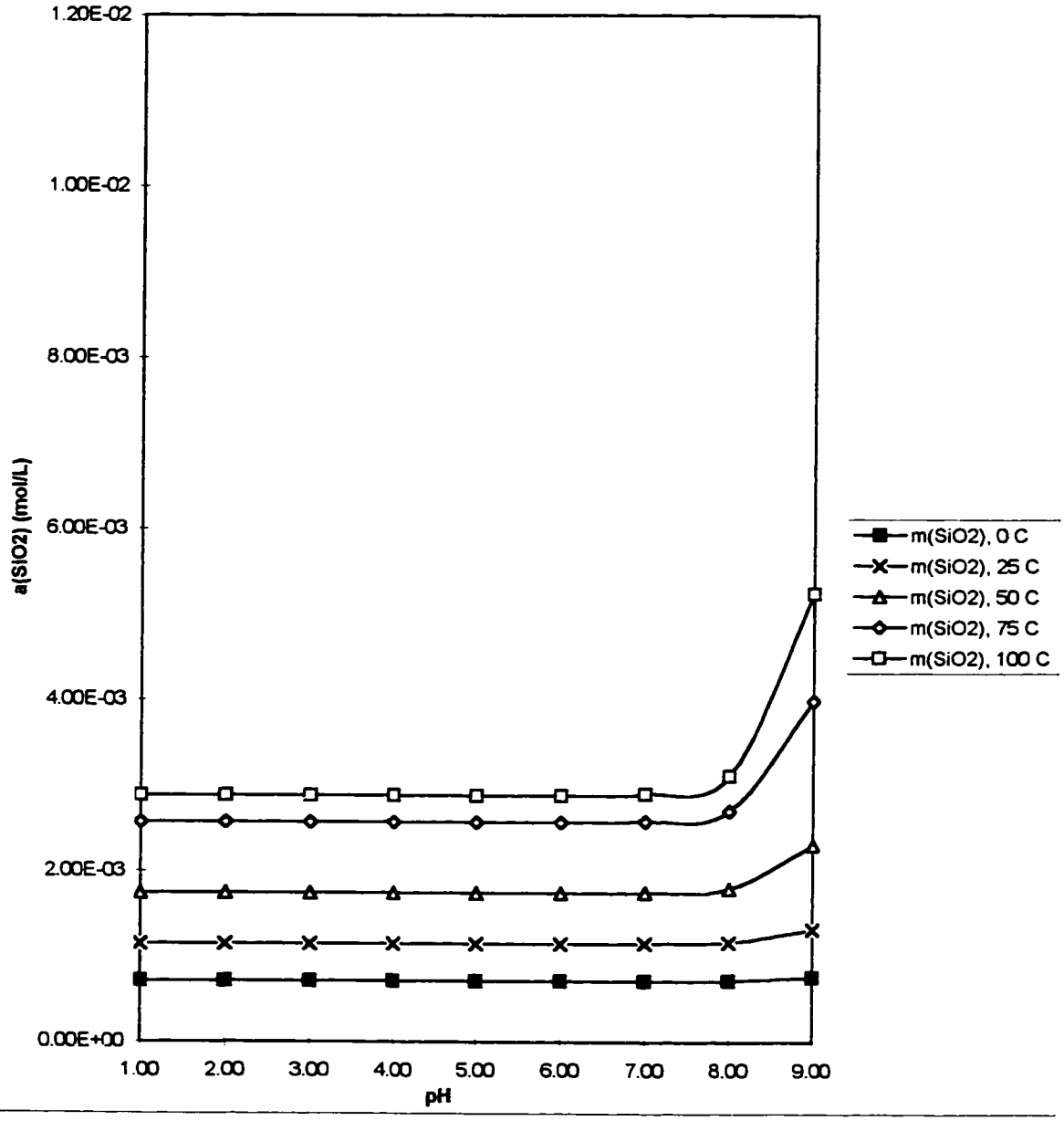

Figure 5.6 Activity of silica vs pH for amorphous silica

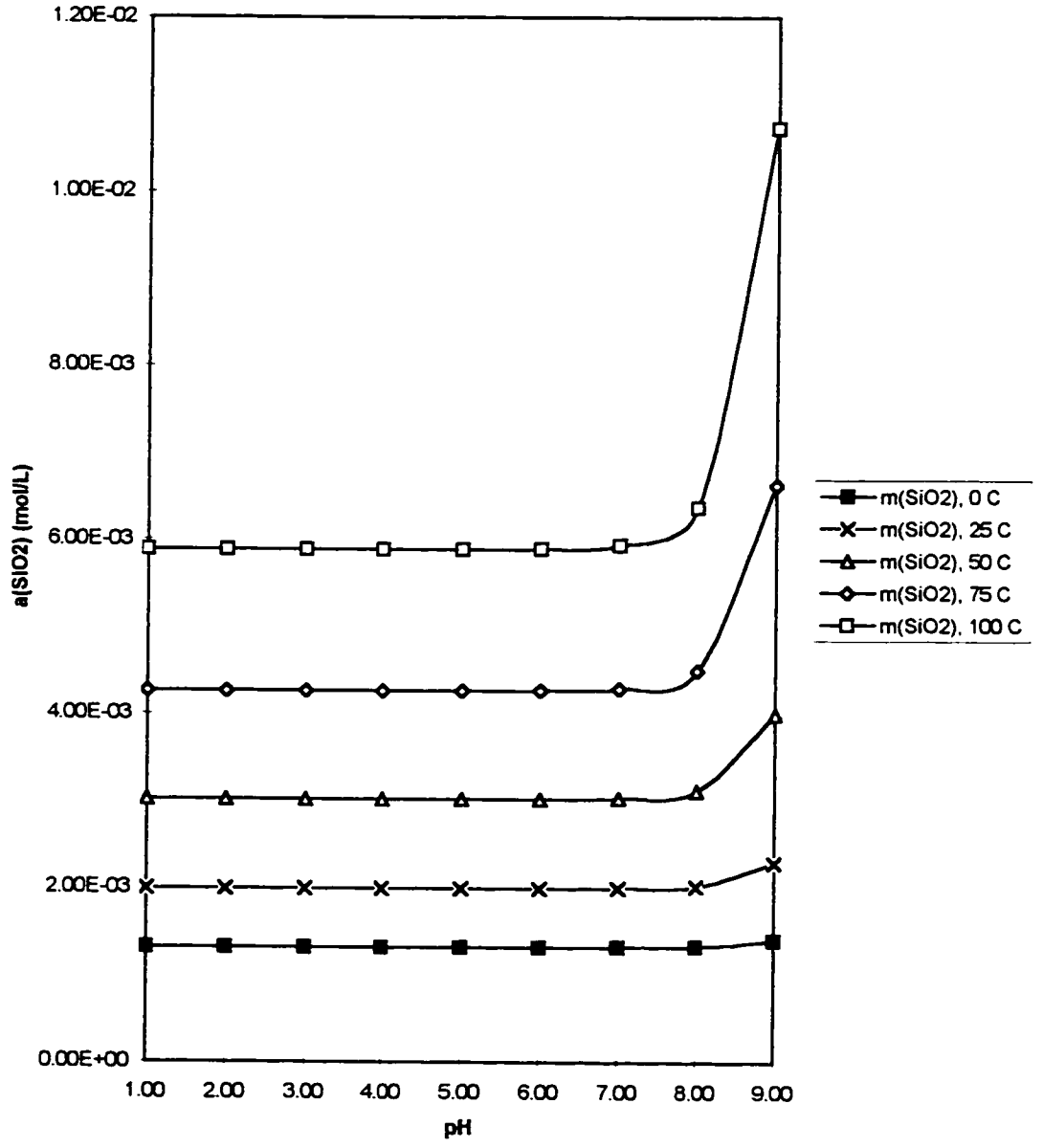

5.2. H_2S solubility

Fournier et al. (1994) suggest that cryptocrystalline quartz or colloidal silica forms as a result of boiling or loss of H_2S when fluids flow upwards. Buchanan (1981) presents a similar mechanism for silicification in epithermal deposits in the southwestern United States, where consumption of H^+ by degassing of H_2S from geothermal fluids increases pH and is related to silicification of vein walls.

In this section, the hypothesis that effervescence of biogenic H_2S has led to silica dissolution will be examined. Barta and Bradley (1985) have presented equations relating the solubility of various gases to gas composition and water salinity, temperature and pressure in saline waters at elevated P and T. Their equations of H_2S gas partitioning are of particular applicability to this thesis. Their method for calculating H_2S solubility (see Appendix 2) as a function of gas partial pressures, temperature, and ionic strength uses the following equations to calculate the molecular interaction parameters for the H_2S-Na-Cl system (Barta and Bradley, 1985):

$$\lambda'_{(H2S,H2S)} = (C_0 + C_1T + C_2T^2 + C_3 \ln T + C_4T \ln T)^2 \quad (14)$$

$$\Delta_{(Na,H2S,Cl)} = C_5 + C_6T + C_7T^2 + C_8 \ln T + C_9T \ln T \quad (15)$$

$$X_{(Na,H2S,Cl)} = C_{10} + C_{11}T + C_{12}T^2 + C_{13} \ln T + C_{14}T \ln T \quad (16).$$

Values for the regression constants (C_o-C_{14}) are given in Table 5.1. At any given temperature T, and salinity $m_{(Na^+)}$, the Henry's Law ratio, k_H, can be calculated using this

equation (Barta and Bradley, 1985):

$$ln\ k_H = \Delta_{Na,CLH2S} m_{Na} + \tfrac{3}{2} X_{Na,CLH2S} m_{Na}^2 + \tfrac{1}{2} ((2m_{Na}\Delta_{Na,CLH2S} + 3X_{Na,CLH2S} m_{Na}^2)^2 + 8\lambda'_{H2S,H2S})^{1/2} \quad (17).$$

The molality of dissolved H_2S can then be calculated using Henry's law (Barta and Bradley, 1985):

$$k_H = \frac{f_{H2S(g)}}{m_{H2S(aq)}} \quad (18)$$

where gas fugacity in vapor phase relative to ideal gas standard state, f, can be calculated using this relation:

$$f = P_K \Phi_{T,P} \quad (19)$$

where P_K is the gas partial pressure and $\Phi_{T,P}$ is the fugacity coefficient at temperature T and pressure P. The method used for calculating $\Phi_{T,P}$ is summarized in Appendix 2.

Using the values tabulated in Table 5.1 and Equation 17, it is possible to calculate the values for λ', Δ, and X at 273 and 298 K summarized in Table 5.2.

The results of the Barta and Bradley (1985) method for calculating the Henry's Law ratio at 25°C for the H_2S-Na-Cl system shown in Figure 5.7 have been summarized in Appendix 2, assuming H_2S pressure is equal to total pressure. The data clearly demonstrate how the solubility of H_2S increases with rising pressure but decreases with increasing salinity. These values will be of use in the next section, where the effect of pH, as controlled by H_2S solubility, is examined for its affect on the solubility of silica.

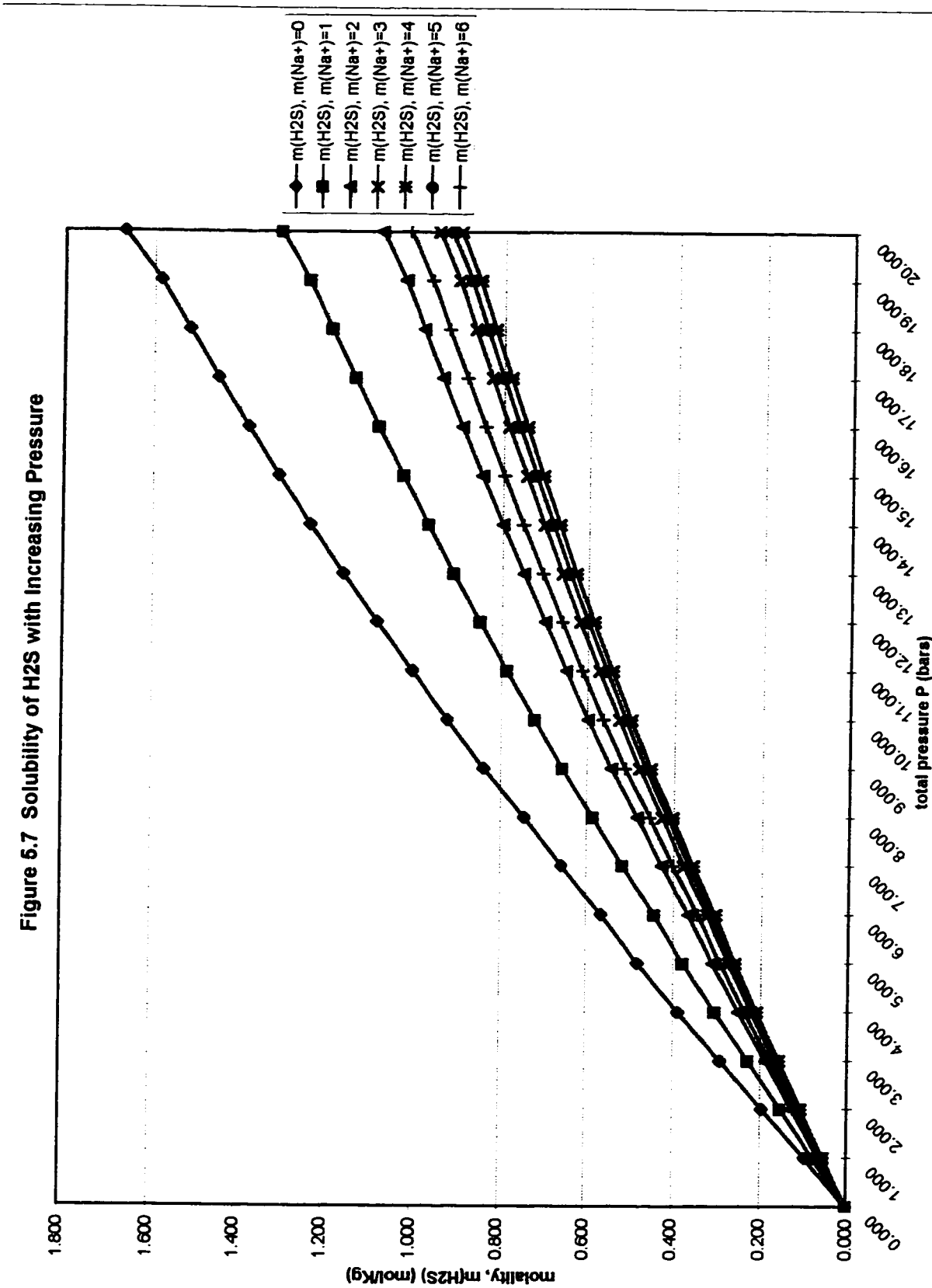

Figure 6.7 Solubility of H2S with Increasing Pressure

Table 5.1. Regression coefficients for calculating H_2S solubility as tabulated by Barta and Bradley (1985).

Coefficient	Value	Standard Deviation†
C_0	-9.527821E2	1.209E2
C_1	-8.154073	1.448
C_2	-6.299369E-4	1.151E-4
C_3	2.62725E2	0.4682E2
C_4	1.144762	0.2093
C_5	1.31462E3	0.1511E3
C_6	11.92594	1.573
C_7	9.432639E-4	1.118E-4
C_8	-3.680454E2	0.4686E2
C_9	-1.681809	0.2067
C_{10}	-1.650661E2	0.3530E2
C_{11}	-1.511839	0.3154
C_{12}	-1.209444E-4	0.2465E-4
C_{13}	46.31658	9.845
C_{14}	0.2134868	0.04439

†Two times the standard error (95% confidence limit).

Table 5.2. Values for λ', Δ, and X calculated at 273 and 298 K.

Temperature, K	$\lambda'_{(H2S,\ H2S)}$	$\Delta_{(Na,H2S,Cl)}$	$X_{(Na,H2S,Cl)}$
273.00	1.06	0.66	-0.07
298.00	2.67	0.26	-0.02

5.3. H_2S degassing and silica dissolution

The above sections describe how silica concentration and H_2S solubility varies with temperature, pressure, salinity and pH. This section will demonstrate how H_2S fugacity affects solution pH and, consequently, how this affects the concentration of silica.

Recall that Equations (2) and (3) from Section 5.1 can express the dissociation of silica:

$$SiO_{2(s)} + 2H_2O \rightleftharpoons H_4SiO_4^0{}_{(aq)} \quad (2)$$

$$H_4SiO_4^0{}_{(aq)} \rightleftharpoons H_3SiO_4^-{}_{(aq)} + H^-{}_{(aq)} \quad (3)$$

Combining these reactions, we get:

$$SiO_{2(s)} + 2H_2O \rightleftharpoons H_3SiO_4^-{}_{(aq)} + H^-{}_{(aq)} \quad (20).$$

Under conditions where pH is controlled by H_2S effervescence, the following reaction applies:

$$HS^-{}_{(aq)} + H^-{}_{(aq)} \rightleftharpoons H_2S_{(aq)} \rightleftharpoons H_2S_{(g)} \quad (21),$$

assuming that the redox chemistry of the fluid is sufficiently reducing and pH is intermediate to basic. If a fluid saturated with dissolved $H_2S_{(g)}$ is allowed to effervesce, equation 21 would shift towards the right to compensate for this change and the fluid chemistry would respond by an increase in pH.

Combining equations 20 and 21 demonstrates how the dissolution of silica is affected by effervescence of $H_2S_{(g)}$:

$$SiO_{2(s)} + 2H_2O + HS^-{}_{(aq)} \rightleftharpoons H_3SiO_4^-{}_{(aq)} + H_2S_{(g)}\uparrow \quad (22).$$

Note that silica is dissolved as the reaction compensates for the removal of H_2S. This reaction, however, assumes that H_4SiO_4 is the only species present that reacts with HS^- in this acid-base reaction. In natural geological systems, this may not be the case. Other mineral buffers such as the carbonate system may be more reactive. Therefore, it is most likely that silica dissolution through effervescence of $H_2S_{(g)}$ occurs within the quartz-rich McMurray Formation and not in the limestones of the Waterways Formation. This is

consistent with petrographic observations, which show dissolution of framework silica grains in the BRS of the McMurray Formation.

Consider a fluid rising to the near surface from a depth of 40 m. As the fluid reaches the surface, pressure decreases and continuous loss of H_2S is predicted. Table 5.3 summarizes the amount of H_2S that can be lost by effervescence from solution at various salinities over a series of 10 m incremental steps. Given the total amount of H^+ consumed, this can be linked to the amount of SiO_2 dissolved in rocks of appropriate lithology.

Table 5.3. Cumulative H_2S loss from 1.0 L solution as pressure decreases for various concentrations of NaCl; method for $f(H_2S)$ calculation shown in Appendix 2.

(a) $m(Na^+) = 0$

Depth (m)	40	30	20	10	0
Pressure (atm)	5	4	3	2	1
$f(H_2S)$	4.85	3.92	2.94	1.98	0.99
$m(H_2S)$	0.48	0.39	0.29	0.20	0.10
H_2S loss		0.09	0.10	0.09	0.10
Cumulative H_2S loss from solution (mol)		0.09	0.19	0.28	0.38

(b) $m(Na^+) = 1$

Depth (m)	40	30	20	10	0
Pressure (atm)	5	4	3	2	1
$f(H_2S)$	4.85	3.92	2.94	1.98	0.99
$m(H_2S)$	0.38	0.31	0.23	0.15	0.08
H_2S loss		0.07	0.08	0.08	0.07
Cumulative H_2S loss from solution (mol)		0.07	0.15	0.23	0.30

Table 5.3. (Continued) Cumulative H_2S loss from 1.0 L solution as pressure decreases concentrations of NaCl; method for $f(H_2S)$ calculation shown in Appendix 2.

(c) $m(Na^+) = 2$

Depth (m)	40	30	20	10	0
Pressure (atm)	5	4	3	2	1
$f(H_2S)$	4.85	3.92	2.94	1.98	0.99
$m(H_2S)$	0.31	0.25	0.19	0.13	0.06
H_2S loss		0.06	0.06	0.06	0.07
Cumulative H_2S loss from solution (mol)		0.06	0.12	0.18	0.25

(d) $m(Na^+) = 3$

Depth (m)	40	30	20	10	0
Pressure (atm)	5	4	3	2	1
$f(H_2S)$	4.85	3.92	2.94	1.98	0.99
$m(H_2S)$	0.27	0.22	0.17	0.11	0.06
H_2S loss		0.05	0.05	0.06	0.05
Cumulative H_2S loss from solution (mol)		0.05	0.10	0.16	0.21

(e) $m(Na^+) = 4$

Depth (m)	40	30	20	10	0
Pressure (atm)	5	4	3	2	1
$f(H_2S)$	4.85	3.92	2.94	1.98	0.99
$m(H_2S)$	0.26	0.21	0.16	0.11	0.05
H_2S loss		0.05	0.05	0.05	0.06
Cumulative H_2S loss from solution (mol)		0.05	0.10	0.15	0.21

(f) $m(Na^+) = 5$

Depth (m)	40	30	20	10	0
Pressure (atm)	5	4	3	2	1
$f(H_2S)$	4.85	3.92	2.94	1.98	0.99
$m(H_2S)$	0.27	0.22	0.16	0.11	0.05
H_2S loss		0.05	0.06	0.05	0.06
Cumulative H_2S loss from solution (mol)		0.05	0.11	0.16	.22

Table 5.3. (Continued) Cumulative H_2S loss from 1.0 L solution as pressure decreases concentrations of NaCl; method for $f(H_2S)$ calculation shown in Appendix 2.

(g) $m(Na^+) = 6$

Depth (m)	40	30	20	10	0
Pressure (atm)	5	4	3	2	1
$f(H_2S)$	4.85	3.92	2.94	1.98	0.99
$m(H_2S)$	0.29	0.24	0.18	0.12	0.06
H_2S loss		0.05	0.06	0.06	0.06
Cumulative H_2S loss from solution (mol)		0.05	0.11	0.17	0.23

SOLMINEQ88 can be used to calculate the amount of silica dissolved by a saline fluid discharging from depth through a series of box-steps, as illustrated in Figure 5.8. Since the fluids discharging from depth in modern day springs are saline, and therefore likely originated from somewhere in the Elk Point Group, formation water from the Keg River aquifer (RCAH116-374D) from Hitchon (1993) was used to generate the starting water.

Table 5.4 summarizes the methodology used for the box-step modeling. The first step was to dilute this water by mixing with different fractions of pure water to generate several starting waters of various salinity. These diluted Keg River formation waters were used as starting waters to test the amount of silica that can be dissolved in each of the different brines. The next step taken was to modify the pH of the system to the condition specified by equilibrium with calcite to simulate equilibrium with limestones of the Waterways Formation. Equilibrium with quartz sand of the McMurray Formation was simulated by imposing equilibration with quartz. The model proposed must be consistent

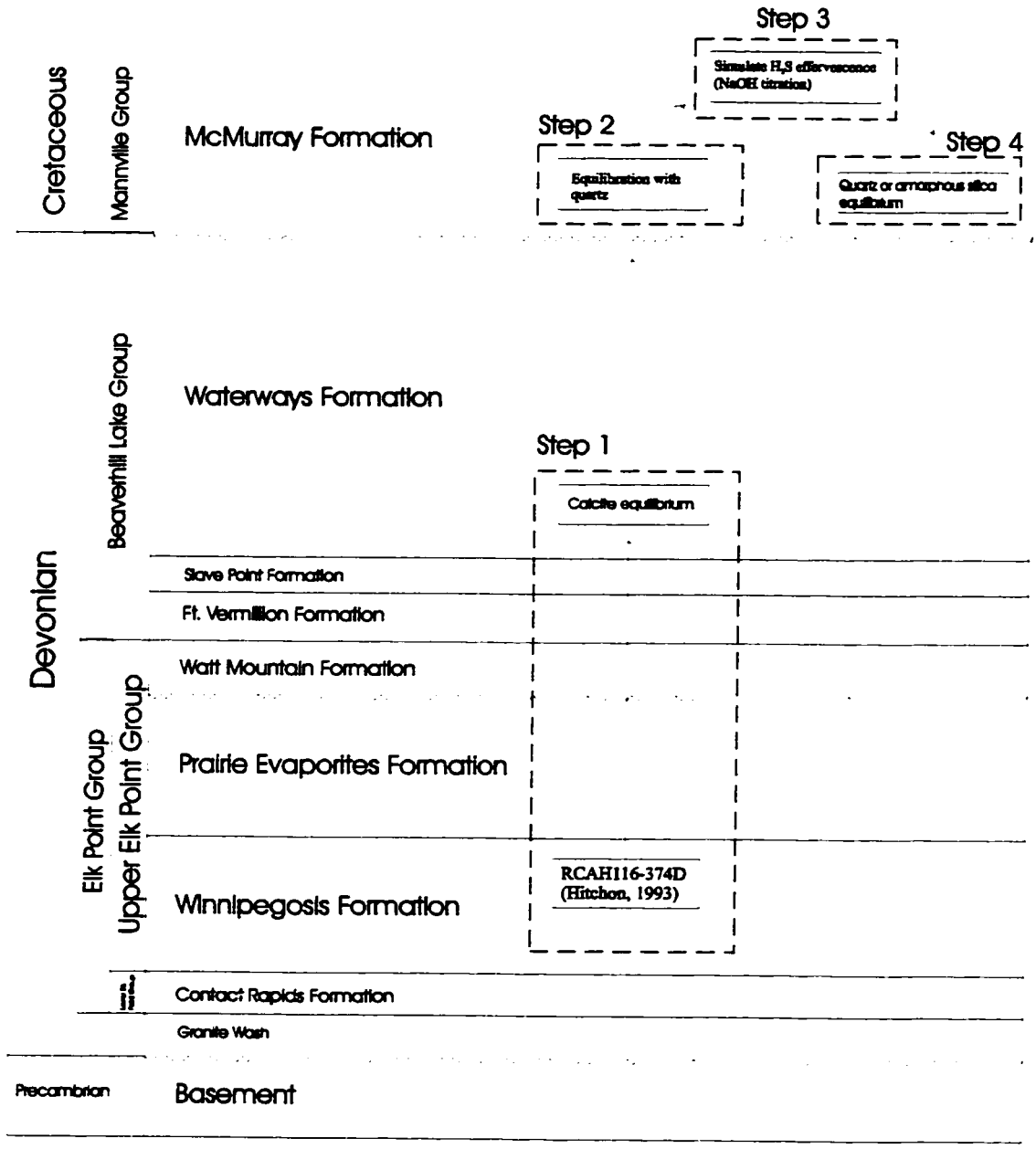

Figure 5.8. Placement of box-steps within stratigraphy controlling geochemical conditions. The starting water was taken from Hitchon (1993) and diluted with pure water so that calculation of dissolved silica at various salinities is made possible. Equilibration with H_2S was simulated by titrating in the amount of H^+ consumed as tabulated in Table 5.3.

with petrographic observation, which shows that authigenic silica in the BRS was likely generated *in situ*. Therefore, the following step simulated the generation of silica within the McMurray Formation by simulating effervescence of H_2S and consumption of H^- at near surface conditions (pressure drop from 2 atm to 1 atm). Adding a specified amount of strong base (NaOH in this case) simulates H^- consumption during effervescence of H_2S. The amount of NaOH titrated into this solution using SOLMINEQ88 is equal to the amount of H^- consumed through a drop in pressure from 2 atm to 1 atm, as tabulated in Table 5.3. The final step was to re-equilibrate the water with a silica polymorph to establish silica dissolution. Only quartz and amorphous silica are considered here to determine the maximum and minimum amounts of silica dissolved.

Table 5.5 summarizes the amount of silica dissolved at various salinities when H_2S is allowed to effervesce. These values indicate that the process modeled can dissolve a large amount of silica with only very little exsolution of $H_2S_{(g)}$.

Table 5.4. Methodology used for SOLMINEQ88 box-step modeling

Step #	Task	Method performed using SOLMINEQ88
1	Generate a starting water.	1. Dilute real water analysis from Hitchon (1993) with pure water. 2. Modify the pH of the solution to the condition specified by equilibrium with calcite.
2	Simulate equilibrium with quartz.	Titrate SiO_2 into the water until at equilibrium with quartz.
3	Effervesce H_2S.	Add a specified amount of NaOH to consume H^- to simulate effervescence of H_2S.
4	Simulate *in situ* dissolution of silica.	Titrate SiO_2 into the water until at equilibrium with quartz/amorphous silica.

Table 5.5. Amount of silica dissolved at various salinities using SOLMINEQ88 to simulate consumption of H^-.

Salinity, m(Na^-)	H^- consumed from 2 atm to 1 atm (mol)	Amount of quartz dissolved (mg/L)	Amount of $SiO_{2(am)}$ dissolved (mg/L)
0	0.10	3298.88	4635.94
1	0.07	1851.46	2830.19
2	0.07	1549.46	2558.43
3	0.05	794.26	1636.29

Salinity, m(Na^-)	Volume of quartz dissolved (mL) in 1 $L^\dagger$	Volume of am. SiO2 dissolved (mL) in 1 $L^\dagger$
0	1.25	2.11
1	0.70	1.29
2	0.59	1.17
3	0.30	0.75

†Density of quartz used is 2.648 g/cc and for amorphous silica is 2.196 g/cc (Greenwood and Earnshaw, 1984).

5.4. Silica precipitation

Once silica is in solution, it is necessary to precipitate the dissolved silica such that the Beaver River sandstone is formed. Assuming that these discharging fluids are able to reach the interface between the groundwater table and the unsaturated zone, meteoric water and dissolved atmospheric CO_2 will play a role in this process. CO_2 dissolved in the groundwater can be represented by this reaction:

$$CO_2 + H_2O \rightleftharpoons H_2CO_3 \quad (23)$$

and

$$H_2CO_3 \rightleftharpoons HCO_3^- + H^- \quad (24).$$

Since the reverse of Equation 20 is desired, we write:

$$H_3SiO_4^- + H^- \rightleftharpoons SiO_{2(s)} + 2H_2O \quad (25).$$

Combining Equations 23, 24, and 25 we get:

$$H_3SiO_4^- + CO_2 \rightleftharpoons SiO_{2(s)} + HCO_3^- + H_2O \quad (26).$$

As the dissolved silica encounters dissolved CO_2 derived from the atmosphere and carried in near-surface groundwaters, a driving force for the precipitation of silica is created. This mechanism is only one of many potential mechanisms, but it is consistent with the petrographic textures documented earlier. Invoking dissolved atmospheric CO_2 as a process leading to silica cementation of the McMurray Formation to produce the Beaver River sandstone would require that the process occurred at or near the water table.

Chapter 6. Discussion and Conclusions

6.1. Experimental calculations

6.1.1. SiO_2 solubility

An understanding of the solubility of silica is useful in determining how silica can be generated *in situ*. It was shown in Chapter 5 that silica solubility varies according to the salinity and the pH of a system for any given silica polymorph. Increasing the salinity of a fluid decreases the amount of dissolved silica. Conversely, increasing the pH of a fluid increases silica solubility. Silica solubility in response to pH changes has been calculated in Chapter 5. It follows from these calculations that, for a given increase in pH, the increase in concentration of dissolved silica is known. H_2S effervescence is invoked as a model for increasing the pH.

6.1.2. H_2S solubility and the affect of H_2S effervescence on the solubility of silica

The method of Barta and Bradley (1985), outlined in Appendix 2, was used to calculate the solubility of H_2S at various pressures and salinities. It is readily obvious that the amount of dissolved H_2S increases as the partial pressure of H_2S increases. As salinity increases, the amount of H_2S dissolved in solution reaches a minimum in a 4 M Na^+ solution.

Using the results of H_2S solubility calculations, SOLMINEQ88 was used to determine the amount of silica that is dissolved within a quartz rich rock, such as the McMurray Formation, through a pressure change from 2 bars to 1 bar. Given that the porosity of an uncompacted sandstone is approximately 26%, or 260,000 mL/m^3 of rock, this must considered as the amount of silica that must be precipitated since very little of the original porosity remains in the BRS, as determined by petrographic observation. Table 5.5 shows that for every liter of H_2S bearing fluid that is discharged, approximately 0.3 to 1 mL of quartz can be dissolved. Assuming that the efficiency of silica precipitation is 100%, on the order of 10^5 liters of H_2S bearing fluid must be discharged to provide 260,000 mL of cement, as tabulated in Table 6.1.

Table 6.1. Volume of H_2S-bearing fluid required to completely silicify a one metre cube of the McMurray Formation to make the Beaver River sandstone.

Salinity, m(Na^+)	Volume of fluid required if quartz was original polymorph (L)	Volume of fluid required if amorphous silica was original polymorph (L)
0	208,000	123,223
1	371,428	201,550
2	440,678	222,222
3	866,667	346,667

McBride (1989) shows that time, space, and silica supply must not be limited in order to form euhedral quartz overgrowths. One or more of these factors must have been limiting if the microcrystalline quartz grains found in the BRS are the incipient euhedral quartz overgrowths described by Pittman (1972) and Carozzi (1960). The question is why

there is such an abundance of the microcrystalline quartz grains. The fine grained nature of these grains suggests that they grew very quickly. Therefore, either many nucleation sites were formed instantaneously, or crystal growth was inhibited, possibly by an interruption of silica supply.

Crystal size is indicative of temperature and rate at which the crystals formed. Microcrystalline cements such as those in the BRS, may be indicative of low temperatures and/or fast rates of crystallization. The polynuclear or "birth and spread" model predicts that many critical nuclei may form simultaneously on surfaces of a relatively large area (Hillig, 1966; Nielsen, 1984). The rate of nucleation, J_n, has been reported by Mullin (1972) as:

$$J_n = A_e \exp(-\Delta G_n^*/kT)$$

where A_e, the pre-exponential term of the homogeneous nucleation rate equation, is also dependent on the supersaturation. ΔG_n^* is the Gibbs formation energy of critical 3-dimensional nuclei. Zhang and Nancollas (1990) used this equation to show that the nucleation rate of crystals is negligible until the solution reaches a "critical supersaturation" (their Figure 2), suggesting that long periods of time can pass before precipitation of crystals occur.

The above equation implies that the rate of nucleation is high if the solution is supersaturated. It stands to reason that there must have been very few nucleation sites prior to the precipitation of silica in the proto-BRS sediments, even when silica-supersaturation persisted. Many nucleation sites must have suddenly been made available to promote crystal growth, resulting in the abundant microcrystalline quartz grains.

Another possibility is that growth of syntaxial, euhedral quartz overgrowths may have been inhibited by clay coatings and/or organic material (Heald and Larese, 1974). Clay coatings are not observed in the BRS and organic material postdates growth of microcrystalline quartz grains so these factors are judged to be inconsequential.

Carozzi (1960) described silica cemented sandstones having a mosaic, quartzitic texture without interlocking quartz grains, which is descriptively similar to the BRS. Unfortunately, he does not suggest reasons for why the cement grows in this fashion. Perhaps the BRS would have developed syntaxial quartz overgrowths except that the supply of silica was somehow interrupted, either by "choking" of the pores through cementation or by a change in the water chemistry. Choking of the pores is consistent with the BRS, because a later pore filling quartz phase occurs.

6.2. Constraints on the origin of the Beaver River sandstone

This section discusses various aspects of the Beaver River sandstone such as distribution, elevation, thickness, mineralogy, analytical geochemistry, paragenesis, and petrography. These observations will be used to limit the range of possibilities for the mechanism of formation of the BRS.

6.2.1. Distribution, elevation and thickness

Figures 2.3 and 2.4 show the outcrop distribution of the BRS. It is apparent that the distribution is scattered and discontinuous, although the areal distribution is generally localized in a north-south linear distribution in the study area. BRS outcrop also appears to be found only near the McMurray-Waterways formations contact, predominantly in the north-central area.

The discontinuous distribution of the BRS could be attributed to erosion of a once continuous body. However, the BRS has pronounced local variations in thickness, is very hard, and is resistant to erosion. If it was originally continuous, then it should be preserved everywhere as a weathering cap for the underlying McMurray Formation. In fact, the Beaver River sandstone is often not present when the McMurray Formation is found in outcrop, as shown in Figure 2.2. Therefore, there is no reason to assume that the BRS was necessarily originally continuous. For this reason, it appears to be more reasonable to suggest that the BRS was originally a discontinuous unit.

Both the elevation and the thickness of the BRS outcrop vary within a small geographic area, as shown in Figure 2.3. In general, the average thickness of the BRS ranges from 70 to 100 cm thick but can be found anywhere from less than 30 cm up to 175 cm thick. The elevation varies through 20 m, ranging from approximately 260 m to 280 m above sea level and an average elevation of 276 m.

There appears to be good correlation between thickness and elevation of the BRS. Where the BRS is higher, it is generally thick; where it is lower, it is generally thin. Similarly, as the BRS rises to the north, it also thins to the north.

The BRS is not observed elsewhere in the WCSB and is apparently unique to the study area. Rocks that have not been subjected to deep burial along the eastern margin of the WCSB are usually not as intensely quartz cemented as the BRS. An exception to this might be the siliceous "sinters" in the Dawson Bay, Manitoba area reported by Fedikow et al. (1996), which occupy a similar stratigraphic position in an area of saline brine discharge.

6.2.2. Mineralogy

The BRS is composed of almost 100% quartz as determined through XRD, optical mineralogy, and SEM. The framework grains in the Beaver River sandstone are composed mainly of quartz. Detailed scanning electron microscopy examination revealed that the matrix is composed of siliceous euhedral to subhedral grains and pore-filling, anhedral material. Some question arose as to what was the mineralogy of the matrix material. Since no other silica polymorph was found by XRD, it is inferred that all the silica in the matrix material is composed of quartz.

XRD and BSE were used to determine that the trace minerals in the BRS are limited to detrital K-feldspars and TiO_2. BSE is especially useful in determining the opaque minerals found on a polished surface. The K-feldspar minerals comprise a small

part of the framework grains. While TiO_2 is also found as a minor component of the framework grains, a fine grained opaque material is often found in the microcrystalline matrix. Using inference from XRD data, it is likely that all TiO_2 minerals are anatase. However, it is not certain whether the fine anatase grains are detrital or authigenic.

6.2.3. Analytical geochemistry

6.2.3.1. Bulk rock geochemistry

Basic rock geochemistry methods such as XRF, RockEval, LECO sulfur, and ILC of 18MΩ H_2O leach analyses were included in the suite of analytical methods to fully characterize the BRS. XRF was useful in determining the major elements found in the BRS. Si and Ti-oxides were the major oxides, which is in accord with the XRD data discussed in the previous section. RockEval was able to determine that the samples on average contain 0.4 wt % total organic carbon content, ranging from 0 to almost 3 wt %. Sulfur analysis using a LECO sulfur analyzer found that the average amount of sulfur in the BRS is 0.1%, ranging from 0 to 3.7%. A method was developed to analyze for soluble salts in the BRS. The analytical results suggest that very little to no salts are present in the samples analyzed.

RockEval, LECO, and the method developed for ILC are simply additional analytical techniques that further support the XRD and XRF results, where the most

common mineral in the BRS is quartz, and that very little of anything else is present in the BRS.

6.2.3.2. Precious metal geochemistry

Since native Ni, Pt-rimmed Ni grains and Pt grains were found in the BRS during BSE investigation, standard industry analytical techniques were used to determine the amount of precious metals present in the samples. Samples were sent for fire assay-directly coupled plasma (FA-DCP), induced neutron activation analysis (INAA), and total digestion-inductively coupled plasma-mass spectrometry (TD-ICP-MS). An additional method, laser ablation-inductively coupled plasma-mass spectrometry (LA-ICP-MS) was done at GSC-Calgary for verification of these methods. These methods all suggest that the metals contained in the BRS are at values near or below detection limit.

6.2.4. Petrography

The matrix of the BRS is made up of microcrystalline quartz grains. Euhedral microcrystalline grains range in size from $\leq$ 5 μm to 100 μm, but have a bimodal distribution around 5 μm and 20 μm. Microcrystalline quartz grains with pristine, unabraded surfaces are abundant in the BRS. Less well-developed subhedral microcrystalline grains were also observed in the BRS. However, these grains only range

in size from < 2 μm to 5 μm in diameter. Pore-filling anhedral quartz is found within the matrix of these authigenic euhedral and subhedral microcrystalline quartz grains.

Fluid inclusions in the matrix material in the BRS are very rare; likely because of the fine grained nature of the matrix material. However, those that were found are composed of an aqueous phase. No organic phase was found in the fluid inclusions.

6.2.5. Paragenesis of the Beaver River sandstone

Detailed SEM examination of BRS rock chips revealed that the cement has two distinct textures. Euhedral and subhedral microcrystalline quartz grains are found embedded in a late, pore filling anhedral quartz cement. The euhedral and subhedral microcrystalline grains fill the pore space created by the framework grains while the anhedral quartz cement fills the remainder of the free space. Textures also suggest that episodic dissolution and precipitation of silica occurred during the formation of the BRS.

Partially filled and unfilled pore spaces are also observed. Interestingly, these unfilled pore spaces create geopetal textures, where it appears as though the microcrystalline quartz grains have settled out of solution and collected on the bottom of the pore space.

Fine grained TiO_2 grains were observed in the interstices of the framework grains during BSE-SEM investigation of thin sections. These tiny grains were found concentrated along grain edges, and, most convincingly, in pore spaces creating geopetal textures. These textures appear to be created after crystals had formed *in situ* and then

collected at the bottom of an open pore space, similar to the microcrystalline quartz grains. TiO_2 is interpreted to be sourced from detrital grains through *in situ* solution and precipitation, analogous to the silica grains. This conclusion was drawn when detrital TiO_2 grains were found in a partially dissolved stage.

As mentioned previously, no silica polymorph other than quartz is found in the BRS, suggesting two possibilities. The first is that silica was initially precipitated as some low crystallinity silica polymorph, which later recrystallized to quartz. The other possibility is that quartz was the original silica polymorph precipitated. Assuming nuclei are available, quartz can precipitate directly from solution if the fluid is at or above quartz saturation and is undersaturated with respect to kinetically favored silica polymorphs (Morey et al, 1962; MacKenzie and Gees, 1971; Kastner et al, 1977; Hesse, 1989; M. Kastner, written communication, 1997). However, if amorphous silica is at or above saturation, it is likely that quartz was not the original polymorph formed since the rate of quartz precipitation is slower than the rate of precipitation of amorphous silica.

Consider the following scenario. Amorphous silica was the original polymorph precipitated. Early recrystallization to quartz formed the microcrystalline quartz grains with pristine, unabraded faces. A volumetric reduction of the neoformed material accompanies recrystallization because of the difference in density of the various silica polymorphs. A later episode of precipitation of pore-filling silica would result in the total choking of the pores. The previously formed quartz grains would act as nuclei, so that this later episode of silica would crystallize as quartz.

Celikkaya and Akinc (1990) document the formation of bimodal size distribution of ZnS aggregates, which grew through the collection of ZnS crystallites (Ostwald ripening). By controlling temperature, pH, and the concentration of Zn and S sources, they were able to control the rate of production of ZnS crystallites relative to the rate of growth of larger ZnS aggregates. Once the crystallites reached a critical concentration, a second population of smaller aggregates began to form, resulting in a bimodal distribution of ZnS aggregates. There exists a bimodal distribution of neoformed quartz grains in the BRS. It is possible that the growth of euhedral quartz grains grew through a similar mechanism by incorporating the smaller subhedral quartz grains into the larger euhedral quartz grains.

Textures suggesting *in situ* dissolution and precipitation of silica are found in the BRS. A model involving the degassing of H_2S is proposed as a mechanism for dissolving silica. To do this, the solubility of H_2S was also investigated using the method outlined by Barta and Bradley (1985). It is believed that this is a valid mechanism for the study area because modern day springs are found in and near the study area that are reportedly elevated in H_2S (Borneuf, 1983; Hitchon, 1993). The question at hand is whether the degassing of H_2S produces a sufficient change in pH to dissolve enough silica to generate the amount of authigenic silica found in the BRS. The work presented in Chapter 5 suggests that this is indeed possible.

6.3. Classification of the Beaver River sandstone

Since the BRS appears to be unique to the WCSB, it follows that a unique mechanism must have occurred in order for the silica alteration to occur. The physical characteristics of the BRS have been discussed in the previous section. It is now possible to use these constraints to classify the Beaver River sandstone.

M. Dufresne (personal communication) suggested that the Beaver River sandstone is a sinter cap, similar to those related to the Carlin microdisseminated gold deposit in Nevada. Alternatively, F. Krause (personal communication) suggested that the BRS could be a ganister, based on petrographic observations. A completely different scenario is one where the microcrystalline quartz grains are not due to any kind of geochemical alteration. Rather, they might be considered to be of detrital origin. These suppositions will be addressed in the sections below.

6.3.1. Is the Beaver River sandstone detrital in origin?

There is no doubt that the framework grains in the BRS are detrital in origin. However, the euhedral and subhedral microcrystalline quartz grains and the pore-filling anhedral quartz are not. Euhedral grains have pristine, unabraded surfaces, which is not consistent with a detrital origin. Euhedral and subhedral microcrystalline quartz grains are found embedded in pore-filling anhedral quartz, which also does not suggest that these grains are detrital in origin.

If the microcrystalline quartz grains were detrital, and had been deposited at the same time as the framework sand grains, the BRS should be situated at the same stratigraphic level. This would require the BRS to be distributed as a relatively flat surface, assuming original horizontality. However, this is not the case. Figure 2.3 shows that the elevation of BRS outcrop varies up to 20 m vertically and the thickness ranges from less than 30 cm thick up to 175 cm thick, all within a very limited geographic area. It does not seem reasonable to suggest that the BRS, or specifically the silicification of the McMurray Formation, is detrital in origin.

6.3.2. Is the Beaver River sandstone a silcrete?

"Silcrete" is a generic term used for describing silica cemented surficial sediment (Bates and Jackson, 1987). Summerfield (1983a) rejects the notion that silcretes invariably form in arid or semi-arid climate (non-weathering profile-type soil environments), and suggests that silicification can also occur in humid climates in highly acidic, poorly drained weathering environments (weathering profile-type soil environments). "Weathering profile-type silcretes" are Ti-rich (>1% TiO_2) and are characterized by humid, low pH environments. Non-weathering profile-type silcretes are Ti-poor and are indicative of high-pH, semiarid to arid environments (Summerfield, 1983a,b). The somewhat Ti-rich BRS is consistent with the Ti-rich "weathering profile-type silcrete". However, *in situ* dissolution of framework grains in the BRS conflicts with

the low pH environments required for these types of silcretes, as is shown by silica solubility calculations.

Langford-Smith (1978) documented the field properties of fresh, unweathered silcretes as:

> "...*usually grey, but the colour may vary considerably and can be whitish, red, brown, or yellow. Fresh silcrete, when struck with a hammer, gives a very characteristic ring and a pungent odor. It is extremely brittle, and shatters readily into sharp, angular pieces with a conchoidal fracture. Newly-broken rocks have a semi-vitreous sheen.*
>
> *When in place, beds of silcrete are usually 1 to 2 m thick, but on occasion may be 5 m or more. Vertical jointing is almost invariably present, and usually gives rise to a columnar structure. Sub-horizontal jointing is also common, but tends to be discontinuous.*"

Although the discussion above demonstrates that silcretes are lithologically similar to the BRS, it is necessary to differentiate lithology and mode of formation. The mode of formation must be considered to correctly categorize one type of silica concretion from the next. As such, it is speculative to classify the Beaver River sandstone as a particular kind of silcrete, such as a ganister or a sinter, until a viable mechanism that clearly and correctly demonstrates the processes responsible for silicification has been determined.

6.3.3. Is the Beaver River sandstone a ganister?

Ganisters are fine grained, well sorted, closely packed, subangular, highly siliceous, silica cemented quartz sandstones which commonly occur as the seat earth[1] soil below a coal seam. Carbonaceous traces of rootlets are common in ganisters, which form by silica enrichment during pedogenesis (Percival, 1983a). The parent material must contain <95% quartz prior to pedogenic leaching and >95% quartz due to enrichment by leaching in a moderately well drained, upper horizon paleosol profile. The unsilicified material is usually, but not necessarily, associated with an organic matter cover, a vegetation cover, or coal seams (Percival, 1983a; Retallack, 1988; Gibling and Rust, 1992).

True ganisters are essentially fossilized A2 horizons[2] of modern podzols and podzolic soils. A2 horizons form under freely drained conditions, when precipitation exceeds evapotranspiration, and are associated with an organic matter/vegetation cover (the A2 horizon is generally leached of organic material, which can be fine particles or coatings on minerals, and therefore has less organic content than the A1 horizon).

---

[1] Seat earth: A British term for a bed of rock underlying a coal seam, representing an old soil that supported the vegetation from which the coal was formed; specifically underclay. A highly siliceous seat earth is known as a ganister (Bates and Jackson, 1987).

[2] A-horizon: A mineral horizon formed or forming at or adjacent to the surface that either:
1. Shows an accumulation of humified organic matter intimately associated with the mineral fraction, or
2. Has morphology acquired by soil formation but lacks the properties of E and B-horizons.
The organic matter in A-horizons is well decomposed and is either distributed as fine particles or is present as coatings on the mineral particles. As a result A horizons are normally darker than the adjacent underlying horizons. In warm, arid climates where there is only slight or virtually no accumulation of organic matter, surface horizons may be less dark than adjacent underlying horizons. If the surface horizon has a morphology distinct from that of the assumed parent material and lacks features characteristic of E and B horizons, it is designated as an A horizon on account of its surface location (FitzPatrick, 1983).

The Firestone Sill Ganister, which was produced by pedogenic leaching of subarkosic sand parent material, never exceeds 1.5 m thickness (Percival, 1983b). The BRS rarely exceeds 130 cm, but can be found up to 175 cm thick. The Firestone Sill Ganister has a large spatial occurrence and rapid variations in lithology (e.g. quartz arenite directly overlying a sub-arkosic sandstone) which suggests a pedogenic origin as opposed to a sedimentary origin (Percival, 1983b). Lamar (1953) suggested the leaching of siliceous limestone or calcareous chert forms the ganister deposit found in the Hartline "formation" in southern Illinois.

A ganister is differentiated from other silcretes by the lack of abundant cherty, cryptocrystalline or opaline silica cement, lack of evidence of near surface cementation, and lack of TiO_2-rich cloudy areas (Percival, 1982, 1983a). However, Gibling and Rust (1992) reported authigenic formation of iron and titanium oxides, silica, and siderite, plus the alteration of some detrital grains and clay minerals as the major pedogenic processes that occurred during ganister formation in the Waddens Cove Formation. Therefore, there still exists some discrepancy regarding the physical description of a ganister. Classification of texturally mature quartz arenitic sandstone as a ganister depends on the presence of several criteria; Percival (1983a) mentions those listed in Table 6.2.

It difficult to know which of the criteria in Table 6.1 should be used to classify silicified sediment as a ganister. Many physical characteristics of the BRS, such as the formation of isolated sandstone layers capping thicker sandstone bodies, the general thickness of the outcrop, and the presence of TiO_2 (anatase)-rich cloudy areas, are similar to ganisters. So the question at hand is whether the BRS should be classified as a

ganister. Silica solution and precipitation have occurred locally within the McMurray Formation in the proto-BRS sediments. Petrographic observations of dissolution and precipitation of silica suggests mineral leaching occurred, as required for ganister genesis. Gibling and Rust (1992) suggest that textures similar to pedogenic ganisters would be observed if microquartz cementation of the proto-ganister sediments is associated with phreatic, silica rich groundwater at shallow depth, where dissolved atmospheric CO_2 likely provides the driving force for silica precipitation. These characteristics suggest that the BRS is a ganister, whereas other features such as evidence of soil profiles and pedogenic leaching are not observed. It is likely that there exists more than one method of early silica cementation of unconsolidated sediments. For this reason, it is probable that rocks such as the Beaver River sandstone, although petrographically similar to ganisters, can be produced through dissimilar processes.

6.3.4. Is the Beaver River sandstone a sinter?

Radtke (1985) described silica alteration at the Carlin Mine as fine-grained hydrothermal silica that occurred as a late phase alteration. The host carbonate rocks had undergone moderate to intense hydrothermal dissolution prior to, as well as during, silica alteration. Hydrothermal silica seams and patches formed where dissolution occurred prior to silicification of the host carbonate rocks; jasperoid bodies formed where late stage dissolution and silicification were coeval. The silica alteration results in the metasomatic replacement of silty, fossiliferous dolomite (i.e. a jasperoid). Radtke (1985) believes the

siliceous seams formed along faults and fractures, and thin or pinch-out away from the main structures. Armstrong et al. (1987) report jasperoids in the Carlin area typically contain euhedral quartz crystals coated by fine grains of iron oxides.

St. John and Cummings (1992) report on the active formation of sinters, as well as fossil sinter terraces at Mickey Hot Springs, Oregon. These sinters can be up to 1.5 m thick and directly overly fine-grained unconsolidated silty sand, which, descriptively, is similar to the Beaver River sandstone. Active springs at Mickey Hot Springs range in temperature from 56°C-96°C and have a field pH of approximately 8.

Table 6.2. Criteria needed for ganister classification and textures observed in the BRS.

Ganister Characteristic from Percival (1982)	BRS Observations
Roots and rootlets are present, but usually decrease in abundance with depth.	Roots and rootlets are present (Fenton and Ives, 1990).
Evidence for soil horizons: The top is commonly a thin coal that overlies a quartz arenite horizon, which in turn overlies a clay enriched zone (the clay content decreases with depth). The clay enriched zone is commonly referred to as a "cutan" (Brewer, 1964). Cutans commonly occur as clay coatings and pore linings.	No clay coatings, no soil horizons, and no coal layer in outcrop; however, Fenton and Ives (1990) reported that root molds, coal laminae and a highly variable lithology directly underlies the BRS.
The base of the quartz arenite can be either a sharp or a transitional contact. When the contact is transitional, the underlying sandstone is commonly texturally and mineralogically less mature. Sharp contacts have irregular bases with undulations up to a few tens of cm deep.	Both gradational (Fenton and Ives, 1990) and sharp contact at base (this study).
Sedimentary structures are absent due to bioturbation (rootlets and soil organisms) and other pedogenic processes.	Roots and rootlets present (Fenton and Ives, 1990). Sedimentary structures sometimes present.
The quartz arenite is commonly thin, generally < 1 m, but up to 2 m in extreme cases. Large variations in the thickness of the quartz arenite horizon are generally due to the irregular basal contact.	Variation in thickness ranges from less than 30 cm up to 175cm thick.
Vertical and lateral changes in the lithology of the quartz arenite horizon are due to variations in leaching. The frequency of easily weathered minerals such as feldspars and micas is low in the quartz arenite horizon.	No variation in quartz arenite horizon; mineralogy is quite uniform, with quartz being the dominant lithology (>95%).
Absence of any marine fauna in the quartz arenite.	No marine fauna observed.
Features indicating high energy reworking are lacking (e.g. well rounded, well sorted grains).	The BRS is composed of subrounded to angular framework grains.

Mass transfer of silica via hydrothermal fluids has long been documented as a process for silica transport (e.g. Fournier, 1984). The hydrothermal system at Carlin implies that transport of silica occurred over some distance rather than originating from a local silica source. Radtke (1985) suggests that if shallow mobilization and redeposition of silica had occurred, then evidence must be shown for local depletion of silica. This evidence was not found at Carlin.

Evidence of silica alteration such as quartz veining in basement granitoids (Feng and Abercrombie, 1994) and chalcedony laths in the limestones (G. de Paoli, personal communication, 1997) has been observed in the Ft. McKay area. SEM photomicrographs presented in Chapter 3 show ragged and pitted detrital grain edges and euhedral microcrystalline quartz grains, which are indicative of local dissolution and precipitation. These textures are good evidence for silica transport within the study area, both *in situ* and at depth. Although temperature has been demonstrated to be a factor that can increase the silica solubility, no evidence has been found to suggest that temperature was a major factor in the silicification of the Beaver River sandstone.

6.3.5. Silicification of the Beaver River sandstone

The discussion above describes how the BRS is similar to other silica cemented surficial deposits. For instance, the BRS is similar to the generic description given for a silcrete. Yet it is only partially consistent with the Ti-rich weathering profile-type silcrete. In fact, the low pH environment of this type of silcrete is in direct contradiction to the

silica solubility calculations. The BRS is more compatible with the non-weathering profile-type silcrete, where high pH environments occur. This type of silcrete is also indicative of arid to semi-arid environments. During times of McMurray deposition in a fluvial/deltaic depositional environment, it does not seem likely that an arid to semi-arid environment occurred. Although, the BRS resembles the physical description of silcretes, this is insufficient ground for classification as a silcrete.

Sinters form in hydrothermal environments, such as the hydrothermal system at the Carlin Mine in Nevada and the fossil sinter terraces at Mickey Hot Springs, Oregon. However, these, and other hydrothermal systems, occur at temperatures relatively higher than the temperatures to which the study area has been subjected. No evidence for elevated temperatures has been observed within the study area. Nonetheless, the fossil sinter terraces at Mickey Hot Springs are descriptively similar to the BRS. However, again, these are insufficient grounds for classification.

Although the method of formation of a ganister was not found in the literature, it seems as though many of these types of deposits are associated with coal deposits. Although coal is found in the Firebag member of the Waterways Formation, large coal deposits within the McMurray Formation are not common. Moreover, there is no evidence that the BRS is actually a fossilized portion of a paleo-soil horizon.

It seems that the BRS does not fit into any of the categories suggested above. Perhaps it is timely to propose a different scenario to explain the silicification of the BRS. Abercrombie and Feng (1997) suggest that the Beaver River sandstone is a record of warm, somewhat alkaline fluids that carried elevated amounts of dissolved silica into the

basal McMurray Formation that discharged along localized fracture zones in the underlying Waterways Formation limestones. Petrographic observations, however, are inconsistent with this scenario and suggest that the silica likely originated from a local source. The *in situ* dissolution of quartz grains can be explained by invoking H_2S effervescence as a mechanism for silica dissolution. Petrographic observations show that precipitation of authigenic silica occurred, possibly as amorphous silica followed by very early recrystallization forming euhedral and subhedral microcrystalline quartz grains. Formation of these microcrystalline quartz grains was followed by later precipitation of pore-filling anhedral quartz. Although many mechanisms may be invoked to explain the pronounced variation in thickness over a small geographic area, the simplest scenario is that the BRS is thickest nearest the point of focused fluid discharge and H_2S effervescence.

As H_2S effervesces, the pH increases, causing *in situ* dissolution of silica. Periodic desiccation of pore fluids increases the relative dissolved SiO_2 concentration. Variable pore fluid chemistry occurring due to episodic H_2S effervescence would cause chemical conditions to fluctuate from more acidic to more basic conditions. In either case, a driving force for silica precipitation is created.

Allowing for periodic desiccation of these silica rich pore fluids, or periodic fluctuation of water chemistry, geopetal textures might form as euhedral and subhedral quartz crystals form and fall to the bottom of the pore space. Although desiccation arguably may or may not have occurred, dissolved atmospheric CO_2 as a driving force

would provide a strong buffering capacity and therefore would lower the pH of this system.

6.4. Discrepancy between SEM and PGE assays

All standard analytical techniques such as fire assay and neutron activation found that the BRS contained very little to undetectable amounts of platinum. However, many rock chips were found to contain several native Ni grains, Ni grains rimmed with Pt, and Pt grains by BSE-SEM.

The precious metal assay analyses are not consistent with the detailed examination of the samples. For this reason, an acid digestion sample preparatory technique for ICP-MS analysis was undertaken in an attempt to find a method that was able to process many samples quickly and efficiently. Although a combination of H_2O_2, HF, HNO_3, and HCl was found that was able to digest 0.1 gram samples, the turn around time for analysis and the results were not encouraging.

Cabri and Laflamme (1981) warn that routine PGE analyses on similar samples must be developed through experience, which can be considered more reliable than analyses on single or few samples when there is no or little prior analytical background. Anyone attempting to develop new analytical methods should be forewarned that it is a time consuming, effortful task and the problems of analysis should not be taken lightly. O'Neill et al. (1996) report a method for quantitative analysis of PGEs and Au in silicate rock matrices using a cation exchange/ultrasonic inductively coupled plasma-mass

spectrometry (USN-ICP-MS) technique. Their technique uses sample sizes of ≤ 50 mg. However, they stress that a rigorous sample homogenization is necessary before the samples are processed, making for a rather time consuming and tedious method. Development of a similar methodology was beyond the scope of this thesis.

6.5. Conclusions

The Beaver River sandstone has been studied by various methods. These include field investigations, petrographic and textural observations, and analytical geochemistry.

Field investigations reveal that the BRS occurs as discontinuous outcrop. The variation in thickness and elevation over a small geographic area suggest that the microcrystalline quartz matrix is not detrital in origin.

Scanning electron microscopy was found to be most useful in the petrographic and textural examinations. Using this technique, it was possible to determine that the matrix in the BRS is composed of unabraded, euhedral to subhedral microcrystalline quartz grains. These grains are embedded in late, pore-filling anhedral quartz cement. Textures found in the matrix suggest this material formed *in situ*, and is not detrital in nature. Framework grains with dissolution textures were found using transmitted light microscopy and SEM suggesting that *in situ* dissolution of the framework grains occurred.

A mechanism was proposed to explain the silicification of the proto-BRS sediments. Groundwater springs near the study area discharge H_2S rich fluids from depth (Ells, 1926; Carrigy, 1959; Borneuf, 1983; Hitchon, 1993). Bitumen, pyrrhotite and

marcasite after pyrite are found in the Waterways Formation. Redox conditions exhibit an overall change from oxidizing evaporites in the Elk Point Group to reducing carbonates in the Beaverhill Lake Group. These factors suggest that reducing conditions likely prevail in the fluids discharging from depth. This is accompanied by a decrease in pressure, resulting in H_2S effervescence, which causes an increase in pH. The overall effect of H_2S effervescence is an increase in silica solubility. In fact, in order to fully silicify unconsolidated, uncompacted sand that has an average original porosity of 26%, on the order of 10^5 liters of HS^- bearing fluid must be discharged per cubic meter of rock.

Several methods were used to characterize the samples for whole-rock analytical geochemistry. The mineralogy was found to be almost all quartz with trace amounts of anatase (TiO_2) and K-feldspars. Industry standard techniques such as neutron activation and fire assay were used to determine the precious metal content of the BRS. Although a method preparing pulped BRS samples by acid digestion in an industrial microwave was attempted, the turn-around time and results of the analyses resulted in this method being abandoned. Other methods of sample preparation, such as the one described by O'Neill et al. (1996) for USE-ICP-MS should be investigated. Adding a microwave digestion to their technique would likely increase the efficiency of the method.

6.6. Further work

Although BSE investigations suggests that the rocks contain Pt, Ni and other native metals, the problem of quantitative determination of PGEs has not been resolved

here. An exhaustive search of reliable methods that gives a reasonable analytical result for PGEs and Au in the BRS should be investigated.

The role of authigenic TiO_2 should be investigated since it seems to play a role not only in ganister genesis, but also BRS formation. Calculations including TiO_2 as an additional mineral that responds to variations in water chemistry should be considered. Also, precious metals such as the PGEs and Au and base metals such as Ni should also be added to the species included in solubility calculations. Do precious metals like Pt, Ni, and Cr also precipitate/mineralize as native metals? How is this affected by fresh/meteoric waters, which are usually oxidized? The presence of Ni suggests that deposition had to occur under highly reducing conditions (D. Pattison, personal communication).

Surdam and Crossey (1987) developed a temperature-dependent model showing that quartz cementation occurs in two episodes, one between 20° and 80 °C and one at temperatures greater than 160°C. However, McBride (1989) suggests that quartz cementation occurs over a greater range than what Surdam and Crossey (1987) claim, but rarely under 40°C. Kirkland (1993) found quartz overgrowths formed between 40 and 70 °C in the Kiskatinaw Formation in the Peace River area using fluid inclusion data. Similar studies on fluid inclusions, as well as apatite fission track studies, need to be done in order to constrain the temperatures under which the quartz cement formed in the Beaver River sandstone. Fluid inclusion studies would also help in determining the salinity of the fluid from which the microcrystalline quartz cements were formed. However, this will not be an easy task since few fluid inclusions were observed in thin section.

Petrographic study shows that in situ dissolution of framework grains occurred, and is likely the silica source of the authigenic microcrystalline quartz grains. However, it is unclear whether or not the volume of quartz preserved in the BRS was entirely derived from local sources. Therefore, detailed investigation of detrital silica grains proximal to BRS deposits should be investigated, where these grains are suspected to be an additional source of silica. Textural studies of quartz and clays in underlying Devonian limestone should also be considered.

References

Abercrombie, H.J. and R. Feng, 1997. Geological setting and origin of microdisseminated Au-Ag-Cu minerals, Fort MacKay region, northeastern Alberta. *In:* Macqueen, R.W., Exploring for minerals in Alberta: Geological Survey of Canada Geoscience contributions, Canada-Alberta agreement on mineral development (1992-1995), GSC Bulletin 500, pp. 247-276.

Abercrombie, H.J., I.E. Hutcheon, J.D. Bloch, P. de Caritat, 1994. Silica Activity and the Smectite-Illite Reaction. Geology, vol. 22, pp. 539-542.

Armstrong, A.K., Bagby, W.C., Ekburg, C., and Repetski, J., 1987. Petrographic and Scanning Electron Microscope Studies of Samples from the Roberts Mountains and Popovich Formations, Carlin Mine Area, Eureka County, Nevada. U.S.G.S Bull. 1684.

Bjorlykke, K. and P.K. Egeberg, 1993. Quartz Cementation in Sedimentary Basins. AAPG Bull., vol. 77, pp. 1538-1578.

Barta, L. and D.J. Bradley, 1985. Extension of the Specific Interaction Model to Include Gas Solubilities in High Temperature Brines. Geochimica et Cosmochimica Acta, vol.49, pp. 195-203.

Bates, R.L. and J.A. Jackson, 1987. Glossary of Geology, 3rd Ed. American Geological Institute, Alexandria, Virginia.

Bennett, P.C., 1991. Quartz dissolution in organic-rich aqueous systems. Geochimica et Cosmochimica Acta. vol. 55, pp. 1781-1797.

Benthin, H.L., 1973. Conventional oil possibilities in the Fort McMurray area. *In:* M.A. Carrigy (Ed.), Guide to the Athabasca Oil Sands area. Alberta Research Information Series 65, pp. 165-172.

Borneuf, D., 1983. Springs of Alberta. Alberta Research Council, Earth Sciences Report vol 82-3, 95 pp.

Buchanan, L.J., Precious Metal Deposits Associated with Volcanic Environments in the Southwest. *In:* W.R. Dickinson and W.D. Payne (Eds.), Relations of Tectonics to Ore Deposits in the Southern Cordillera. Arizona Geological Society Digest, vol. XIV, pp. 237-262.

Cabri, L.J. and J.H.G. Laflamme, 1981. Sample preparation techniques for PGE-bearing elements. *In:* Cabri, L.J. (Ed), Platinum-group elements; mineralogy, geology,

recovery, Special Volume – Canadian Institute of Mining and Metallurgy, vol. 23, pp. 151-173.

Cant, D.J., and B. Abrahamson, 1996. Regional distribution and internal stratigraphy of the Lower Mannville. Bulletin of Canadian Petroleum Geology, vol. 44, no. 3, pp. 508-529.

Carozzi, A.V., 1960. Microscopic Sedimentary Petrography. John Wiley & Sons, Inc., New York.

Carrigy, M.A., 1959. Geology of the McMurray Formation: Part III, General geology of the McMurray area. Research Council of Alberta, Geological Division, Memoir 1. 130 pp.

Carrigy, M.A., 1966. Lithology of the Athabasca Oil Sands. Alberta Geological Survey, Alberta Research Council, Bulletin 18, 48 pp.

Carrigy, M.A., 1973. Mesozoic Geology of the Fort McMurray area; *In:* M.A. Carrigy and J.W. Kramers (Eds.), Guide to the Athabasca Oil Sands Area, Alberta Research Council Information Series 65, pp. 77-101.

Celikkaya, A. and M. Akinc, 1990. J. Amer. Ceramic Soc., vol. 73, p. 245.

Celikkaya, A. and M. Akinc, 1990. J. Amer. Ceramic Soc., vol. 73, p 2360.

Cotterill, D.K., and W.N. Hamilton, 1995. Geology of Devonian limestones in Northeast Alberta, Alberta Geological Survey, Alberta Research Council, Open File Report 1995-07.

Crickmay, C.H., 1957. Elucidation of Some Western Canada Devonian Formations. Published by the author, Imperial Oil LTD., Calgary.

DePaoli, G., 1996. Unpublished data.

Dienert, F., and W. Wandenbulcke, 1923. Sur le dosage de la silice dans les eaux. Compt. Rend., vol. 176, p. 1478-1480.

Dove, P.M., 1995. Kinetic and Thermodynamic Controls on Silica Reactivity in Weathering Environments. *In:* A.F. White and S.L. Brantley (Eds.), Chemical Weathering Rates of Silicate Minerals, pp. 235-290.

Durand, B., 1987. Understanding the Hydrocarbon Migration in Sedimentary Basins (Present State of Knowledge). Advanced Organic Geochemistry, vol. 13, pp. 445-459.

Espitalie, J., M. Madec, and B. Tissot, 1980. Role of mineral matrix in kerogen pyrolysis; influence on petroleum generation and migration. AAPG Bulletin, vol 64, no. 1, pp. 59-66.

Fedikow, M.A.F., R.K. Bezys, J.D. Bamburak, and H.J. Abercrombie, 1996. Prairie-type microdisseminated Au mineralization - a new deposit type in Manitoba's Phanerozoic rocks (NTS 63C/14). Manitoba Energy and Mines, Minerals Division, Report of Activities, 1996 p. 108-121.

Fenton, M.M. and J.W. Ives, 1982. Preliminary Observations on the Geological Origins of Beaver River Sandstone. Archeological Survey of Alberta, Occ. Pap. no. 19, pp. 166-189.

Fenton, M.M. and J.W. Ives, 1984. The Stratigraphic Position of Beaver River Sandstone. Archeological Survey of Alberta, Occ. Pap. no. 23, pp. 128-136.

Fenton, M.M. and Ives, J.W., 1990. Geoarchaeological Studies of the Beaver River Sandstone, Northeastern Alberta. *In:* N.P. Lasca and J. Donahue (Eds.), Archaeological Geology of North America: Boulder, Colorado, Geological Society of America, Centennial Special Volume 4,. pp. 123-135.

Feng, R. and H.J. Abercrombie, 1994. Disseminated Au-Ag-Cu mineralization in the Western Canadian Sedimentary Basin, For MacKay, northeastern Alberta: A new gold deposit type. *In:* Current Research 1994-E; Geological Survey of Canada, pp. 121-132.

Ferris, F.G., 1990. Immobilization and Mineralization of Metallic Ions by Bacteria. Energy Sources, vol. 12, pp. 371-375.

Ferris, F.G., W.S. Fyfe, and T.J. Beveridge, 1988. Metallic Ion Binding by *Bacillus subtilis*: Implications for the Fossilization of Microorganisms. Geology, vol. 16, pp. 149-152.

Fournier, R.O., 1984. The Behavior of Silica in Hydrothermal Solutions. *In:* B.R. Berger and P.M. Bethke (Eds.), Geology and Geochemistry of Epithemal Systems, pp. 45-62.

Gibling, M.J. and B.R. Rust, 1992. Silica-Cemented Paleosols (Ganisters) in the Pennsylvanian Waddens Cove Formation, Nova Scotia, Canada. *In:* K.H. Wolf

and G.V. Chilingarian (Eds.), Diagenesis, III. Developments in Sedimentology, vol. 47, pp. 621-655.

Greenberg, S.A. and E.W. Price, 1957. The Solubility of Silica in Solutions of Electrolytes. Journal of Physical Chemistry, vol. 61, pp. 1539-1541.

Greenwood, N.N. and A. Earnshaw, 1984. Chemistry of the Elements. Pergamon Press, Oxford, England. p. 395.

Hackbarth, D.A. and N. Nastasa, 1979. The Hydrogeology of the Athabasca Oil Sands Area, Alberta. Alberta Research Council, Bull. 38.

Heald, M.T., and R.E. Larese, 1974. Influence of coatings on quartz cementation. Journal of Sedimentary Petrology, vol. 44, no. 4, pp. 1269-1274.

Hesse, R., 1989. Silica Diagenesis: Origin of Inorganic and Replacement Cherts. Earth Science Reviews, vol. 26, pp. 253-284.

Hillig, W.B., 1966. A derivation of classical two-dimension nucleation kinetics and the associated crystal growth laws. Acta Metall. vol. 14, pp. 1868-1869.

Hitchon, B., 1993. Geochemistry of formation waters, Northern Alberta, Canada: Their relation to the Pine Point ore deposit. Alberta Geological Survey, Open File Report 1993-14.

Hitchon, B., A.A. Levinson, and S.W. Reeder, 1969. Regional Variations of River Water Composition Resulting from Halite Solution, MacKenzie River Drainage Basin, Canada. Water Resources Res. 5, pp. 1395-1403.

Iler, R.K., 1955. The colloid chemistry of silica and silicates. xii.

Iler, R.K., 1979. The Chemistry of Silica. John Wiley & Sons, New York, New York. pp. 3-104.

Ives, J.W. and M.M. Fenton, 1983. Continued research on the geological sources of the Beaver River Sandstone source study: Archaeological Survey of Alberta Occasional Paper, 21, pp. 78-88.

Ives, J.W. and M.M. Fenton, 1985. Progress report for the Beaver River Sandstone geological source study: Permit 83-54, final report; Report on file, Permit 83-54, Archaeological Survey of Alberta, 69 p.

James, D. P., 1977. The Sedimentology of the McMurray Formation, East Athabasca. Master's Thesis, University of Calgary, Calgary, Alberta, 198 pp.

Kastner, M., J.B. Keene, and J.M. Gieskes, 1977. Diagenesis of Siliceous Oozes - I. Chemical Controls on the Rate or Opal-A to Opal-CT Transformation - An Experimental Study. Geochimica et Cosmochimica Acta, vol. 41, pp. 1041-1059.

Kastner, M., J.M. Gieskes, and E.I. Bromley, 1978. Hydrothermal Experiments on Silica Diagenesis. EOS, p. 307.

Keith, T.E.C., 1992. A look at silica phases in evolving hydrothermal systems. *In:* Kharaka, Y.K. and A.S. Maest (Eds.), Proceedings – International Symposium on Water-Rock Interaction, 7; pp. 1423-1426.

Kharaka, Y.K., W.D. Gunter, P.K. Aggarwal, E.H. Perkins, and J.D. DeBraal, 1988. SOLMINEQ.88: A Computer Program for Geochemical Modeling of Water-Rock Interactions. U.S.G.S. Water-Resources Investigations Report 88-4227, 420 pp.

King, R.B. (Editor in Chief) (1994). Encyclopedia of Inorganic Chemistry, vol. 8. John Wiley and Sons, West Sussex, England, p. 4204.

Kirkland, I. K., 1993. Diagenesis of the Mississippian (Viséan) Kiskatinaw Formation, Peace River area, Alberta. University of Calgary. Dept. of Geology and Geophysics.

Konhauser, K.O., W.S. Fyfe, F.G. Ferris, and T.J. Beveridge, 1993. Metals Sorption and the Mineral Precipitation by Bacteria in Two Amazonian River Systems: Rio Solimoes and Rio Negro, Brazil. Geology, vol. 21, pp. 1103-1106.

Krauskopf, K.B., 1956. Dissolution and precipitation of silica at low temperatures. Geochimica et Cosmochimica Acta, vol. 10, no. 1-2, pp. 1-26.

Krauskopf, K.B., 1959. The Geochemistry of Silica in Sedimentary Environments. Society of Economic Paleontologists and Mineralogists. Special Publication, no. 7, pp. 4-19.

Lamar, J.E., 1953. Siliceous Materials of Extreme Southern Illinois: Silica, Novaculite, Ganister, Calico rock, and Chert Gravels. Illinois State Geological Survey, Report of Investigations, no. 166, 39pp.

Langford-Smith, T., 1978. A select review of silcrete research in Australia. *In:* Langford-Smith, T. (Ed.), Silcrete in Australia, pp. 1-11.

MacKenzie, F.T. and R. Gees, 1971. Quartz: Synthesis at Earth-Surface Conditions. Science, vol. 173, pp. 533-534.

McBride, E.F., 1989. Quartz Cement in Sandstones: A Review. Earth Science Reviews, vol. 26, pp. 69-112.

McGookey, D.P., J.D. Haun, L.A. Hale, H.G. Goodell, D.G. McCubbin, R.J. Weimer, and G.R.Wulf, 1972. Cretaceous system. *In:* W.W. Mallory (Ed.), Geologic atlas of the Rock Mountain region, U.S.A.: denver, Rocky Mountain Association of Geologists, pp. 190-228.

Mellon, G.B., and Wall, J.H., 1956. Foraminifera of the Upper McMurray and Basal Clearwater Formations. Geology of the McMurray Formation. Research Council of Alberta, Report. 72, Part. I, p. 1-29.

Morey, G.W., Fournier, R.O., and Rowe, J.J., 1962. The Solubility of Quartz in Water in the Temperature Interval from 25 to 300°C. Geochimica et Cosmochimica Acta. vol. 22, pp. 1029-1043.

Mullin, J.W., 1972. Crystallization. Butterworths, London.

Nielsen, R.L., 1984. Evolution of porphyry copper ore deposit models. Mining Engineering, vol. 36, no. 12, pp. 1637-1641.

Nordstrom, D.K. and J.L. Munoz, 1985. Geochemical Thermodynamics. The Benjamin/Cummings Publishing Co., Inc. p 23 and p.133.

Norris, A.W., 1963. Devonian Stratigraphy of Northeastern Alberta and Northwestern Saskatchewan. GSC Memoir 313. pp. 2-39.

Okamoto, G., T. Okura, K. Goto, 1957. Properties of Silica in Water. Geochimica et Cosmochimica Acta., vol. 12, pp. 123-132.

O'Connell, S.C. 1994. Geological history of the Peace River Arch. *In:* Mossop, G. and I. Shetsen (Compilers.), Geological Atlas of the Western Canada Sedimentary Basin. pp. 431-438.

O'Neill, J.A. Jr., C.R. Neal and J.C. Jain, 1996. Addressing Heterogeneous Distribution and Trace Abundances of Platinum Group Elements (PGEs) and Gold (Au) in Silicate Rock Matrixes (sic): Quantitative Analyses Using

Ultrasonic Inductively Coupled Plasma- Mass Spectrometry (USN-ICP-MS). EOS Transactions. Vol. 77, No. 46.

Peirce, J.W., S.A. Goussev, R.A. Charters, H.J. Abercrombie, and G. DePaoli, 1998. Intrasedimentary magentization by vertical fluid flow and exotic geochemistry. The Leading Edge, pp. 89-92.

Percival, C.J., 1983a. A definition of the Term Ganister. Geological Magazine, vol. 120, pp. 187-190.

Percival, C.J., 1983b. The Firestone Sill Ganister, Namurian, Northern England - The A2 horizon of a Podzol or Podzolic Palaeosol. Sedimentary Geology, vol. 36, pp. 41-49.

Pittman, E.D., 1972. Diagenesis of Quartz in Sandstones as Revealed by Scanning Electron Microscopy. Journal of Sedimentary Petrology, vol. 42, no. 3, pp. 507-519.

Price, R.A. 1994. Cordilleran Tectonics and the Evolution of the Western Canada Sedimentary Basin. *In:* Mossop, G. and I. Shetsen (Compilers.), Geological Atlas of the Western Canada Sedimentary Basin. pp. 431-438.

Radtke, A.S., 1985. Geology of the Carlin Gold Deposit, Nevada. U.S.G.S. Prof. Pap. 1267, 124 pp.

Renders, P.J.N., and H.L. Barnes, 1989. Hydrothermal Precipitation of Cristobalite at 200°C. Geological Society of America, Annual Meeting, p. A103.

Retallack, G.J., 1988. Field Recognition of Paleosols. *In:* R. Juergen and W.R. Sigleo (Eds.), Paleosols and Weathering Through Geologic Time; Principles and Applications, GSA Special Paper, vol. 216, pp. 1-20.

Rimstidt, J.D. and H.L. Barnes, 1980. The Kinetics of Silica-Water Reactions. Geochimica et Cosmochimica Acta, vol. 44, pp. 1683-1699.

Robert, R.V.D., Van Wyk, E. and Steele, T.W., 1975. The Effects of Various Matrix Elements on the Efficiency of the Fire-Assay Procedures Using Nickel Sulfide as the Collector. National Institute of Metallurgy Report 1705, Johannesburg.

Ross, G. and R.A. Stephenson, 1989. Crystalline Basement: The Foundations of Western Canada Sedimentary Basin. *In:* Ricketts, B.D. (Ed.), Western Canada Sedimentary Basin; A Case History, pp. 33-45.

Saigal, G. C., K. Bjorlykke, S. Larter, 1992. The Effects of Oil Emplacement on Diagenetic Processes - Examples from the Fulmar Reservoir Sandstones, Central North Sea. AAPG Bull. No. 76, pp. 1024-1033.

Sherwin, D.F., 1962. Lower Elk Point Section in East-Central Alberta. Journal of the Alberta Society of Petroleum Geologists, vol. 10, pp. 185-191.

St John, A.M. and M.L. Cummings, 1992. Silica sinter deposits and recent geysering activity at Mickey Hot Springs, Alvord Valley, Harney County, Oregon. GSA Abstracts with Programs, vol. 24, no. 5, p. 82.

Stein, C.L. and R.J. Kirkpatrick, 1976. Experimental Porcelanite Recrystallization Kinetics: A Nucleation and Growth Model. Journal of Sedimentary Petrology, vol. 46, pp. 430-435.

Stelck, C.R., 1975. Basement Control of Cretaceous Sand Sequences in Western Canada. *In:* W.G.E. Caldwell (Ed.), Cretaceous System of the Western Interior of North America, Geological Association of Canada Special Paper 13, pp. 427-440.

Strahler, A.N. and A.H. Strahler, 1987. Modern Physical Geography, 3rd Ed. John Wiley & Sons.

Surdam, R.C. and L.J. Crossey, 1987. Integrated Diagenetic Modeling: A Process-Oriented Approach for Clastic Systems. American. Review of Earth and Planetary Science, vol. 15, pp.141-170.

Summerfield, M.A., 1983a. Silcrete as a Palaeoclimatic Indicator: Evidence From Southern Africa. Palaeogeography, Palaeoclimatology, and Palaeoecology., vol. 41, pp. 65-79.

Summerfield, M.A., 1983b. Petrography and diagenesis of silcrete from the Kalahari Basin and Cape coastal zone, Southern Africa. Journal of Sedimentary Petrology, vol. 53, no. 3, pp. 895-909.

Truesdell, A.H. and R.O. Fournier, 1975. Calculation of deep reservoir temperatures from chemistry of boiling hot springs of mixed origin. U.N. Symp. Dev. Use Geotherm. Resour., Abstr.. 2,

Truesdell, A.H. and R.O. Fournier, 1977. Procedure for estimating the temperature of hot-water component in a mixed water by using a plot of dissolved silica versus enthalpy. Journal of Research at the U.S. Geological Survey, vol. 5, no. 1, pp. 49-52.

Tsang, B.W.B., 1996. Unpublished data.

Tugarinov, I.A., I.G. Ganeyev, and I.L. Khodakovskiy, 1975. Thermodynamic properties of macedonite (α-$PbTiO_3$) and the conditions of its formation in hydrothermal veins. Geochemistry International, vol. 12, no. 4, pp. 47-53.

Urrutia, M.M. and T.J. Beveridge, 1994. Formation of Fine-Grained Metal and Silicate Precipitates on a Bacterial Surface (*Bacillus subtilis*). Chemical Geology, vol. 116, pp. 261-280.

White, D.E., W.W. Brannock, and K.J. Murata, 1956. Silica in Hot-Spring Waters. Geochimica et Cosmochimica Acta, vol. 10, pp. 27-59.

Wolery, T.J., 1986. EQ3/6; status and future development. *In:* Jackson, K.J. and W.L. Bourcier (Eds.), Proceedings of the workshop on geochemical modeling, pp. 10-19.

Wu, S., Y-H Zhao, X. Feng and A Wittmeier, 1996. Application of Inductively Coupled Plasma Mass Spectrometry for Total Metal Determination in Silicon-Containing Solid Samples Using the Microwave-Assisted Nitric Acid-Hydrofluoric Acid-Hydrogen Peroxide-Boric Acid Digestion System. Journal of Analytical Atomic Spectrometry, vol. 11, pp. 287-296.

Zhang, J.W. and G.H. Nancollas, 1990. Mechanisms of growth and dissolution of sparingly soluble salts. *In:* Hochella, M.F. Jr. and A.F. White (Eds.), Mineral-water interface geochemistry. Reviews in Mineralogy, vol. 23, pp. 365-396.

Appendix 1. Silica activity as a function of pH

The equilibrium coefficients are needed to calculate the solubility of silica using equation 10 introduced in Chapter 4. Equilibrium coefficients for various silica polymorphs were taken from the SOLMINEQ88 database (Kharakha et al., 1988) and are tabulated in Tables A1 to A5.

Table A1.1. Equilibrium coefficients for quartz taken from the SOLMINEQ88 database.

temp (°C)	0	25	50	75	100
K(SiO2)	5.75E-05	1.71E-04	2.34E-04	4.47E-04	7.94E-04
K(H4SiO4)	6.31E-11	1.48E-10	3.24E-10	5.50E-10	8.13E-10
K(H3SiO4-)	6.31E-13	2.00E-12	5.01E-12	7.94E-12	1.00E-11

Table A1.2. Equilibrium coefficients for amorphous silica taken from the SOLMINEQ88 database

temp (°C)	0	25	50	75	100
K(SiO2)	1.32E-03	2.00E-03	3.02E-03	4.27E-03	5.89E-03
K(H4SiO4)	6.31E-11	1.48E-10	3.24E-10	5.50E-10	8.13E-10
K(H3SiO4-)	6.31E-13	2.00E-12	5.01E-12	7.94E-12	1.00E-11

Table A1.3. Equilibrium coefficients for cristobalite-a taken from the SOLMINEQ88 database

temp (°C)	0	25	50	75	100
K(SiO2)	1.58E-04	2.88E-04	5.37E-04	9.77E-04	1.58E-03
K(H4SiO4)	6.31E-11	1.48E-10	3.24E-10	5.50E-10	8.13E-10
K(H3SiO4-)	6.31E-13	2.00E-12	5.01E-12	7.94E-12	1.00E-11

Table A1.4. Equilibrium coefficients for chalcedony taken from the SOLMINEQ88 database

Temperature (°C)	0	25	50	75	100
K(SiO2)	6.17E-05	1.86E-04	4.17E-04	7.94E-04	1.32E-03
K(H4SiO4)	6.31E-11	1.48E-10	3.24E-10	5.50E-10	8.13E-10
K(H3SiO4-)	6.31E-13	2.00E-12	5.01E-12	7.94E-12	1.00E-11

Table A1.5. Equilibrium coefficients for cristobalite-b taken from the SOLMINEQ88 database

Temperature (°C)	0	25	50	75	100
K(SiO2)	7.14E-04	1.15E-03	1.74E-03	2.57E-03	2.88E-03
K(H4SiO4)	6.31E-11	1.48E-10	3.24E-10	5.50E-10	8.13E-10
K(H3SiO4-)	6.31E-13	2.00E-12	5.01E-12	7.94E-12	1.00E-11

Silica reacted with water forms silicic acid. The speciation of silicic acid must be included to fully characterize the dissolution of silica. By combining the mass action equations of these reactions and the mass balance of silica considering only these Si-bearing species, an expression for the solubility of silica is achieved (Equation 10, Chapter 4). Silica solubility for various polymorphs at various temperatures and pH are tabulated in Tables 1.A6 to A1.10.

Table A1.6. Calculated silica molarity from dissolved quartz

pH	m(SiO2), 0 C	m(SiO2), 25 C	M(SiO2), 50 C	m(SiO2), 75 C	m(SiO2), 100 C
1.00	5.75E-05	1.71E-04	2.34E-04	4.47E-04	7.94E-04
2.00	5.75E-05	1.71E-04	2.34E-04	4.47E-04	7.94E-04
3.00	5.75E-05	1.71E-04	2.34E-04	4.47E-04	7.94E-04
4.00	5.75E-05	1.71E-04	2.34E-04	4.47E-04	7.94E-04
5.00	5.75E-05	1.71E-04	2.34E-04	4.47E-04	7.94E-04
6.00	5.75E-05	1.71E-04	2.34E-04	4.47E-04	7.95E-04
7.00	5.75E-05	1.71E-04	2.35E-04	4.49E-04	8.00E-04
8.00	5.79E-05	1.74E-04	2.42E-04	4.72E-04	8.59E-04
9.00	6.11E-05	1.96E-04	3.10E-04	6.95E-04	1.45E-03
10.00	9.40E-05	4.29E-04	1.03E-03	3.10E-03	7.89E-03
11.00	4.43E-04	3.21E-03	1.16E-02	4.46E-02	1.30E-01
12.00	5.98E-03	7.61E-02	4.56E-01	2.20E+00	7.10E+00
13.00	2.65E-01	5.31E+00	3.87E+01	1.98E+02	6.52E+02
14.00	2.33E+01	5.09E+02	3.81E+03	1.95E+04	6.46E+04

Table A1.7. Calculated silica molarity from dissolved amorphous silica

pH	m(SiO2), 0 C	m(SiO2), 25 C	m(SiO2), 50 C	m(SiO2), 75 C	m(SiO2), 100 C
1.00	1.32E-03	2.00E-03	3.02E-03	4.27E-03	5.89E-03
2.00	1.32E-03	2.00E-03	3.02E-03	4.27E-03	5.89E-03
3.00	1.32E-03	2.00E-03	3.02E-03	4.27E-03	5.89E-03
4.00	1.32E-03	2.00E-03	3.02E-03	4.27E-03	5.89E-03
5.00	1.32E-03	2.00E-03	3.02E-03	4.27E-03	5.89E-03
6.00	1.32E-03	2.00E-03	3.02E-03	4.27E-03	5.89E-03
7.00	1.32E-03	2.00E-03	3.03E-03	4.29E-03	5.94E-03
8.00	1.33E-03	2.02E-03	3.12E-03	4.50E-03	6.37E-03
9.00	1.40E-03	2.29E-03	4.00E-03	6.63E-03	1.07E-02
10.00	2.16E-03	5.01E-03	1.33E-02	2.96E-02	5.85E-02
11.00	1.02E-02	3.74E-02	1.50E-01	4.25E-01	9.63E-01
12.00	1.37E-01	8.88E-01	5.88E+00	2.10E+01	5.27E+01
13.00	6.09E+00	6.20E+01	5.00E+02	1.89E+03	4.83E+03
14.00	5.34E+02	5.93E+03	4.91E+04	1.87E+05	4.79E+05

Table A1.8. Calculated silica molarity from dissolved cristobalite-a

pH	m(SiO2), 0 C	m(SiO2), 25 C	m(SiO2), 50 C	m(SiO2), 75 C	m(SiO2), 100 C
1.00	1.58E-04	2.88E-04	5.37E-04	9.77E-04	1.58E-03
2.00	1.58E-04	2.88E-04	5.37E-04	9.77E-04	1.58E-03
3.00	1.58E-04	2.88E-04	5.37E-04	9.77E-04	1.58E-03
4.00	1.58E-04	2.88E-04	5.37E-04	9.77E-04	1.58E-03
5.00	1.58E-04	2.88E-04	5.37E-04	9.77E-04	1.58E-03
6.00	1.58E-04	2.88E-04	5.37E-04	9.78E-04	1.58E-03
7.00	1.58E-04	2.88E-04	5.39E-04	9.82E-04	1.59E-03
8.00	1.59E-04	2.92E-04	5.54E-04	1.03E-03	1.71E-03
9.00	1.68E-04	3.31E-04	7.12E-04	1.52E-03	2.88E-03
10.00	2.58E-04	7.23E-04	2.36E-03	6.78E-03	1.57E-02
11.00	1.22E-03	5.40E-03	2.67E-02	9.74E-02	2.58E-01
12.00	1.64E-02	1.28E-01	1.05E+00	4.80E+00	1.41E+01
13.00	7.29E-01	8.95E+00	8.89E+01	4.32E+02	1.30E+03
14.00	6.39E+01	8.57E+02	8.73E+03	4.27E+04	1.29E+05

Table A1.9. Calculated silica molarity from dissolved chalcedony

pH	m(SiO2), 0 C	m(SiO2), 25 C	m(SiO2), 50 C	m(SiO2), 75 C	m(SiO2), 100 C
1.00	6.17E-05	1.86E-04	4.17E-04	7.94E-04	1.32E-03
2.00	6.17E-05	1.86E-04	4.17E-04	7.94E-04	1.32E-03
3.00	6.17E-05	1.86E-04	4.17E-04	7.94E-04	1.32E-03
4.00	6.17E-05	1.86E-04	4.17E-04	7.94E-04	1.32E-03
5.00	6.17E-05	1.86E-04	4.17E-04	7.94E-04	1.32E-03
6.00	6.17E-05	1.86E-04	4.17E-04	7.94E-04	1.32E-03
7.00	6.17E-05	1.86E-04	4.18E-04	7.98E-04	1.33E-03
8.00	6.21E-05	1.89E-04	4.31E-04	8.38E-04	1.43E-03
9.00	6.56E-05	2.14E-04	5.53E-04	1.23E-03	2.40E-03
10.00	1.01E-04	4.67E-04	1.84E-03	5.51E-03	1.31E-02
11.00	4.76E-04	3.49E-03	2.07E-02	7.91E-02	2.16E-01
12.00	6.41E-03	8.28E-02	8.12E-01	3.90E+00	1.18E+01
13.00	2.85E-01	5.78E+00	6.90E+01	3.51E+02	1.08E+03
14.00	2.50E+01	5.53E+02	6.78E+03	3.47E+04	1.07E+05

Table A1.10. Calculated silica molarity from dissolved cristobalite-b

pH	m(SiO2), 0 C	m(SiO2), 25 C	m(SiO2), 50 C	m(SiO2), 75 C	m(SiO2), 100 C
1.00	7.14E-04	1.15E-03	1.74E-03	2.57E-03	2.88E-03
2.00	7.14E-04	1.15E-03	1.74E-03	2.57E-03	2.88E-03
3.00	7.14E-04	1.15E-03	1.74E-03	2.57E-03	2.88E-03
4.00	7.14E-04	1.15E-03	1.74E-03	2.57E-03	2.88E-03
5.00	7.14E-04	1.15E-03	1.74E-03	2.57E-03	2.88E-03
6.00	7.14E-04	1.15E-03	1.74E-03	2.57E-03	2.88E-03
7.00	7.14E-04	1.15E-03	1.75E-03	2.58E-03	2.90E-03
8.00	7.19E-04	1.17E-03	1.80E-03	2.71E-03	3.11E-03
9.00	7.59E-04	1.32E-03	2.31E-03	3.99E-03	5.24E-03
10.00	1.17E-03	2.89E-03	7.66E-03	1.78E-02	2.86E-02
11.00	5.50E-03	2.16E-02	8.64E-02	2.56E-01	4.71E-01
12.00	7.42E-02	5.12E-01	3.39E+00	1.26E+01	2.58E+01
13.00	3.29E+00	3.57E+01	2.88E+02	1.14E+03	2.36E+03
14.00	2.89E+02	3.42E+03	2.83E+04	1.12E+05	2.34E+05

Tables A1.6 to A1.10 calculate the silica solubility assuming that the activity coefficient of H^+ is unity. Activity coefficients used in the calculations in Chapter 5 where activity is considered non-unity are tabulated in Table A1.11. These values were generated from SOLMINEQ88 (Kharaka et al, 1988).

Table A1.11. Activity coefficients generated from SOLMINEQ88 (Kharaka et al., 1988) for saline fluids

$m(Na^-)$	$\gamma(H_-)$
1	0.8145
2	0.8715
3	0.9322
4	1.0042
5	1.0832
6	1.1686

Appendix 2. Method used to calculate H_2S solubility

Barta and Bradley (1985) calculated the partitioning of H2S between gas and water of varying salinities and at various temperatures and pressures. They solved the partial derivative of the Gibbs free energy equation by assuming that the gas in solution is at equilibrium with the vapor phase and eliminate the terms that explicitly express molality of the non-electrolyte H2S dependence. By doing so, the equation expressing the Henry's law ratio, k_H, becomes a solvable quadratic equation. Values of ln k_H from Equation 11 (Chapter 5) are calculated using the values calculated for λ', Δ and X for various salinities. These values are tabulated in Table A2.1.

Table A2.1. Evaluation of the Henry's Law constant at 298K

m(Na+)	*ln* k_H	k_H
0.00	2.31	10.07
1.00	2.55	12.84
2.00	2.74	15.56
3.00	2.87	17.67
4.00	2.93	18.64
5.00	2.90	18.23
6.00	2.81	16.53

Gas solubility in water, m_K, can be calculated between 25-400°C, 1-30 atm, and 0-6.2 m_{NaCl} for H_2S (Drummond, 1981). This is done using the relation:

$$k_H = f/m_K \qquad \text{(18, Chapter 5)}$$

where the gas fugacity, f, can be expressed by the equation:

$$f = P_K \Phi_{T,P}. \qquad \text{(19, Chapter 5).}$$

Nordstrom and Munoz (1985) show a graph determining the fugacity coefficient of pure gases based on the principle of corresponding states (their Figure 5.9). To determine the fugacity coefficient Φ using their figure, it is necessary to calculate the reduced pressure P_r and reduced temperature T_r for H2S. Assuming that temperature T is at 298K and given that the critical temperature T_c for H_2S is 373.2K (Nordstrom and Munoz, 1985), the reduced temperature is calculated using this equation:

$$T_r = T/T_c = 0.80 \qquad (1).$$

Similarly, the reduced pressure P_r can be calculated using this equation:

$$P_r = P/P_c \qquad (2)$$

given that the critical pressure of H_2S is 89.30 bar. The reduced pressure for H_2S at various pressures is tabulated in Table A2.2. With these values, the fugacity coefficient Φ at $T_r = 0.80$ for H_2S can be estimated using Figure 5-9 of Nordstrom and Munoz (1985).

It is now possible to calculate m_{H2S} using Equation 14. These values have been tabulated in Table A2.3.

Table A2.2. Reduced pressure P_r, fugacity coefficient Φ, and fugacity f for H_2S at various pressures at 298K

P (bar)	Pr	Φ (H_2S)	f (H_2S)
0.00	0.00	1.00	0.00
1.00	0.01	0.99	0.99
2.00	0.02	0.99	1.98
3.00	0.03	0.98	2.94
4.00	0.04	0.98	3.92
5.00	0.06	0.97	4.85
6.00	0.07	0.95	5.70
7.00	0.08	0.95	6.65
8.00	0.09	0.94	7.52
9.00	0.10	0.94	8.46
10.00	0.11	0.93	9.30
11.00	0.12	0.92	10.12
12.00	0.13	0.91	10.92
13.00	0.15	0.90	11.70
14.00	0.16	0.89	12.46
15.00	0.17	0.88	13.20
16.00	0.18	0.87	13.92
17.00	0.19	0.86	14.62
18.00	0.20	0.85	15.30
19.00	0.21	0.84	15.96
20.00	0.22	0.84	16.80

Table A2.3a. Calculation of H_2S gas solubility, m_{H2S} using Equation (14)

P(H2S), bar	m(H_2S), m(Na+)=0	m(H_2S), m(Na+)=1	m(H_2S), m(Na+)=2	m(H_2S), m(Na+)=3	m(H_2S), m(Na+)=4	m(H_2S), m(Na+)=5	m(H_2S), m(Na+)=6
0.00	0.00	0.00	0.00	0.00	0.00	0.00	0.00
1.00	0.10	0.08	0.06	0.06	0.05	0.05	0.06
2.00	0.20	0.15	0.13	0.11	0.11	0.11	0.12
3.00	0.29	0.23	0.19	0.17	0.16	0.16	0.18
4.00	0.39	0.31	0.25	0.22	0.21	0.22	0.24
5.00	0.48	0.38	0.31	0.27	0.26	0.27	0.29
6.00	0.57	0.44	0.37	0.32	0.31	0.31	0.34
7.00	0.66	0.52	0.43	0.38	0.36	0.36	0.40
8.00	0.75	0.59	0.48	0.43	0.40	0.41	0.45
9.00	0.84	0.66	0.54	0.48	0.45	0.46	0.51
10.00	0.92	0.72	0.60	0.53	0.50	0.51	0.56
11.00	1.00	0.79	0.65	0.57	0.54	0.56	0.61
12.00	1.08	0.85	0.70	0.62	0.59	0.60	0.66
13.00	1.16	0.91	0.75	0.66	0.63	0.64	0.71
14.00	1.24	0.97	0.80	0.71	0.67	0.68	0.75
15.00	1.31	1.03	0.85	0.75	0.71	0.72	0.80
16.00	1.38	1.08	0.89	0.79	0.75	0.76	0.84
17.00	1.45	1.14	0.94	0.83	0.78	0.80	0.88
18.00	1.52	1.19	0.98	0.87	0.82	0.84	0.93
19.00	1.58	1.24	1.03	0.90	0.86	0.88	0.97
20.00	1.67	1.31	1.08	0.95	0.90	0.92	1.02

Table A2.3b. Calculation of H_2S gas solubility, ppm(H2S) using Equation (14)

$P_{(H2S)}$, bar	Ppm(H_2S), m(Na+=0)	ppm(H_2S), m(Na+)=1	ppm(H_2S), m(Na+)=2	ppm(H_2S), m(Na+)=3	ppm(H_2S), m(Na+)=4	ppm(H_2S), m(Na+)=5	ppm(H_2S), m(Na+)=6
0.00	0	0	0	0	0	0	0
1.00	3349	2627	2169	1910	1810	1851	2041
2.00	6699	5254	4337	3820	3619	3702	4082
3.00	9947	7802	6440	5672	5374	5497	6061
4.00	13262	10402	8587	7562	7166	7329	8081
5.00	16409	12870	10624	9357	8866	9068	9999
6.00	19285	15125	12486	10996	10420	10658	11751
7.00	22499	17646	14566	12829	12156	12434	13710
8.00	25442	19955	16472	14508	13747	14061	15503
9.00	28622	22449	18531	16321	15465	15818	17441
10.00	31464	24678	20371	17941	17000	17389	19173
11.00	34239	26854	22167	19523	18499	18922	20863
12.00	36945	28977	23920	21067	19962	20418	22512
13.00	39584	31047	25628	22572	21388	21876	24121
14.00	42155	33064	27293	24038	22777	23297	25687
15.00	44659	35027	28914	25465	24130	24681	27213
16.00	47095	36938	30491	26854	25446	26027	28697
17.00	49463	38795	32024	28205	26725	27336	30140
18.00	51764	40600	33514	29517	27968	28607	31542
19.00	53997	42351	34960	30790	29175	29841	32903
20.00	56839	44580	36800	32410	30710	31412	34635

Appendix 3, BRS sample suite

Sample	Station # (Figure 2.3)	Location (Easting)	Location (Northing)	Field descriptions
AU94-007	AUH96-002	464251	6334759	Beaver River Sandstone, possibly float
AU94-017	AUH96-003	462544	630998	sample from east end of borrow pit approximately in the center, 15 m east of the water line in the pit. BRSS is med. grey, m-c grained quartz sandstone with finely XLN silica cement. There appears to be very small pyrite grains in the matrix.
AU94-022	AUH96-004	464632	6338791	dark grey, siliceous, and possibly partly bitumen saturated quartz sandstone. Contains some porosity (1-2%) but is extremely hard nevertheless. Slight mottling of 1 mm greyish-brown patches and probably relict bitumen staining.
AU94-023	AUH96-005	464657	6339115	Mottled light greyish-red to dark grey, siliceous quartz cemented quartz sandstone. contains possible relict bitumen and appears to contain finely disseminated metallic mineralization.
AU94-024	AUH96-006	46425	6338860	BRSS sampled in the middle of the large roche moutonnee. Dark grey to black where oil-stained
AU94-025	AUH96-007	464610	6338931	Mottled to laminated dark grey to tan, siliceous quartz sand. identical location to R-45 (Tintina location WK-31 approximate). o/c of BRSS extends to road on map which travels at 045 from main road from main road crossing on Muskeg R.
AU94-030	AUH96-008	463624	6336650	BRSS - silica cemented m-c grained quartz sandstone, white-grey, tan to black where apparently coated by oil. At Tintina o/c WK-2; location of sample "CQS".
AU94-031	AUH96-009	463611	6336620	Black, tan and grey mottled BRSS o/c consists of variably massive, grey, f. gr. quartz ss and poorly sorted mottled grey and black m-c gr. ss.
AU94-037	AUH96-010	464692	6338263	BRSS- silica cemented quartz sandstone at site labelled "CR414516" and WK-34?
AU94-046	AUH96-011	463250	6342401	Yellow-grey BRSS (coarse grained McM.) overlooking Athabasca R. on east side approximately 12 m above river. Beds here dip to south, but change to N dip before 047. No thin section.
AU94-062		474750	6305650	White, partly altered Devonian lst sampled approx 25 cm below o/c of dark grey-brown, v. f. gr., Fe stained (purple and orange) BRSS. The unconf. is marked by approx. 20 cm of Fe-stained and highly altered lst (with clayey consistency). No thin section.
AU94-078	AUH96-012	461751	6337101	Outcrop of massive to poorly bedded grey to maroon to intenxe orange-maroon Fe stained, coarse grained quartz carbonate clast ss in a goethite matrix. Probable BRSS 142 degrees to S. tip of small island S. of Ft. MacK. No thin section.

Appendix 3, BRS sample suite

Sample	Station # (Figure 2.3)	Location (Easting)	Location (Northing)	Field descriptions
AU94-079		462050	6338100	Outcrop of red-stained nodular, rubbly to massive bioclastic limestone at F. MacKay townsite on river. Outcrop dips 20-30 degrees to the S and is overlain by BRSS (in o/c). Contact not observed. The red coloration is due to downslope movement of red earth. Sample is a composite of carbonate lithologies including massive and rubbly biocastic lst. No thin section.
AU95-002	AUH96-013	462369	6330998	BRSS collected from o/c on NW end of borrow pit. Grey, f.-m.gr., mod. sorted quartz sandstone. Hard, well indurated with quartz cement. Dark grey with some light grey alteration on surface
AU95-003	AUH96-014	464281	6333526	Med - dk. grey, m-c. gr., quartgz cemented, quartz +kf(?) sandstone. Weathers to tan-grey and o/c has approx a 5 mm rind. Fresh surfaces are grey to dark grey with variable bitumen content. O/c appears to be "heaved" with mound convered by "pavement" of round weathering BRSS. ** may contain trace disseminated metallic mineralization. STA 95-003
AU95-009	AUH96-015	464616	6336215	BRSS - at top of river bank above bluff of L. McM approx 6 m. high. BRSS is approximately 35 cm thick and is a resistant cap.
AU95-010		464616	6336215	Check to see if sample of McMurray Fm underlying the BRSS resistant cap.
AU95-011	AUH96-016	464616	6336215	Sample of BRSS taken at top of bank edge approx 12 m south of sample 009. Sample is quartz cemented, weathered or partly altered parts contain some bitumen and ferruginous Forric oxyhydroxide minerals.
AU95-012	AUH96-017	464615	6336526	Black (bituminous) stained BRSS at N end of long (250 m +) o/c ridge of BRSS. BRSS occurs on knolls on top of LMcM Fm ss. L McM underlies small ridges. Resistant BRSS caps some, but not all. Very close to site of RR-16, approx 15m S of AU95-018).
AU95-013	AUH96-018	464583	6336256	"The obelisk". 70 cm thick o/c of BRSS. Also black stained, poorly sorted m-c. gr. partly silica and bitumen? cemented ss similar to AU95-012. Close to RR-15, which is 20 m S.
AU95-014	AUH96-019	464468	6335906	BRSS grey and black silica/bitumen(?) cemented ss. Very similar to other BRSS samples collected in this area. Knoll capped by BRSS, 60 cm - 2 m thick.
AU95-015	AUH96-020	464723	6337585	BRSS o/c SW of cabins on west bank of Muskeg R. O/C appears to be an extension of the o/c seen yesterday - quad tracks leads from cabins area. "Rounded" knolls of lower McM are capped by resistant BRSS, 50 cm thick.

Appendix 3, BRS sample suite

Sample	Station # (Figure 2.3)	Location (Easting)	Location (Northing)	Field descriptions
AU95-016	AUH96-022	464552	6337338	At bend in Muskeg R., where LMcM (oil stained) is overlain by resistant BRSS in a lichen-moss covered meadow. 60 cm thick.
AU95-017	AUH96-021	463529	6336748	
AU95-019	AUH96-023	463961	6336861	BRSS - typical, some dark staining on fractures (oil?). O/C - large lichen covered meadow, rock floored.
AU95-020	AUH96-024	464239	6336901	BRSS o/c thickness 80 cm (minimum). Mottled variegated black, grey, tan laminated BRSS. Taken 30 m S of RR 21.
AU95-021	AUH96-025	464227	6336452	Near site of sample RR-17. BRSS along S edge of LMcM sand "bank". Thickness here approx 50 cm min.
AU95-023	AUH96-026	464454	6338556	BRSS on small step on powerline. Thickness of BRSS approx 83 cm. Grey weathering BRSS. some dark banding on freshly broken surfaces, but in generalquite fresh looking (no ?bitumen staining).
AU95-024	AUH96-028	464638	6338421	BRSS o/c (with bear den) in middle of swamp! (island of BRSS) 90 cm thickness.
AU95-025	AUH96-027	464952	6339859	BRSS in open o/c lying on c. gr. LMcM. BRSS sits up approx 1-2 m above elevation of forest and is clearly lying on top of the sands in this area signifying that it is the hightest unit. Therefore all other sands are probably LMcM(assuming that BRSS is top of LMcM (which may not be correct. 85 cm thick)
AU95-026	AUH96-029	464666	6340251	Small BRSS o/c at top of small knoll. Thickness unknown, but >30 cm.
AU96-001	AUH96-030	464116	6332821	Grab sample of coarse quartz grains eroded out of lower member of McM. Compare geochemically w/ AU96-002 and f. gr. qtz sand from upper member. Sample taken for determining if BRSS is detrital, and if so, what is the nature of the coarse quartz grains?
AU96-002	AUH96-031	464116	6332821	Massively siliceous, very coarse to cobble sized quartz clasts were collected. Collection of qtz pebbles-(fragmented) boulder including possible vein qtz(??), silicified wood, tormaline bearing megaXLN qtz (shield origin?).
AU96-009	AUH96-032	465679	6340064	BRSS, probable outcrop, but not 100% sure. BRS exposed in tipped tree, tree roots in tar sand with grey, bituminous (along fractures), v. hard, qtz cemented BRS.
AU96-010	AUH96-033	464261	6340337	Siderite cemented lower McM. Has also been termed BRSS by some. Near to area of abundant true BRSS (qtz cemented, qtz ss) and previous years identified location of BRSS. Include this sample for textures and bulk rock geochem.

Appendix 3, BRS sample suite

Sample	Station # (Figure 2.3)	Location (Easting)	Location (Northing)	Field descriptions
AU96-011	AUH96-034	464693	6340209	BRSS in float boulder on powerline. BRSS probably exists at depth underneath this location and has been brought to surface by power/pipeline construction.
AU96-012	AUH96-038	464406	6339996	mottled grey to dark grey (bitumen). Sample is from large, near o/c which is approx. 90 cm thick. Could be transported but likely is in place - several other BRSS boulders were found at this location.
AU96-013	AUH96-039	464119	6340504	Red-brown siderite(?) cemented sandstone (BRSS equiv.)
AU96-014	AUH96-035	464245	6340707	BRSS in float in sand ridge
AU96-015	AUH96-036	464719	6340440	Probable BRSS in o/c. Grey, f. gr. qtz ss with (micro)qtz cement. Location has several qtz cemented ss boulders in one location. Most are moss and lichen covered and are probably in place (several in this location). Thickness is difficult to estimate, but probably >30 cm.
AU96-016	AUH96-040	464632	6340027	(Siderite) Red-cemented BRSS from probable o/c.
AU96-017	AUH96-041	461467	6347486	Composite grab sample of Fe-stained sideritic lower McM. Sideritic stain is secondary; unaltered sideritic material is light greenish brown in color.also present are Fe-coated qtz cemented BRSS. Sample taken on E side of Bitumount Road.
AU96-043	AUH96-037	464632	6338791	Sandy soil collected at the AU94-022 o/c area. Sample was taken approximately 30 cm below the surface as a potential constraint of the soil underlaying BRSS. Roy Eccles suggests that the BRSS here is at surface due to frost heave.

Appendix 4

Raw XRD data for selected suite of pulped BRS samples. Tabulated values include angle, d spacings, peak width, peak intensity, background intensity, relative peak intensity and actual intensity. Instrumental parameters are also reported.

[illegible] program base: TBAB 14-Nov-1995 10:34

[illegible] MINERALOGY LABORATORY [illegible] [illegible]

Program created at: 14-Nov-1995 10:21:11.
Last update: 14-Nov-1995 10:21:00

Default base for raw data files: TBAB

Pos	Program name	Program type	Sample identification	Data file name
1	[illegible]	[illegible]	[illegible]	TBAB_1
2	[illegible]	[illegible]	[illegible]	TBAB_2
3	[illegible]	[illegible]	[illegible]	TBAB_3
4	[illegible]	[illegible]	[illegible]	TBAB_4
5	[illegible]	[illegible]	[illegible]	TBAB_5
6	[illegible]	[illegible]	[illegible]	TBAB_6
7	[illegible]	[illegible]	[illegible]	TBAB_7
8	[illegible]	[illegible]	[illegible]	TBAB_8
9	[illegible]	[illegible]	[illegible]	TBAB_9
10	[illegible]	[illegible]	[illegible]	TBAB_10
11	[illegible]	[illegible]	[illegible]	TBAB_11
12	[illegible]	[illegible]	[illegible]	TBAB_12
13	[illegible]	[illegible]	[illegible]	TBAB_13
14	[illegible]	[illegible]	[illegible]	TBAB_14
15	[illegible]	[illegible]	[illegible]	TBAB_15
16	[illegible]	[illegible]	[illegible]	TBAB_16
17	[illegible]	[illegible]	[illegible]	TBAB_17
18	[illegible]	[illegible]	[illegible]	TBAB_18
19	[illegible]	[illegible]	[illegible]	TBAB_19
20	[illegible]	[illegible]	[illegible]	TBAB_20
21	[illegible]	[illegible]	[illegible]	TBAB_21
22	[illegible]	[illegible]	[illegible]	TBAB_22

File: TSA901.DI 16-Nov-1995 10:22

CLAY MINERALOGY LABORATORY PW1700 JENNY WONG

Sample identification: SU95-00C
Data measured at: 14-Nov-1995 10:07:00

Diffractometer type: PW1710 BASED
Tube anode: Co
Generator tension [kV]: 40
Generator current [mA]: 30
Wavelength Alpha1 [A]: 1.78896
Wavelength Alpha2 [A]: 1.79285
Intensity ratio (alpha2/alpha1): 0.500
Divergence slit: Automatic
Irradiated length [mm]: 12
Receiving slit: 0.2
Monochromator used: YES
Start angle [°2Th]: 4.000
End angle [°2Th]: 64.020
Step size [°2Th]: 0.020
Maximum intensity: 14689.44
Time per step [s]: 1.000
Type of scan: CONTINUOUS
Minimum peak tip width: 0.000
Maximum peak tip width: 0.000
Peak base width: 0.000
Minimum significance: 0.75
Number of peaks: 17

Angle [°2Th]	d-value 1 [A]	d-value 2 [A]	Peak width [°2Th]	Peak int [counts]	Back. int [counts]	Rel. int [%]	Signif.
13.730	6.4467	6.4563	0.160	199	14	1.4	0.91
14.195	6.2367	6.2460	0.140	2591	13	17.6	29.65
19.050	4.6568	4.6638	0.080	12	13	0.1	1.09
19.485	4.5527	4.5595	0.120	22	14	0.2	1.65
21.045	4.2184	4.2247	0.140	14689	15	100.0	65.33
42.715	2.1161	2.1192	0.100	1122	13	7.6	7.74
46.165	1.9648	1.9677	0.080	900	14	6.1	4.24
46.295	1.9595	1.9624	0.040	365	14	2.5	1.20
47.150	1.9260	1.9289	0.080	511	14	3.5	2.70
47.280	1.9208	1.9237	0.060	237	14	1.6	1.05
49.715	1.8320	1.8348	0.080	1011	14	6.9	5.92
49.845	1.8274	1.8302	0.060	543	14	3.7	1.44
53.715	1.7049	1.7075	0.080	497	14	3.4	2.91
53.855	1.7006	1.7032	0.060	240	14	1.6	2.50
58.940	1.5652	1.5676	0.080	1764	12	12.0	6.87
59.095	1.5614	1.5638	0.060	818	12	5.6	1.49
59.530	1.5507	1.5531	0.060	42	12	0.3	0.86

File: 73497.01 16-Nov-1995 10:12

CLAY MINERALOGY LABORATORY PW1700 JENNY WANG

Sample identification: 4078-014
Data measured at: 14-Nov-1995 15:43:00

Diffractometer type: PW1710 BASED
Tube anode: Cu
Generator tension [kV]: 40
Generator current [mA]: 30
Wavelength Alpha1 [A]: 1.78896
Wavelength Alpha2 [A]: 1.79285
Intensity ratio (alpha2/alpha1): 0.500
Divergence slit: AUTOMATIC
Irradiated length [mm]: 12
Receiving slit: 0.2
Scatter: OFF
Anti-scatter slit: 1.0

Start angle [2Th]: 4.000
End angle [2Th]: 64.000
Step size [2Th]: 0.020
Maximum intensity: 12773.00
Time per step [s]: 1.000
Type of scan: CONTINUOUS

Minimum peak tip width: 0.0
Minimum peak tip width: 0.00
Peak base width: 0.10
Minimum significance: 0.75
Offset of peaks: 0.0

Angle [2Th]	d-value [A]	d-value [A]	Peak width [2Th]	Peak int [counts]	Back. int [counts]	Rel. int [%]	Signif.
7.420	12.0022	12.0814	0.160	45	24	0.3	1.35
14.020	6.3144	6.3397	0.120	3.70	14	24.4	20.71
19.100	5.6832	5.6912	0.480	6	14	0.0	0.35
21.075	5.0392	5.0445	0.140	12773	16	100.0	62.62
42.720	2.4588	2.4612	0.100	1142	12	8.9	8.40
42.820	2.4495	2.4549	0.040	650	12	5.0	4.27
45.185	2.2806	2.2855	0.100	681	12	5.3	5.55
47.155	2.2358	2.2407	0.080	445	12	3.4	2.46
49.735	2.1271	2.1317	0.080	858	12	6.6	4.72
49.875	2.1215	2.1261	0.060	386	12	3.0	0.79
52.455	2.0240	2.0284	0.300	7	11	0.1	0.79
53.740	1.9791	1.9834	0.060	734	11	5.7	2.22
53.885	1.9742	1.9784	0.060	335	11	2.6	1.16
58.955	1.8177	1.8217	0.060	1739	13	13.4	6.90
59.115	1.8133	1.8172	0.060	841	13	6.5	1.67
59.520	1.8020	1.8060	0.060	62	12	0.5	1.60

File: TSN802.DI 16-Nov-1995 10:24

CLAY MINERALOGY LABORATORY PW1700 JENNY WONG

Sample identification: AU95-003
Data measured at: 14-Nov-1995 11:28:00

Diffractometer type: PW1710 BASED
Tube anode: Co
Generator tension [kV]: 40
Generator current [mA]: 30
wavelength #1(a) [A]: 1.7889a
wavelength #1(a) [A]: 1.79285
Intensity ratio (alpha2/alpha1) : 0.500
Divergence slit: AUTOMATIC
Irradiated length [mm]: 12
Receiving slit: 0.2
Scatter: Off
Monochromator used: YES

Start angle [deg]: 4.000
End angle [deg]: 64.020
Step size [deg]: 0.020
Maximum intensity: 1047.37
Time per step [s]: 1.000
Type of scan: CONTINUOUS

Minimum peak tip width: 0.00
Maximum peak tip width: 1.00
Peak base width: 1.00
Minimum significance: 0.75
Number of peaks: 17

Angle [deg]	d-value 1 [A]	d-value 2 [A]	Peak width [deg]	Peak int [counts]	Back. int [counts]	Rel. int [%]	Signif.
4.280	20.6960	20.7503	0.400	19	44	0.2	0.76
20.140	4.4058	4.4095	0.120	34	12	0.3	1.34
14.310	4.1407	4.2555	0.140	2642	12	21.2	58.50
28.090	3.6656	3.6703	0.120	13	12	0.1	1.14
31.070	3.3078	3.3470	0.140	12477	14	100.0	59.22
42.730	2.4555	2.4606	0.120	992	12	8.0	11.14
42.845	2.4490	2.4543	0.040	445	12	3.6	1.31
46.200	2.2797	2.2843	0.100	697	12	5.6	6.19
47.180	2.2351	2.2400	0.080	557	13	4.5	3.66
47.310	2.2294	2.2342	0.040	219	13	1.8	1.21
49.750	2.1265	2.1311	0.080	713	13	5.7	3.53
49.890	2.1209	2.1255	0.040	339	13	2.7	3.16
53.730	1.9794	1.9837	0.080	458	14	3.7	3.25
53.880	1.9743	1.9786	0.060	225	13	1.8	0.84
58.965	1.8175	1.8214	0.100	1600	12	12.8	10.95
59.115	1.8133	1.8172	0.060	812	12	6.5	1.85
59.545	1.8014	1.8053	0.160	29	12	0.2	0.79

File: TSA902.01 16-Nov-1995 10:24

CLAY MINERALOGY LABORATORY PW1710 JENNY WONG

182

Sample identification: AU95-009
Data measured at: 14-Nov-1995 12:19:00

Diffractometer type: PW1710 BASED
Tube anode: Co
Generator tension [kV]: 40
Generator current [mA]: 30
Wavelength Alpha1 [A]: 1.7889e
Wavelength Alpha2 [A]: 1.7929e
Intensity ratio (alpha2/alpha1): 0.50
Divergence slit: AUTOM-TIC
Irradiated length [mm]: 12
Receiving slit: 0.2
Scanning: CON
Monochromator used: YES

Start angle [°2th]: 4.000
End angle [°2th]: 64.020
Step size [°2th]: 0.020
Maximum intensity: 1e+05
Time per step [s]: 1.000
Type of scan: CONTINUOUS

Minimum peak tip width: 0.1
Maximum peak tip width: 1.0
Peak base width: 1.0
Minimum significance: 0.75
Number of peaks: 17

Angle [°2th]	d-value 1 [A]	d-value 2 [A]	Peak width [°2th]	Peak int [counts]	Back. int [counts]	Rel. int [%]	Signif.
24.335	4.2479	4.2531	0.120	2850	12	17.2	21.20
28.125	3.8810	3.8867	0.481	5	12	0.0	0.75
29.545	3.7638	3.7696	0.120	29	12	0.2	2.74
31.095	3.5771	3.5844	0.140	16689	14	100.0	62.87
39.500	2.6470	2.6523	0.240	4	11	0.0	0.90
42.745	2.4545	2.4578	0.100	935	12	5.7	6.39
42.865	2.4479	2.4532	0.060	392	12	2.7	1.90
46.205	2.2796	2.2846	0.080	773	12	5.3	4.15
46.335	2.2736	2.2785	0.060	357	12	2.4	1.39
47.185	2.2349	2.2398	0.080	467	13	3.2	3.28
49.770	2.1257	2.1303	0.060	1109	14	7.5	2.71
49.900	2.1205	2.1251	0.060	536	14	4.0	1.90
53.755	1.9786	1.9829	0.080	441	13	3.0	2.72
53.905	1.9735	1.9778	0.060	225	13	1.5	0.90
58.985	1.8169	1.8209	0.100	1459	12	9.9	10.05
59.135	1.8127	1.8167	0.060	745	12	5.1	1.54
59.585	1.8003	1.8042	0.080	64	12	0.4	0.96

File: TBA804.DI 14-Nov-1995 10:26

CLAY MINERALS LABORATORY PW1700 JENNY WONG

Sample identification: AU95-011
Data measured at: 14-Nov-1995 13:10:00

Diffractometer type: PW1710 BASED
Tube anode: Cu
Generator tension [kV]: 40
Generator current [mA]: 20
Wavelength Alpha1 [A]: 1.78896
Wavelength alpha2 [A]: 1.79285
Intensity ratio (alpha2/alpha1): 0.500
Divergence slit: AUTOMATIC
Irradiated length [mm]: 12
Receiving slit: 0.2
Soller: 2.3°
Monochromator used: YES

Start angle [°2θ]: 4.000
End angle [°2θ]: 64.020
Step size [°2θ]: 0.020
Maximum intensity: 144014.31
Time per step [s]: 1.000
Type of scan: CONTINUOUS

Minimum peak tip width: 0.07
Maximum peak tip width: 0.50
Peak base width: 1.00
Minimum significance: 0.75
Number of peaks: 19

Angle [°2θ]	d-value [A]	d-value [A]	Peak width [°2θ]	Peak int [counts]	Back. int [counts]	Rel. int [%]	Signif.
8.873	12.7118	12.7278	0.300	4	19	0.0	0.92
14.228	4.2429	4.2501	0.140	2540	17	17.6	27.17
18.180	3.6496	3.6560	0.220	8	12	0.1	0.95
19.485	3.5185	3.5246	0.240	12	14	0.1	1.39
21.090	3.3377	3.3449	0.140	144014	15	100.0	63.82
42.730	2.4542	2.4595	0.120	941	12	6.5	9.05
42.865	2.4479	2.4532	0.040	412	12	2.9	0.90
44.275	2.3739	2.3791	0.160	18	12	0.1	1.05
45.810	2.3367	2.3420	0.240	5	13	0.0	0.76
46.210	2.2794	2.2844	0.080	900	13	6.2	4.43
46.335	2.2736	2.2785	0.060	449	13	3.1	0.94
47.190	2.2347	2.2396	0.100	475	13	3.3	4.36
47.310	2.2294	2.2342	0.040	240	13	1.7	1.24
49.755	2.1263	2.1309	0.080	713	14	4.9	4.06
49.870	2.1209	2.1255	0.060	365	14	2.5	0.85
53.760	1.9784	1.9827	0.100	524	14	3.6	6.07
56.505	1.8696	1.8933	0.480	8	12	0.1	1.36
58.980	1.8170	1.8210	0.080	1568	13	10.9	5.46
59.135	1.8127	1.8167	0.060	784	13	5.4	1.73

File: TEA505.DI 16-Nov-1995 10:27

DLW MINERALOGY LABORATORY PW1700 JENNY ACN3

Sample identification: AL95-112
Data measured at: 14-Nov-1995 14:01:00

Diffractometer type: PW1710 BASED
Tube anode: Cu
Generator tension [kV]: 40
Generator current [mA]: 30
Wavelength Alpha1 [A]: 1.78896
Wavelength Alpha2 [A]: 1.79285
Intensity ratio (alpha2/alpha1): 0.500
Divergence slit: AUTOMATIC
Irradiated length [mm]: 12
Receiving slit: 0.2
Scatter: ???
Monochromator used: YES

Start angle [°2Th]: 4.000
End angle [°2Th]: 64.020
Step size [°2Th]: 0.020
Maximum intensity: 14901.84
Time per step [s]: 1.000
Type of scan: CONTINUOUS

Profile peak list width: .10
Maximum peak list width: 1.00
Peak base width: 0.16
Minimum significance: .75
Number of peaks: 21

Angle [°2Th]	d-value 1 [A]	d-value 2 [A]	Peak width [°2Th]	Peak int [counts]	Back. int [counts]	Rel. Int [%]	Signif.
14.330	4.2447	4.2537	0.120	2582	12	17.3	10.26
15.110	4.0802	4.0892	0.160	17	12	0.1	0.94
19.810	3.6121	3.6197	0.120	27	12	0.2	1.79
21.085	3.3882	3.3955	0.140	14933	13	100.0	68.10
21.995	3.2476	3.2527	0.120	32	14	0.2	1.06
42.745	2.4545	2.4578	0.060	1537	12	10.3	3.21
42.860	2.4482	2.4535	0.060	724	12	4.8	1.43
44.175	2.3788	2.3840	0.240	4	12	0.0	0.77
46.200	2.2799	2.2848	0.080	801	12	5.4	4.00
46.325	2.2741	2.2790	0.040	376	12	2.5	2.85
47.180	2.2351	2.2400	0.080	445	13	3.0	2.80
47.305	2.2296	2.2344	0.040	193	13	1.3	1.78
49.750	2.1265	2.1311	0.080	724	13	4.8	4.04
49.890	2.1209	2.1255	0.040	331	13	2.2	1.98
53.750	1.9787	1.9830	0.080	515	14	3.5	3.67
53.895	1.9738	1.9781	0.060	207	13	1.4	0.83
56.490	1.8901	1.8942	0.240	10	12	0.1	1.25
58.975	1.8172	1.8211	0.080	1459	12	9.8	5.68
59.125	1.8130	1.8169	0.060	734	12	4.9	1.78
59.565	1.8009	1.8047	0.100	40	12	0.3	0.97

File: TSA806.DI 16-Nov-1995 10:28

CLAY MINERALOGY LABORATORY PW1700 JENNY ANNE

Sample identification: A895-01C
Data measured at: 14-Nov-1995 14:52:00

Diffractometer type: PW1710 BASED
Tube anode: Cu
Generator tension [kV]: 40
Generator current [mA]: 30
Wavelength Alpha1 [A]: 1.78896
Wavelength Alpha2 [A]: 1.79285
Intensity ratio alpha2/alpha1: 0.500
Divergence slit: AUTOMATIC
Irradiated length [mm]: 12
Receiving slit: 0.2
Diffracted beam monochromator used: YES
Start angle [2θ]: 4.000
End angle [2θ]: 64.020
Step size [2θ]: 0.020
Maximum intensity: 14184.81
Time per step [s]: 1.000
Type of scan: CONTINUOUS
Minimum peak tip width: 0.00
Maximum peak tip width: 0.00
Peak base width: 0.00
Minimum significance: 0.75
Number of peaks: 17

Angle [°2θ]	d-value [A]	d-value [A]	Peak width [°2θ]	Peak int [counts]	Back. int [counts]	Rel. int [%]	Signif.
15.770	5.6212	5.6344	0.240	5	14	0.0	1.20
14.000	4.2447	4.2579	0.140	2830	15	20.0	31.38
13.185	3.8364	3.8484	0.120	12	14	0.1	0.89
21.190	3.3377	3.3449	0.160	14185	13	100.0	84.72
40.770	2.4590	2.4696	0.080	961	12	6.8	4.88
42.350	2.4487	2.4541	0.040	467	12	3.3	2.31
44.200	2.2799	2.2848	0.100	776	13	5.5	6.63
46.330	2.2738	2.2788	0.040	350	13	2.5	2.76
47.185	2.2349	2.2398	0.100	467	12	3.3	4.64
47.310	2.2294	2.2342	0.040	216	12	1.5	1.08
49.740	2.1269	2.1315	0.080	829	12	5.8	4.26
49.875	2.1215	2.1261	0.060	424	12	3.0	0.79
53.745	1.9789	1.9832	0.100	488	14	3.4	5.94
53.890	1.9740	1.9783	0.040	228	14	1.6	3.95
58.975	1.8172	1.8211	0.080	1429	12	10.1	6.01
59.125	1.8130	1.8169	0.080	713	12	5.0	2.85
59.545	1.8014	1.8053	0.080	135	12	0.2	0.93

Appendix 5

A select sample set was run for LA-ICP-MS analysis. These were chosen in an attempt to quantify the amount of native precious metals observed under BSE. Different blanks were used for different samples. Samples were collected in multiple runs at different spots and are reported as such. Results are blank corrected values and therefore negative values are calculated to be less than the blank value.

Appendix 5, LA-ICP-MS data

Sample	Li 7	Be 9	B 11	Na 23	Mg 26	Al 27	Si 29	S 34	K39	Ca 43	Sc 45	Ti 49
Blank, 28/8/96 1	0.07	0.34	2	1171	1	6	659	375	4	164	4	0
AU95-012 1	9.59	0.1	5	358	27	2284	468706	5628	74	3772	23	813.01
AU95-012 2	11.75	0.04	6	197	30	4821	454852	9331	49	4007	22	618.1
AU95-012 3	12.65	6.25	6	-25	17	996	462385	3925	24	2009	21	717.4
AU95-012 4	6.16	-0.01	6	425	17	1823	462743	1394	88	1702	14	728.3
AU95-012 5	10.54	0.19	58	-176	15	403	462585	3752	17	2678	17	534.8
AU95-012 6	9.88	-0.02	7	-57	15	757	462303	3989	28	2076	20	1021
Average	10.09	1.09	6	120	20	1847	460596	4670	47	2707	20	738.8
Std. Dev.	2.25	2.53	1	243	7	1615	3201	2655	29	972	3	168.5
RSD	22.24	231.62	11.49	201.8	32.59	87.4	0.7	56.85	62.38	35.89	16.78	22.8
Blank 3/9/96 1	0.05	0.36	18	368	6	4	830	556	68	871	7	1.5
AU94-017 1	15.28	0.37	190	592	626	1740	408090	1102	826	6838	34	102344.2
AU94-017 2	17.31	0.2	110	493	440	951	434758	933	665	6000	22	52062.2
Average	16.3	0.29	150	543	533	1346	421424	1017	746	6419	28	77203.2
Std. Dev.	1.43	0.12	57	70	132	558	18858	120	114	592	9	35554.7
RSD	8.8	40.97	38.89	12.87	24.74	41.45	4.47	11.77	15.31	9.23	31.52	46.05
AU94-022 1	11.88	0.26	14	202	1119	3379	388636	96212	1274	312156	22	9503.2
AU94-022 2	11.24	0.16	10	205	776	1609	414509	58260	816	21028	21	11689.1
AU94-022 3	11.33	0.18	29	325	736	1440	4205425	50975	717	18150	21	11638.3
AU94-022 4	11.52	0.18	17	193	837	1933	410708	65346	887	22408	22	10618.9
AU94-022 5	8.63	0.13	10	141	428	1004	431378	36952	500	12846	16	14116.4
AU94-022 6	11.92	0.19	18	198	665	1723	423421	41469	998	18785	21	14804
Average	11.09	0.18	16	211	760	1848	414866	58202	865	20746	21	12061.6
Std. Dev.	1.24	0.04	7	61	226	813	14721	21352	262	6104	2	2034.1
RSD	11.16	23.03	44.24	28.89	29.73	43.99	3.55	36.69	3024	29.42	10.97	16.86
AU94-007 1	8.26	0.14	18	262	434	636	437722	24144	682	13199	21	14155.5
AU94-007 2	11.28	0.18	32	364	485	861	431982	30284	855	14579	26	17033.8
AU94-007 3	11.05	0.17	35	330	517	759	430042	31556	670	14208	23	21064.2
AU94-007 4	11.78	0.12	51	378	446	783	432158	26833	1124	13288	25	218901.5
Average	10.59	0.15	34	334	470	760	432976	28204	833	13818	24	18536
Std. Dev.	1.59	0.03	14	52	37	93	3306	3363	212	682	2	3609.7
RSD	14.98	18.22	39.89	15.51	7.97	12.29	0.76	11.92	25.42	4.93	10.44	19.47

Appendix 5, LA-ICP-MS data

Sample	Li 7	Be 9	B 11	Na 23	Mg 26	Al 27	Si 29	S 34	K39	Ca 43	Sc 45	Ti 49
Blank, 3/9/96 2	0.55	0.23	8	1788	11	56	1852	1809	271	1495	8	3.5
AU94-025 1	13.42	0.09	18	209	132	2337	451758	12566	623	4365	10	6508.4
AU94-025 2	14.38	0.17	19	267	125	1432	456060	5984	875	3902	10	6351.3
AU94-025 3	17.95	0.54	34	199	201	3512	448568	10991	805	5655	13	10246.4
AU94-025 4	18.32	0.41	30	148	115	883	456765	2297	773	4169	14	8924.5
AU94-025 5	17.69	0.32	26	234	282	4052	443426	13365	1162	6482	14	12586.1
AU94-025 6	12.42	0.14	21	64	75	396	459579	4835	392	2594	9	5332.7
Average	15.7	0.28	25	187	155	2102	452693	8340	771	4528	12	8324.9
Std. Dev.	2.59	0.18	7	72	74	1465	5985	4571	257	1369	2	2769.8
RSD	16.51	63.38	26.84	38.44	47.99	69.57	1.32	54.81	33.3	30.24	18.65	33.27
AU95-019 1	14.8	0.12	25	202	130	4754	453930	1198	674	3312	8	7189.3
AU95-019 2	9.08	0.01	13	32	76	518	461393	955	346	1866	7	3336.7
AU95-019 3	15.07	0.08	15	126	198	2687	453812	2668	746	5732	12	4179.63
AU95-019 4	15.43	0.12	20	14	346	1718	446621	1334	695	17445	23	7629.3
AU95-019 5	19.88	0.12	26	155	363	3199	447908	1199	609	9089	11	9665.9
Average	14.85	0.09	20	106	223	2575	452733	1471	614	7489	12	6411.1
Std. Dev.	3.84	0.05	6	80	128	1590	5879	683	157	6202	6	2603.6
RSD	25.84	53.86	28.77	76.08	57.49	61.74	1.3	46.44	25.64	82.81	51.88	40.68

Appendix 5, LA-ICP-MS data

Sample	V 51	Cr 52	Mn 55	Fe 57	Co 59	Ni 60	Zn 64	Cu 65	Ga 69	Ge 73	As 75	Se 82
Blank, 28/8/96 1	0.17	1	0.3	2	1	1.2	0	1	0.1	0.1	0	5
AU95-012 1	162.04	17.2	12.4	182	1	15.4	4.9	6	2.4	0.5	0	0
AU95-012 2	214.01	12.3	11.2	159	1	18.6	3.7	6	2.2	0.4	0	0
AU95-012 3	95.18	13.2	9	67	5	13.6	2.4	58	6.4	8.5	0	0
AU95-012 4	56.62	12.3	11.1	181	209	8.8	3.2	4	1.1	0.3	0	0
AU95-012 5	77.1	12.3	12.3	209	8	10.5	1.2	5	4.7	11.8	0	4
AU95-012 6	130.24	27.4	8.7	126	1	7.1	2	3	4.4	0.4	0	0
Average	122.53	15.8	10.8	154	38	12.3	2.9	5	3.5	3.6	0	0
Std. Dev.	58.56	6	1.6	51	84	4.3	1.3	1	2	5.2	0	2
RSD	47.79	38.09	14.66	32.92	223.02	34.86	45.19	20.88	55.24	141.34	0	327.16
Blank 3/9/96 1	0.19	1.1	1.1	25	0	2.4	1.1	2	1.1	0.4	10	3
AU94-017 1	260.26	142	49.3	2113	1	11	97.4	46	25.2	1.7	9	0
AU94-017 2	97.45	62.2	54.7	1585	2	9	55	37	15.9	2	5	0
Average	179.85	102.1	52	1849	2	10	76.2	42	20.6	1.9	7	0
Std. Dev.	115.12	56.4	3.8	373	0	1.5	29.9	5	6.6	0.2	3	0
RSD	64.36	55.26	7.39	20.19	4.77	14.66	39.3	12.77	32.15	12.12	44.41	-6.17
AU94-022 1	878.82	60.8	148.8	30610	2	323.2	55.3	25	8.9	1.3	4	1
AU94-022 2	517.17	43.3	96.9	3413	1	191.8	56.1	23	5.7	1.6	2	0
AU94-022 3	451.98	36.4	76.9	2665	1	162.1	50.7	21	5.2	1.6	2	0
AU94-022 4	554.58	57.4	71.2	3059	1	200.6	51.2	23	5.7	1.98	3	0
AU94-022 5	316.93	31.3	43.6	1674	1	111.9	28.7	15	3.6	1.1	2	0
AU94-022 6	353.66	46.4	83.25	2077	1	124.3	58.6	25	4.5	1.6	3	0
Average	512.36	45.4	86.8	2658	1	185.7	50.1	22	5.6	1.5	2	0
Std. Dev.	201.56	11.6	35.1	663	0	76.1	10.9	4	1.8	0.3	1	0
RSD	39.34	25.43	40.46	24.95	35.56	40.97	21.76	17.14	32.39	16.81	29.93	104.98
AU94-007 1	207.92	36.4	21.7	977	1	79.9	68.5	38	4	1.6	3	0
AU94-007 2	260.91	51.1	22.3	1151	1	97.3	63.1	34	5.2	1.6	4	0
AU94-007 3	297.93	42.3	18.3	993	1	100.4	58.7	29	4.9	1.6	2	0
AU94-007 4	247.04	34.4	24.9	1064	2	95.5	87.4	38	5.8	1.9	4	0
Average	253.45	41.1	21.8	1046	1	93.3	69.4	35	5	1.7	3	0
Std. Dev.	37.18	7.5	2.7	80	1	9.2	12.7	4	0.8	0.1	1	0
RSD	14.67	18.25	12.4	7.62	48.25	9.82	18.25	11.8	15.35	7.94	24.65	31.05

Appendix 5, LA-ICP-MS data

Sample	V 51	Cr 52	Mn 55	Fe 57	Co 59	Ni 60	Zn 64	Cu 65	Ga 69	Ge 73	As 75	Se 82
Blank, 3/9/96 2	0.26	3.2	1.4	320	13	3.8	3.1	13	0.6	1.1	41	11
AU94-025 1	55.18	9.8	24.1	1362	0	22.6	15.6	21	1.2	0.5	1	0
AU94-025 2	30.85	9	41.5	946	-1	12.1	24.3	24	1.3	1.3	1	0
AU94-025 3	76.29	17	37.7	1433	-2	27.4	22.1	24	2	0.3	1	0
AU94-025 4	28.83	14.6	46.7	1398	-3	4.5	13.5	23	1.6	1.6	2	0
AU94-025 5	91.64	30.9	850.8	2900	5	33.6	46.3	26	2.7	0.4	3	0
AU94-025 6	32.95	11.2	21	712	-3	12.2	6.5	15	0.7	0.8	1	0
Average	52.62	15.4	170.3	1459	0	18.7	21.4	22	1.6	0.8	1	0
Std. Dev.	26.52	8.1	333.5	763	3	11	13.8	4	0.7	0.6	1	0
RSD	50.39	52.76	195.85	52.32	-666.64	58.56	64.36	18.05	44.07	70.55	46.52	63.36
AU95-019 1	23.89	12.1	7.3	3429	-2	3.6	24.1	21	2.4	0.4	4	0
AU95-019 2	14.4	6.6	5.4	2889	-3	1.2	5.4	9	1.3	0.9	0	0
AU95-019 3	18.16	98.8	9	5145	-5	8.4	23.7	31	3.5	0.1	6	1
AU95-019 4	21.16	14.3	13.6	3880	-3	64.2	12.4	32	7	21.9	-1	1
AU95-019 5	41.58	17.6	14.6	6563	-2	6.1	19.3	18	6.1	1.5	7	1
Average	23.84	12.1	10	4381	-3	16.7	17	22	4.1	5	3	0
Std. Dev.	10.52	4.2	4	1477	1	26.7	8	10	2.4	9.5	4	1
RSD	44.15	34.77	40	33.71	-39.74	159.92	47.22	43.67	59.02	190.76	120.14	137.53

Appendix 5, LA-ICP-MS data

Sample	Rb 85	Sr 88	Y 89	Zr 90	Nb 93	Mo 95	Rh 103	Pd 108	Ag 109	Cd 111	In 115	Sn 118
Blank, 28/8/96 1	0.09	0	0	0.006	0.04	0.03	0.002	0.003	0.02	0.02	0.015	0.17
AU95-012 1	1.18	10.314	25.985	459.449	77.9	4.39	0	0.016	73.73	0.14	0.094	5.25
AU95-012 2	1.59	11.515	23.155	417.992	59.37	4.34	0	0.01	71.11	0.12	0.102	4.41
AU95-012 3	1.09	10.296	19.656	428.936	61.67	2.84	0.048	0.189	11.78	6.13	1.146	9.65
AU95-012 4	0.73	4.348	15.283	240.591	67.44	2.64	0	0.01	60.01	0.13	0.047	4.51
AU95-012 5	1.8	5.249	16.316	338.912	44.26	4.67	0.285	0.13	5.77	12.31	0.09	3.48
AU95-012 6	0.61	9.634	31.91	452.854	93.68	4.13	0	0.01	7	0.05	0.09	7.41
Average	1.17	8.559	22.051	378.122	67.39	3.83	0.056	0.061	38.23	3.15	0.261	5.78
Std. Dev.	0.47	2.989	6.298	127.218	16.94	0.87	0.114	0.079	33.3	5.1	0.434	2.31
RSD	39.95	34.92	28.56	33.64	25.13	22.63	205.13	129.26	87.09	161.97	166	39.94
Blank 3/9/96 1	0.15	0.009	0.016	0.009	0.04	0.12	0.012	0.011	0.12	0.41	0.013	0.07
AU94-017 1	0.94	37.916	96.128	1044.615	326.29	25.63	-0.001	0.296	0.62	0.63	0.402	56.51
AU94-017 2	0.914	13.747	38.848	466.816	139.19	7.02	0.002	0.171	0.38	0.64	0.2	28.46
Average	0.93	25.832	67.488	755.715	232.74	16.32	0.001	0.234	0.5	0.63	0.301	42.48
Std. Dev.	0.02	17.09	40.503	408.566	132.3	13.16	0.002	0.089	0.17	0.01	0.142	19.84
RSD	2.24	66.16	60.02	54.06	56.84	80.64	335.54	38.05	34.05	1.72	47.31	46.69
AU94-022 1	3.26	81.226	12.772	256.273	30.09	42.12	0	0.085	0.22	0.3	0.196	11.27
AU94-022 2	1.6	60.837	17.203	457.89	47.02	25.09	0.006	0.095	0.23	0.23	0.186	9.45
AU94-022 3	2.09	50.184	18.443	526.98	36.13	23.09	0.008	0.096	0.17	0.55	0.149	9.55
AU94-022 4	2.27	64.086	15.69	270.411	36.85	25.72	0.007	0.046	3.46	0.23	0.186	11.32
AU94-022 5	1.22	36.41	21.798	400.216	35.09	16.3	0.009	0.073	0.17	0.17	0.1	9.39
AU94-022 6	2.4	34.971	22.375	501.93	45.82	19.51	0.004	0.119	0.33	0.74	0.173	10.97
Average	2.14	54.619	18.047	402.284	38.5	25.31	0.006	0.086	0.76	0.37	0.165	10.32
Std. Dev.	0.7	17.74	3.662	116.004	6.58	8.89	0.003	0.025	1.32	0.253	0.036	0.95
RSD	32.92	32.48	20.29	28.84	17.1	35.46	57.89	28.88	172.73	60.82	21.65	9.23
AU94-007 1	0.95	13.08	13.824	683.653	47.05	10.53	0.009	0.147	0.83	0.71	0.18	12.01
AU94-007 2	1.32	13.853	21.116	639.721	55.22	14.33	0.003	0.127	0.47	0.45	0.176	14.53
AU94-007 3	1.12	14.309	21.829	581.629	68.36	14.54	0.012	0.143	0.54	0.46	0.197	16.52
AU94-007 4	1.45	13.567	15.794	632.705	73.93	12.78	0.005	0.176	0.63	1.19	0.193	20.63
Average	1.21	13.701	183.141	634.427	61.39	13.04	0.007	0.148	0.62	0.7	0.186	15.93
Std. Dev.	0.22	0.516	3.941	41.8	11.86	1.85	0.004	0.02	0.16	0.35	0.01	3.64
RSD	18.34	3.76	21.73	6.59	19.32	14.19	58.35	13.8	25.26	49.27	5.57	22.86

Appendix 5, LA-ICP-MS data

Sample	Rb 85	Sr 88	Y 89	Zr 90	Nb 93	Mo 95	Rh 103	Pd 108	Ag 109	Cd 111	In 115	Sn 118
Blank, 3/9/96 2	0.21	0.01	0.027	0.047	0.03	0.39	0.028	0.027	0.05	0.15	0.038	0.035
AU94-025 1	0.58	3.242	6.166	183.252	26.86	3.19	-0.006	0.04	0.12	0.4	0.0478	4.33
AU94-025 2	0.76	2.312	14.947	288.877	27.93	1.5	-0.009	0.087	0.21	0.24	0.022	3.35
AU94-025 3	0.98	7.321	7.238	181.524	43.74	4.85	0.011	0.117	0.08	0.18	0.046	4.31
AU94-025 4	1.03	4.042	8.548	187.485	40.94	2.5	-0.013	0.09	0.24	0.17	0.043	4.58
AU94-025 5	1.37	7.751	11.625	321.793	53.81	6.58	-0.007	0.096	0.12	0.3	0.054	6.78
AU94-025 6	0.44	2.519	4.234	142.166	24.59	1.72	-0.004	0.032	0.08	0.31	0.037	3.27
Average	0.86	4.531	8.793	217.516	36.31	3.39	-0.04	0.077	0.14	0.27	0.041	4.44
Std. Dev.	0.34	2.409	3.9	70.732	11.66	1.98	0.008	0.034	0.07	0.09	0.011	1.27
RSD	39.21	53.17	44.36	32.52	32.11	58.32	-188.37	43.8	49.34	33.7	26.73	28.67
AU95-019 1	0.76	4.473	4.471	154.246	29.95	1.39	-0.001	0.032	0.73	0.11	0.035	3.69
AU95-019 2	0.41	1.375	1.647	82.2	13.2	2.98	-0.006	0.049	0.17	0.19	0.042	2.86
AU95-019 3	0.7	4.126	1.452	48.152	15.37	0.73	-0.003	0.035	0.81	0.38	0.033	2.75
AU95-019 4	1.14	3.384	4.176	285.985	29.52	2.92	0.037	0.109	0.79	0.6	0.127	4.24
AU95-019 5	0.86	6.882	12.063	452.323	37.1	1.96	-0.007	0.11	1.44	0.08	0.049	4.92
Average	0.77	4.048	4.762	204.581	25.03	2	0.004	0.067	0.79	0.27	0.057	3.69
Std. Dev.	0.26	1.988	4.313	165.819	10.29	0.97	0.019	0.039	0.46	0.22	0.04	0.92
RSD	34.28	49.1	90.57	81.05	41.1	48.74	450.74	58.31	57.08	80.2	69.2	24.9

Appendix 5, LA-ICP-MS data

Sample	Sb 121	Te 125	Cs 133	Ba 138	La 139	Ce 140	Pr 141	Nd 146	Sm 147	Eu 151	Gd 157	Tb 159
Blank, 28/8/96 1	0.04	0.03	0.02	0.011	0.026	0.011	0.019	0.09	0.026	0.02	0.03	0.009
AU95-012 1	1.08	0.07	0.07	49.248	3.259	8.775	1.075	5.08	1.546	0.52	2.34	0.66
AU95-012 2	0.87	0.06	0.1	60.088	2.903	6.968	1.366	4.76	1.228	0.34	2.51	0.535
AU95-012 3	4.21	8.46	0.48	39.592	2.969	6.496	0.965	8.86	3.57	1.51	8.13	1.45
AU95-012 4	0.83	0	0.03	19.054	2.118	4.589	0.547	2.41	0.81	0.2	1.24	0.335
AU95-012 5	2.13	8.63	1.86	27.802	3.767	4.144	1.169	6.49	8.923	-0.81	14.48	0.341
AU95-012 6	1.15	0.08	0.06	47.874	2.968	6.07	0.822	4.17	1.209	0.36	2.47	0.621
Average	1.71	2.88	0.43	40.61	3.164	6.174	0.991	5.29	2.881	0.35	5.19	0.658
Std. Dev.	1.31	4.39	0.73	15.077	0.666	1.682	0.285	2.2	3.117	0.74	5.16	0.414
RSD	76.63	152.15	166.62	37.13	21.06	27.24	28.78	41.48	108.2	209.4	99.37	62.9
Blank 3/9/96 1	0.05	0.08	0.02	0.019	0.012	0	0.003	0.02	0.019	0.03	0.04	0
AU94-017 1	6.61	0.16	0.09	105.409	39.719	85.083	11.245	39.73	10.826	2.97	13.65	3.148
AU94-017 2	3.24	0.1	0.06	63.325	8.089	20.46	2.085	8.84	2.723	0.77	4.15	0.928
Average	4.93	0.13	0.07	84.367	23.904	52.772	6.665	24.28	6.774	1.87	8.9	2.038
Std. Dev.	2.38	0.04	0.02	29.758	22.366	45.695	6.477	21.84	5.73	1.56	6.72	1.57
RSD	48.25	31.33	25.84	35.27	93.57	86.59	97.18	89.96	84.59	83.34	75.53	77.04
AU94-022 1	0.95	0.09	0.26	672.472	4.553	14.27	1.051	5.15	1.295	0.27	1.68	0.371
AU94-022 2	1.2	0.03	0.05	430.511	2.39	5.913	0.65	2.73	1.078	0.33	1.92	0.5
AU94-022 3	1.16	0.02	0.18	427.364	3.401	8.496	0.848	3.43	1.685	0.28	1.91	0.516
AU94-022 4	1.16	0.16	0.11	489.063	3.467	7.565	0.756	2.55	0.781	0.25	1.74	0.437
AU94-022 5	0.75	0.06	0.1	285.464	2.649	5.596	0.578	2.52	1.049	0.39	2.39	0.583
AU94-022 6	1.01	0.05	0.17	318.343	4.942	11.181	1.087	5.27	1.468	0.26	1.79	0.549
Average	1.04	0.07	0.14	437.203	3.567	8.837	0.828	3.61	1.226	0.3	1.9	0.493
Std. Dev.	0.17	0.05	0.08	138.083	1.013	3.341	0.208	1.28	0.324	0.05	0.25	0.077
RSD	16.7	77	52.05	31.58	28.4	37.8	25.13	35.59	26.44	17.38	13.35	15.68
AU94-007 1	1..22	0.04	0.05	131.769	1.709	6.066	0.618	2.75	1.032	0.31	1.26	0.343
AU94-007 2	1.69	0.06	0.07	127.943	1.947	6.4	0.597	3.08	1.256	0.33	2.01	0.49
AU94-007 3	3.33	0.03	0.05	140.378	2.943	6.989	0.729	4.42	1.193	0.32	1.76	0.464
AU94-007 4	2.04	0.06	0.06	115.786	1.828	6.3346	0.723	3.21	1.101	0.34	1.57	0.402
Average	2.07	0.05	0.06	128.969	2.107	6.45	0.667	3.37	1.145	0.32	1.65	0.425
Std. Dev.	0.9	0.02	0.01	10.212	0.566	0.388	0.069	0.73	0.099	0.01	0.32	0.066
RSD	43.68	35.84	11.96	7.92	26.86	6.01	10.34	21.65	8.62	4.62	19.14	15.56

Appendix 5, LA-ICP-MS data

Sample	Sb 121	Te 125	Cs 133	Ba 138	La 139	Ce 140	Pr 141	Nd 146	Sm 147	Eu 151	Gd 157	Tb 159
Blank, 3/9/96 2	0.13	0.18	0.07	0.015	0.013	0	0.025	0	0.042	0.06	0.09	0.016
AU94-025 1	0.49	0	0.02	15.615	1.551	4.266	0.388	1.46	0.389	0.06	0.46	0.088
AU94-025 2	0.69	0	0.04	14.852	0.821	2.855	0.215	0.9	0.328	0.05	0.85	0.174
AU94-025 3	0.93	-0.09	0.02	24.99	4.495	6.676	0.512	2.87	0.666	0.09	0.76	0.175
AU94-025 4	0.72	-0.05	0.05	19.472	1.999	6.007	0.496	1.73	0.535	0.1	1.11	0.159
AU94-025 5	1.09	0.15	0.06	38.234	3.28	8.523	0.823	2.77	0.719	0.19	1.15	0.215
AU94-025 6	0.3	0	0.05	13.195	0.598	1.87	0.169	0.53	0.334	0.08	0.32	0.098
Average	0.7	0	0.04	21.06	2.124	5.033	0.434	1.71	0.495	0.09	0.77	0.151
Std. Dev.	0.29	0.08	0.02	9.412	1.505	2.496	0.237	0.95	0.171	0.05	0.34	0.049
RSD	40.55	2583.66	39.69	44.69	70.87	49.6	54.69	55.85	34.52	53.98	43.76	32.43
AU95-019 1	0.71	-0.05	0.01	79.25	1.525	4.629	0.384	1.45	0.415	0.11	0.5	0.093
AU95-019 2	0.21	-0.02	0.01	21.681	0.342	1.073	0.108	0.32	0.21	0.02	0.18	0.022
AU95-019 3	0.53	0	0.02	35.677	1.611	6.613	0.692	1.93	0.236	0.02	0.38	0.045
AU95-019 4	1.62	-0.03	0.14	27.001	1.466	4.869	0.405	2.85	0.358	0.1	0.32	0.074
AU95-019 5	0.97	0	0.1	41.695	4.02	14.614	1.368	4.56	1.119	0.35	1.27	0.149
Average	0.81	-0.02	0.06	41.061	1.793	6.36	0.592	2.22	0.468	0.12	0.583	0.097
Std. Dev.	0.53	0.02	0.06	22.699	1.349	5.034	0.481	1.59	0.374	0.14	0.43	0.089
RSD	66.05	-119.26	103.98	55.28	75.25	79.16	81.27	71.81	79.98	113.93	80.71	92.36

Appendix 5, LA-ICP-MS data

Sample	Dy 163	Ho 165	Er 166	Tm 169	Yb 174	Lu 175	Hf 177	Ta 181	W 182	Re 185	Os 192	Ir 193
Blank, 28/8/96 1	0.03	0.012	0.014	0.002	0.006	0	0	0.003	0	0	0	0
AU95-012 1	4.44	1.227	4.094	0.709	4.929	0.858	21.11	6.892	6.117	0.019	0.0002	0
AU95-012 2	3.95	1.093	3.341	0.648	4.102	0.707	15.445	5.196	5.451	0.016	0.0002	0
AU95-012 3	4.29	1.841	3.956	0.976	4.717	1.856	11.693	6.593	8.683	-0.039	0.3575	0.12
AU95-012 4	2.42	0.664	2.174	0.398	2.553	0.432	8.159	5.235	6.069	0.004	0.0003	0
AU95-012 5	9.68	2.769	83.913	0.5	6.45	0.9	18.971	5.368	5.754	-0.047	0.0409	0.093
AU95-012 6	4.28	1.17	3.68	0.678	4.229	0.73	17.118	7.249	7.008	0.008	0.0004	0
Average	4.84	1.461	4.36	0.651	4.497	0.914	15.416	6.089	6.513	-0.007	0.0666	0.036
Std. Dev.	2.48	0.744	2.334	0.198	1.269	0.49	4.785	0.927	1.184	0.029	0.1435	0.056
RSD	51.24	50.981	53.54	30.42	28.323	53.59	31.04	15.22	18.18	-428.24	215.46	156.42
Blank 3/9/96 1	0.03	0	0	0.006	0.009	0.009	0.016	0.011	0.013	0	0	
AU94-017 1	21.79	4.537	14.39	2.382	17.517	2.155	41.22	27.549	43.662	0.006	0	
AU94-017 2	6.91	1.662	5.18	0.78	6.075	0.904	17.893	11.643	16.819	0.003	0	
Average	14.35	3.1	9.785	1.581	11.796	1.529	29.556	19.596	30.241	0.004	0	
Std. Dev.	10.52	2.033	6.512	1.133	8.091	0.884	16.494	11.247	18.981	0.002	0	
RSD	73.33	65.58	66.55	71.65	68.59	57.84	55.81	57.4	62.77	40.28	0	
AU94-022 1	3.67	0.693	2.368	0.384	3.033	0.436	10.259	3.22	5.638	0.384	0	
AU94-022 2	3.48	0.813	3.202	0.582	3.819	0.634	18.076	4.165	5.952	0.201	0	
AU94-022 3	5.37	1.081	3.076	0.617	3.886	0.648	19.493	3.857	6.354	0.165	0	
AU94-022 4	3.44	0.824	3.278	0.393	3.407	0.451	10.761	4.272	8.262	0.261	0.0446	
AU94-022 5	7.21	13.033	3.748	0.535	4.266	0.582	15.202	3.482	4.744	0.108	0.0097	
AU94-022 6	4.31	0.816	2.824	0.502	4.058	0.658	20.601	4.619	7.8724	0.119	0.0268	
Average	4.58	0.877	3.083	0.052	3.745	0.568	15.732	3.936	6.462	0.207	0.0135	
Std. Dev.	1.48	0.149	0.463	0.096	0.451	0.1	4.434	0.521	1.341	0.103	0.0185	
RSD	32.28	16.94	15.02	19.17	12.04	17.65	28.18	13.23	20.76	50.04	136.77	
AU94-007 1	2.71	0.653	2.381	0.443	3.416	0.62	27.358	4.599	5.5273	0.072	0.0209	
AU94-007 2	3.88	0.891	3.235	0.58	4.237	0.712	23.651	5.177	7.78	0.119	0.0275	
AU94-007 3	3.59	0.975	3.448	0.59	5.634	0.791	22.433	6.376	7.598	0.105	0.013	
AU94-007 4	3.04	0.75	2.537	0.447	3.427	0.577	25.932	6.935	7.954	0.062	0.0135	
Average	3.31	0.817	2.9	0.515	4.179	0.675	24.844	5.772	7.226	0.09	0.0187	
Std. Dev.	0.53	0.144	0.521	0.081	1.044	0.096	2.217	1.072	1.112	0.027	0.0068	
RSD	15.92	17.58	17.95	15.38	24.98	14.2	8.92	18.57	15.39	29.69	36.52	

Appendix 5, LA-ICP-MS data

Sample	Dy 163	Ho 165	Er 166	Tm 169	Yb 174	Lu 175	Hf 177	Ta 181	W 182	Re 185	Os 192	Ir 193
Blank, 3/9/96 2	0.05	0.024	0.041	0.01	0	0.018	0.018	0.009	0.015	0.033		0.025
AU94-025 1	0.93	0.197	0.838	0.141	1.056	0.178	5.842	2.275	2.799	0.014		0.032
AU94-025 2	1.88	0.542	2.31	0.408	25.926	0.385	9.791	2.158	2.48	-0.007		-0.016
AU94-025 3	1.11	0.264	1.044	0.175	1.232	0.14	5.657	2.701	4.492	0		0
AU94-025 4	1.26	0.329	1.033	0.171	1.494	0.204	5.542	2.578	4.373	0		-0.018
AU94-025 5	1.86	0.439	1.645	0.298	1.907	0.329	10.82	3.811	7.478	0.04		0.013
AU94-025 6	0.58	0.111	0.457	0.085	0.758	0.162	4.796	1.608	2.273	0.007		-0.015
Average	1.27	0.314	1.221	213	1.562	0.233	7.075	2.522	3.983	0.009		-0.001
Std. Dev.	0.52	0.158	0.657	0.118	0.774	0.1	2.549	0.738	1.96	0.017		0.02
RSD	40.63	50.44	53.83	55.54	49.56	42.79	36.02	29.27	49.21	181.82		-3096.17
AU95-019 1	0.66	0.196	0.577	0.112	0.641	0.117	4.793	1.901	2.816	0		-0.012
AU95-019 2	0.32	0.056	0.264	0.036	0.452	0.043	2.145	0.916	1.342	-0.018		0
AU95-019 3	0.22	0.06	0.265	0.036	0.361	0.032	1.622	0.878	1.21	-0.019		0.022
AU95-019 4	0.68	0.167	0.547	0.09	0.922	0.17	9.951	1.648	3.742	-0.009		0.041
AU95-019 5	1.8	0.403	1.514	0.281	2.556	0.332	14.309	2.429	3.279	-0.005		0.026
Average	0.73	0.176	0.633	0.111	0.986	0.139	6.564	1.554	2.478	-0.01		0.015
Std. Dev.	0.63	0.141	0.514	0.101	0.904	0.122	5.444	0.663	1.146	0.008		0.021
RSD	85.15	80.22	81.23	90.91	91.61	87.83	82.94	42.65	46.24	-80.8		137.45

Appendix 5, LA-ICP-MS data

Sample	Pt 195	Au 197	Hg 200	Tl 205	Pb 208	Bi 209	Th 232	U 238
Blank, 28/8/96 1	0	0.34	0.1	0.002	0.02	0.007	0	0.0029
AU95-012 1	0	0.27	1.1	0.055	6.4	0.787	7.368	10.7671
AU95-012 2	0.001	0	0.8	0.043	6.18	0.997	6.0573	11.1862
AU95-012 3	0.0084	0	3.4	1.889	4.57	0.439	6.7937	58.7818
AU95-012 4	0	0	0.8	0.005	2.97	0.175	4.4285	5.2982
AU95-012 5	0.0387	0	0.4	0.864	3.44	1.106	4.5196	7.1828
AU95-012 6	0.0001	0	0.3	0.024	5.8	0.595	7.7774	9.493
Average	0.0079	0.05	1.1	0.48	4.89	0.683	6.1574	8.2849
Std. Dev.	0.0155	0.11	1.2	0.767	1.46	0.35	1.4266	2.5471
RSD	196.14	244.1	103.47	159.72	29.81	51.26	23.17	30.74
Blank 3/9/96 1	0	0	0.7	0	0.05	0.021	0.0049	0.0045
AU94-017 1	0.0013	0	5.2	0.097	78.71	2.52	36.6916	33.0174
AU94-017 2	0.0007	0	4.9	0.064	42.43	1.218	13.3424	14.3441
Average	0.001	0	5	0.081	60.57	1.869	25.017	23.6807
Std. Dev.	0.0004	0	0.2	0.024	25.66	0.92	16.5104	13.204
RSD	40.28	-141.42	4.3	29.49	42.36	49.23	66	55.76
AU94-022 1	0.0013	0.08	105.1	0.126	15.74	0.539	5.8906	5.831
AU94-022 2	0.0008	0.33	17.8	0.045	19.29	0.62	5.8354	6.3913
AU94-022 3	0	0.32	11	0.088	13.73	0.443	4.9139	4.6511
AU94-022 4	0.0009	0.51	19.6	0.06	13.21	0.346	3.4874	4.2336
AU94-022 5	0.0006	0.28	5	0.037	10.34	0.356	3.9435	4.1167
AU94-022 6	0.003	0.26	7.3	0.077	15.76	0.365	7.0718	5.5103
Average	0.0011	0.3	27.6	0.072	14.68	0.445	5.2404	5.1223
Std. Dev.	0.001	0.14	38.4	0.032	3.01	0.113	1.2673	0.9259
RSD	91.41	46.48	138.91	44.72	20.53	25.39	24.18	18.08
AU94-007 1	0.0007	0.12	3.4	0.044	20.984	0.432	5.0458	11.6921
AU94-007 2	0.00148	0	3.6	0.074	21.76	0.584	6.4152	13.0001
AU94-007 3	0.0087	0.02	3.5	0.063	21.17	0.783	6.0467	12.3392
AU94-007 4	0.0013	0	3	0.06	21.96	0.586	6.4186	10.3352
Average	0.0031	0.03	3.4	0.06	21.46	0.596	5.9816	11.8416
Std. Dev.	0.0038	0.06	0.3	0.012	0.48	0.144	0.6478	1.1374
RSD	121.29	165.47	8.19	20.29	2.25	24.14	10.83	9.61

Appendix 5, LA-ICP-MS data

Sample	Pt 195	Au 197	Hg 200	Tl 205	Pb 208	Bi 209	Th 232	U 238
Blank, 3/9/96 2	0	0.01	2.6	0.007	0.19	0.036	0	0
AU94-025 1	0	0.01	1.1	0.009	6.1	0.157	1.8334	2.6526
AU94-025 2	0	0	1.52	0.028	6.33	0.121	1.87871	3.8977
AU94-025 3	0	0	1.9	0.011	5.97	0.22	2.9694	3.813
AU94-025 4	0.0019	0.01	1.4	5	4.78	0.221	3.2046	3.6224
AU94-025 5	0.0006	0	2.5	0.158	13.04	412	4.8197	6.8361
AU94-025 6	0.0022	0	0.7	0.013	3.28	0.135	1.3593	2.787
Average	0.0008	0	1.5	0.038	6.58	0.211	2.6789	3.9348
Std. Dev.	0.001	0	0.6	0.06	3.36	0.107	1.2671	1.5161
RSD	128.12	121.81	40.91	158.84	51.06	50.73	47.3	38.53
AU95-019 1	0.0006	0.01	1.1	0.004	5.79	0.2	1.5415	2.2602
AU95-019 2	0.0013	0	0.4	0	2.04	0.038	0.8479	1.2338
AU95-019 3	0.0022	0.01	1.8	0.013	8.06	0.161	1.4198	1.316
AU95-019 4	0.0021	0	1.2	0.018	8.2	0.191	1.6502	4.1581
AU95-019 5	0.002	0.01	0.9	0.019	11.07	0.315	4.1088	5.3165
Average	0.0016	0.01	1.1	0.01	7.03	0.181	1.9136	2.8569
Std. Dev.	0.0007	0	0.5	0.008	3.36	0.099	1.2655	1.8102
RSD	40.25	73.46	45.96	79.85	47.78	54.69	66.13	63.36

Appendix 6, ILC data

sample	Cl	Br	NO3	PO4	SO4	Li	Na
94-007	0.48	<D.L.	<D.L.	<D.L.	1.65	<D.L.	0.42
94-017	0.32	0.09	0.12	<D.L.	3.21	0.10	0.39
94-022	0.21	0.09	0.12	<D.L.	2.68	<D.L.	0.19
94-023	0.21	<D.L.	0.04	<D.L.	0.83	<D.L.	0.18
94-024	0.25	<D.L.	0.27	<D.L.	0.93	<D.L.	0.15
94-030	0.41	<D.L.	0.66	<D.L.	6.24	<D.L.	1.09
94-031	0.25	<D.L.	0.26	<D.L.	1.17	<D.L.	0.18
94-037	0.24	<D.L.	0.06	<D.L.	2.02	<D.L.	0.22
94-046	0.48	<D.L.	0.06	<D.L.	5.61	0.08	0.74
94-078A	0.62	<D.L.	0.01	<D.L.	29.94	0.09	0.84
94-078B	0.61	<D.L.	0.62	<D.L.	29.94	0.09	0.92
95-002	0.61	<D.L.	0.19	<D.L.	1.06	0.07	1.00
95-003	0.31	<D.L.	0.06	<D.L.	2.62	<D.L.	0.40
95-009	0.35	<D.L.	<D.L.	<D.L.	3.89	<D.L.	0.33
95-011	0.45	<D.L.	<D.L.	<D.L.	1.80	0.16	0.82
95-012	0.29	<D.L.	0.06	<D.L.	1.15	0.09	0.42
96-999B	0.06	<D.L.	0.09	<D.L.	0.09	0.13	0.05
95-013	0.36	<D.L.	0.04	<D.L.	2.95	0.07	0.41
95-014	0.27	<D.L.	0.04	<D.L.	4.10	0.07	0.41
95-015	0.28	<D.L.	0.07	<D.L.	2.68	0.07	0.38
95-016	0.32	<D.L.	<D.L.	<D.L.	0.71	0.09	0.50
95-020A	0.35	<D.L.	<D.L.	<D.L.	0.87	0.07	0.36
95-021B	0.32	<D.L.	<D.L.	<D.L.	0.98	0.07	0.37
95-023	0.39	<D.L.	<D.L.	<D.L.	0.79	0.12	0.56
95-024	0.28	<D.L.	<D.L.	<D.L.	5.18	<D.L.	0.75
95-025	0.30	<D.L.	0.06	<D.L.	6.56	0.07	0.37
96-999C	0.05	<D.L.	<D.L.	<D.L.	0.10	<D.L.	<D.L.
94-007	0.30	<D.L.	<D.L.	<D.L.	1.22	0.07	0.29
95-017	0.28	<D.L.	<D.L.	<D.L.	0.64	0.04	0.23
95-011	0.35	<D.L.	<D.L.	<D.L.	2.57	0.07	0.34
95-026	0.45	<D.L.	<D.L.	<D.L.	4.53	<D.L.	0.21
96-002	0.97	<D.L.	<D.L.	<D.L.	0.13	0.07	0.60
96-009	0.33	<D.L.	<D.L.	<D.L.	1.33	0.07	0.28
96-011	0.37	<D.L.	<D.L.	<D.L.	1.36	0.07	0.25
96-012	0.16	<D.L.	<D.L.	<D.L.	0.76	0.03	0.28
96-014	0.27	<D.L.	<D.L.	0.13	2.30	<D.L.	0.41
96-015	0.27	<D.L.	<D.L.	<D.L.	1.19	0.04	0.21
96-041	0.70	<D.L.	<D.L.	<D.L.	202.82	0.17	2.34
96-999D	0.04	<D.L.	<D.L.	<D.L.	0.06	<D.L.	<D.L.
	dark stipple = below calibration concentrations						
	light stipple = near calibration concetrations						

Appendix 6, ILC data

sample	NH4	K	Mg	Ca
94-007	0.08	0.76	0.56	19.20
94-017	0.28	1.85	8.17	23.07
94-022	0.15	0.66	0.25	1.88
94-023	0.16	0.58	0.24	1.54
94-024	0.07	0.34	0.26	1.95
94-030	0.34	1.11	0.82	9.15
94-031	0.38	0.64	0.28	3.45
94-037	0.19	0.78	0.55	16.46
94-046	0.28	0.88	0.74	4.03
94-078A	0.17	1.30	4.37	35.72
94-078B	0.16	1.55	4.27	35.59
95-002	<D.L.	1.31	1.12	5.46
95-003	<D.L.	0.93	0.86	5.31
95-009	0.14	0.91	0.51	2.42
95-011	<D.L.	0.82	0.37	1.07
95-012	0.30	0.70	0.26	0.71
96-999B	0.23	<D.L.	0.27	<D.L.
95-013	0.27	0.31	0.24	1.64
95-014	0.32	0.75	0.28	2.79
95-015	0.31	0.83	0.27	1.81
95-016	0.16	0.62	0.28	1.00
95-020A	0.16	0.72	0.24	0.93
95-021B	0.17	0.73	0.22	1.19
95-023	0.18	0.66	0.32	2.46
95-024	<D.L.	0.47	0.21	3.74
95-025	0.44	0.77	0.38	4.35
96-999C	0.21	<D.L.	0.13	<D.L.
94-007	0.17	0.70	0.45	19.36
95-017	0.16	0.66	0.41	7.12
95-011	<D.L.	0.81	0.31	2.12
95-026	0.15	0.70	0.40	5.24
96-002	0.21	0.52	0.24	1.38
96-009	0.07	0.79	0.29	1.40
96-011	0.25	0.65	0.55	1.68
96-012	0.20	0.29	0.18	0.62
96-014	0.18	0.67	0.21	1.75
96-015	0.16	0.67	0.51	2.57
96-041	0.36	3.60	6.87	142.31
96-999D	0.22	0.34	0.14	<D.L.

Appendix 7, Rock Eval. data

Rock Eval.	QTY	TMAX	S1	S2	S3	PI	S2/S3	PC	TOC	HI	OI
AU94-007	100.1	422	0.43	1.07	0.34	0.29	3.14	0.12	0.25	428	136
AU94-007	99.5	421	0.44	1.09	0.35	0.29	3.11	0.12	0.25	436	140
AU94-017	100.1	411	0.03	0.27	0.59	0.1	0.45	0.02	0.21	128	280
AU94-017	100.6	407	0.03	0.29	0.5	0.09	0.58	0.02	0.02	145	250
AU94-022	100.2	418	1.23	3.81	0.54	0.24	7.05	0.43	0.8	476	67
AU94-022	100.2	418	1.32	3.91	0.52	0.25	7.51	0.43	0.8	488	65
AU94-023	99.6	425	0.09	0.47	0.31	0.16	1.51	0.04	0.13	361	238
AU94-023	99.9	419	0.08	0.45	0.26	0.15	1.73	0.04	0.13	346	200
AU94-024	99.8	425	0.13	0.7	0.35	0.16	2	0.06	0.18	388	194
AU94-024	99.7	426	0.13	0.67	0.35	0.16	1.91	0.06	0.18	372	194
AU94-030	100.8	418	1.57	6.34	0.56	0.2	11.32	0.65	1.22	519	45
AU94-030	100.4	419	1.55	6.31	0.57	0.2	11.07	0.65	1.22	517	46
AU94-037	100	422	0.28	0.82	0.37	0.25	2.21	0.09	0.21	390	176
AU94-037	99.6	423	0.26	0.74	0.39	0.26	1.89	0.08	0.21	352	185
AU94-046	100.5	416	6.48	7.64	0.43	0.46	17.76	1.17	1.63	468	26
AU94-046	100.6	413	6.5	7.39	0.44	0.47	16.79	1.15	1.61	459	27
AU94-062	100.4		0.01	0	0.28		0	0	0.05	0	560
AU94-062	100.2		0	0	0.23		0	0	0.03	0	766
AU94-062	100.6	332	0	0.01	0.14		0.07	0	0.03	33	466
AU94-062	100	345	0.02	0.04	0.22	0.33	0.18	0	0.04	100	550
AU94-062	100.1	421	0.01	0.01	0.22	0.5	0.04	0	0.03	33	733
AU94-078	100.8	417	0.02	0.17	6.07	0.11	0.02	0.01	0.32	53	1896
AU94-078	100.3	418	0.01	0.16	5.98	0.06	0.02	0.01	0.32	50	1868
AU94-079	100.5	417	0.01	0.02	0.33	0.5	0.06	0	0.07	28	471
AU94-079	99.8	421	0.03	0.08	0.34	0.3	0.23	0	0.08	100	425
AU95-02	100.5	418	1.55	1.44	0.19	0.52	7.57	0.24	0.39	369	48
AU95-002	100.1	414	1.59	1.27	0.27	0.56	4.7	0.23	0.39	325	69
AU95-003	99.4	418	0.59	1.89	0.34	0.24	5.22	0.2	0.42	450	80
AU95-003	100.4	418	0.53	1.77	0.34	0.23	5.2	0.19	0.4	442	85
AU95-009	99.8	419	0.04	0.13	0.14	0.25	0.921	0.01	0.06	216	233
AU95-009	100.2	413	0.03	0.1	0.1	0.25	1	0.01	0.06	166	166
AU95-011	100.5	416	0.3	1.11	0.35	0.21	3.17	0.11	0.32	346	109
AU95-011	100.2	417	0.38	1.49	0.37	0.2	4.02	0.15	0.34	438	108
AU95-012	100.5	422	0.76	1.61	0.38	0.32	4.23	0.19	0.4	402	95
AU95-012	99.8	421	0.81	1.81	0.4	0.32	4.27	0.21	0.41	417	97

Appendix 7, Rock Eval. data

Rock Eval.	QTY	TMAX	S1	S2	S3	PI	S2/S3	PC	TOC	HI	OI
AU95-013	100.4	418	2.81	4.82	0.46	0.37	10.47	0.63	1.06	454	45
AU95-013	99.7	418	2.82	4.87	0.46	0.37	10.14	64	1.07	455	44
AU95-014	99.8	415	1.79	2.94	0.48	0.38	6.12	0.39	0.72	408	66
AU95-014	99.6	418	1.81	3.12	0.46	0.37	6.78	0.41	0.73	427	63
AU95-015	99.7	419	0.37	1.52	0.39	0.2	3.89	0.15	0.35	434	111
AU95-015	100.1	422	0.28	1.26	0.38	0.18	3.31	0.12	0.34	370	111
AU95-016	99.9	418	0.06	0.36	0.22	0.14	1.63	0.03	0.17	211	129
AU95-016	100	418	0.08	0.4	0.21	0.17	1.9	0.04	0.16	250	131
AU95-016	100.2		0	0	0.05		0	0	0.01	0	500
AU95-017	100.5		0	0	0.04		0	0	0		
AU95-017	100.3		0	0	0.01		0	0	0		
AU95-017	100.2		0	0	0.07		0	0	0		
AU95-019	99.8	419	0.07	0.27	0.2	0.21	1.35	0.02	0.13	207	153
AU95-019	100.3	420	0.07	0.27	0.2	0.21	1.35	0.02	0.11	245	184
AU95-020	99.9	416	0.06	0.1	0.09	0.37	1.11	0.01	0.05	200	180
AU95-020	100	413	0.05	0.07	0.06	0.42	1.16	0.01	0.05	140	120
AU95-021	100.4	419	0.26	0.57	0.25	0.32	2.28	0.06	0.21	271	119
AU95-021	100.3	420	0.24	0.56	0.26	0.3	2.15	0.06	0.18	311	144
AU95-023	100.5	417	0.23	0.36	0.26	0.4	1.38	0.04	0.18	200	144
AU95-023	100.3	423	0.25	0.43	0.25	0.37	1.72	0.05	0.19	226	131
AU95-024	99.5	420	1.32	6.51	0.41	0.17	15.87	0.65	1.3	500	31
AU95-024	99.9	421	1.32	6.06	0.44	0.18	13.77	0.61	1.27	477	34
AU95-025	100.4	417	4.98	14.42	0.68	0.26	21.2	1.61	2.95	488	23
AU95-025	100.3	416	4.88	14.23	0.69	0.26	20.62	1.59	2.92	487	23
standards											
9108	100.8	413	0.05	1.17	0.98	0.4	1.19	0.1	2.3	50	42
9108	99.9	418	0.06	1.15	0.96	0.05	1.19	0.1	2.31	49	41
9108	100	411	0.07	1.14	1.05	0.06	1.08	0.1			
9108	100.1	413	0.06	1.2	1	0.05	1.2	0.1	2.33	51	42
9108	99.7	415	0.06	1.14	0.99	0.05	1.15	0.1	2.36	48	41
9108	100.2	415	0.01	0.98	1	0.01	0.98	0.08	2.28	42	43
9108	100.8	409	0.05	1.07	1.05	0.04	1.01	0.09	2.31	46	45
9108	99.8	414	0.07	1.22	1.01	0.05	1.2	0.1			
9108	100.2	416	0.07	1.27	0.97	0.05	1.3	0.11	2.37	53	40

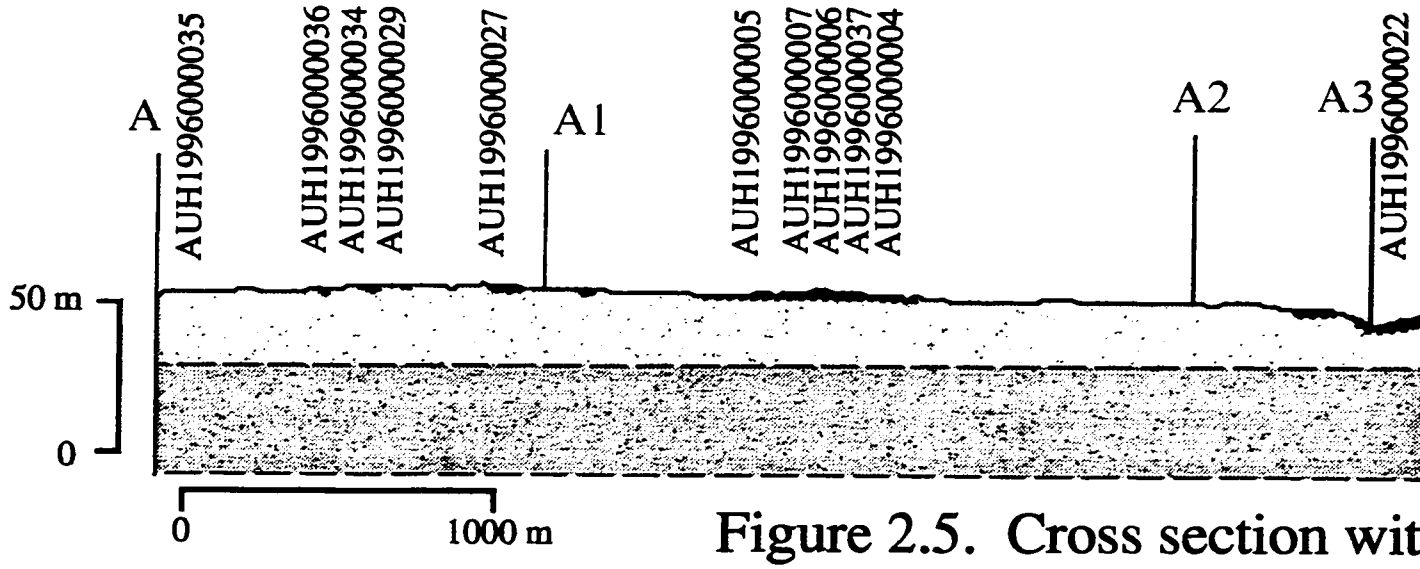

Figure 2.5. Cross section wit

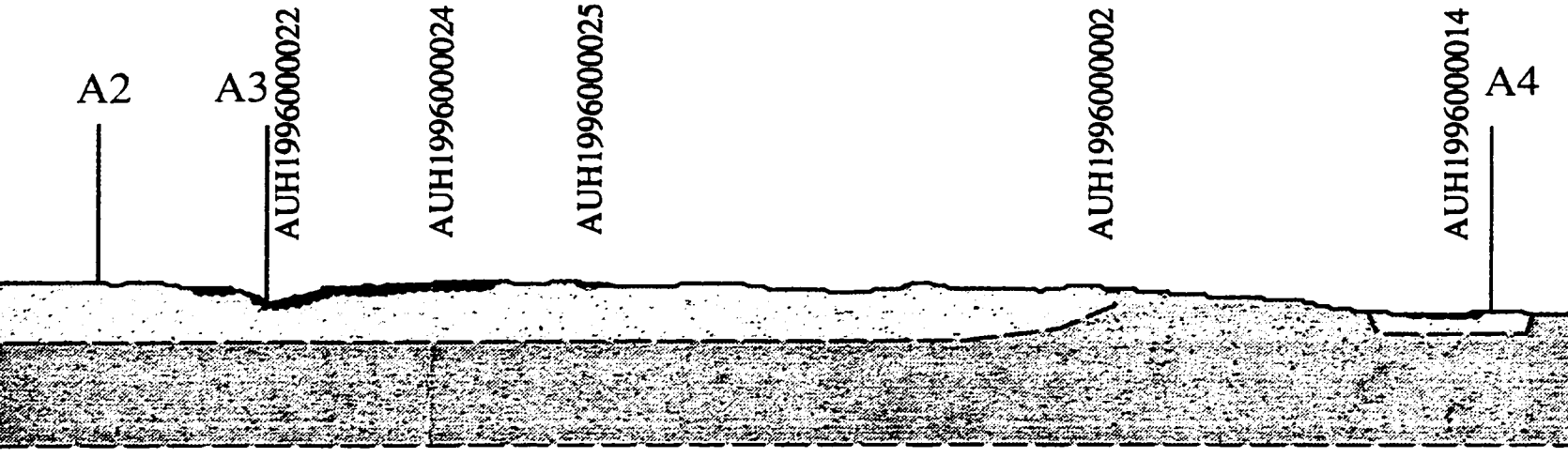

oss section with view towards the east; vertical exaggeration = 10

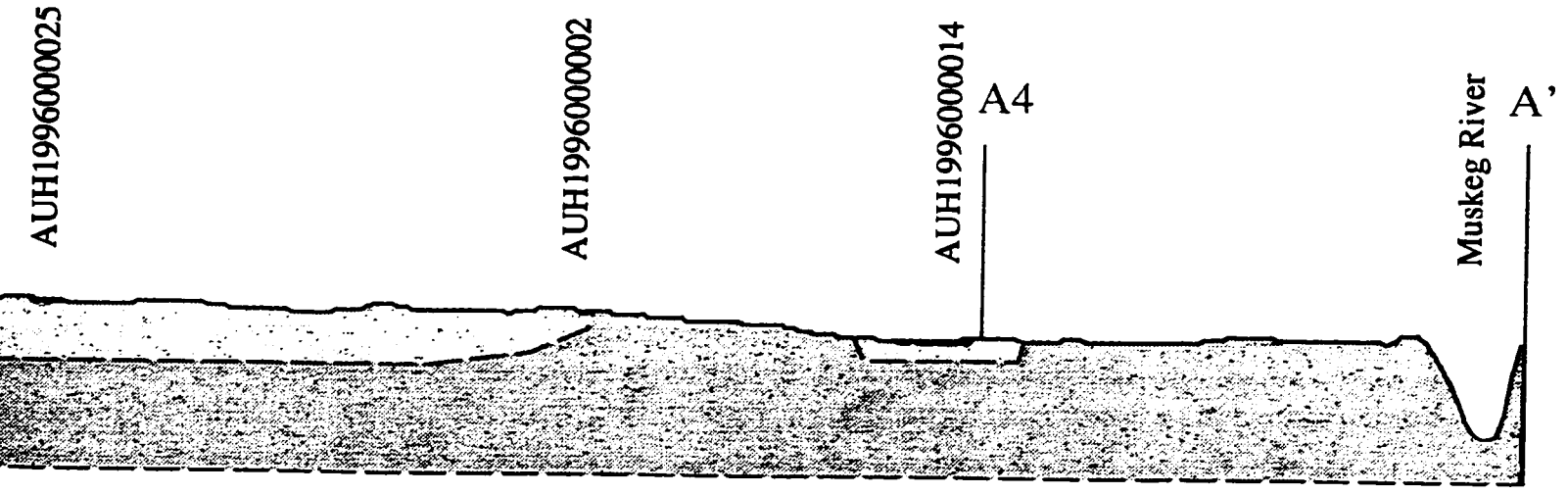

vards the east; vertical exaggeration = 10

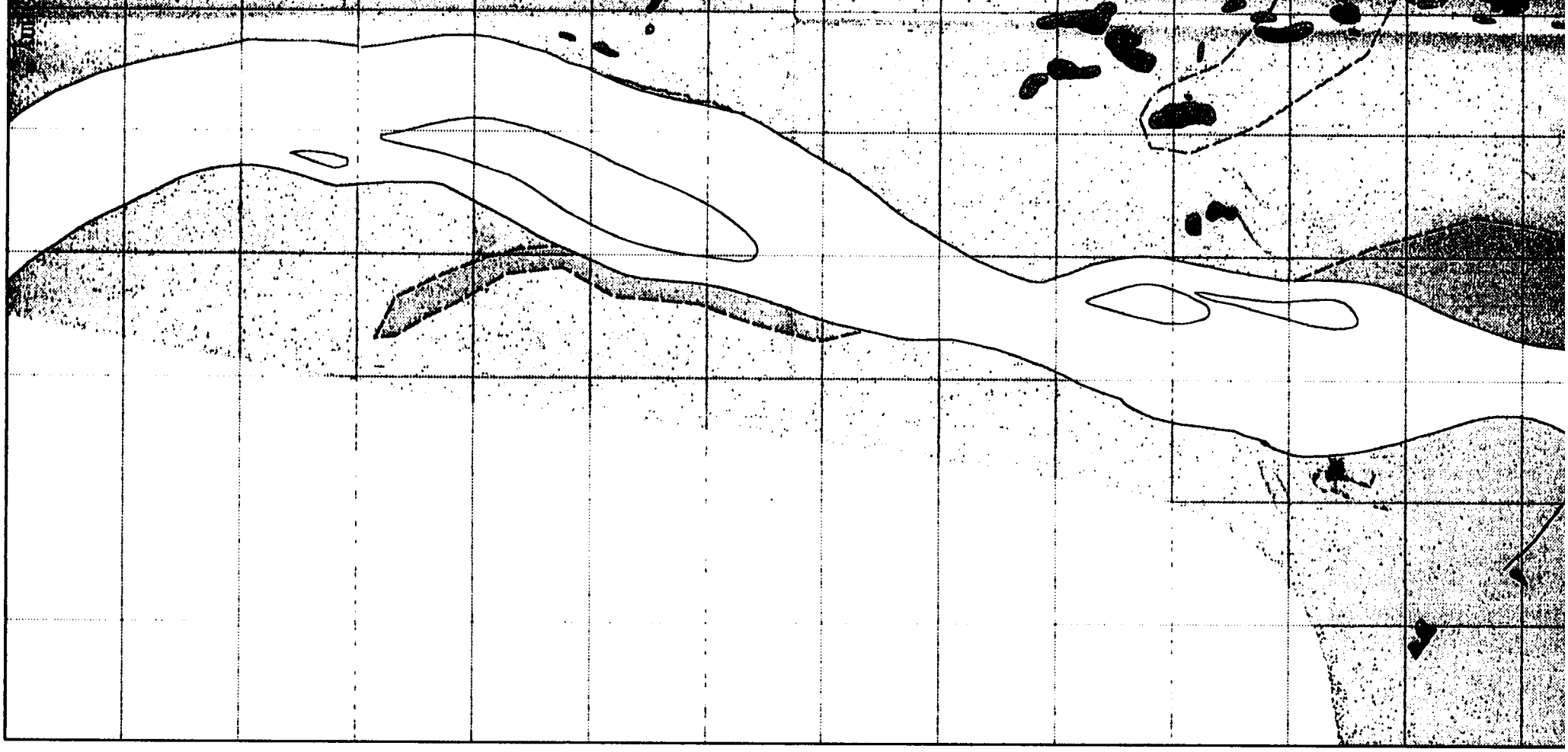

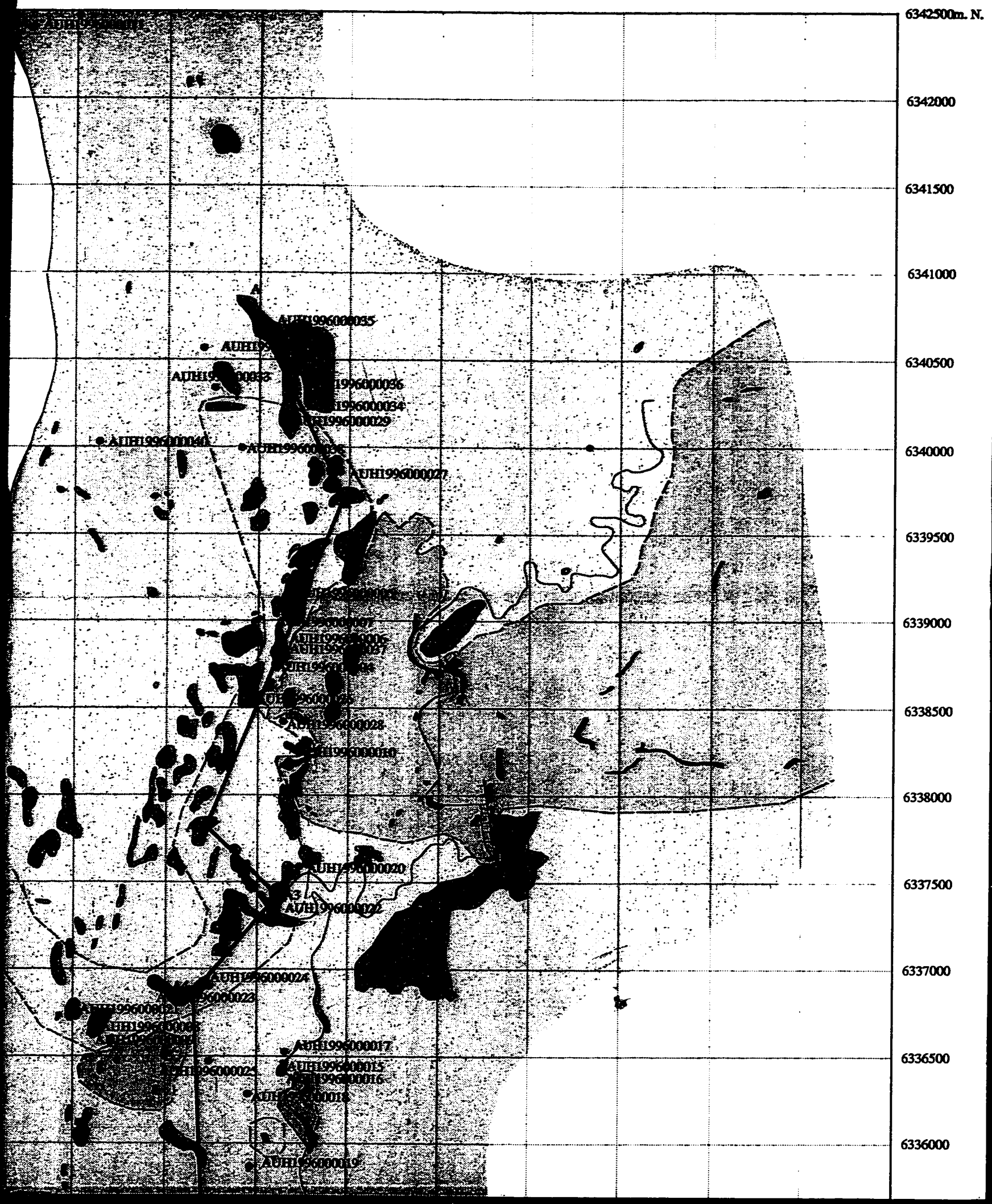
6342500m. N.
6342000
6341500
6341000
6340500
6340000
6339500
6339000
6338500
6338000
6337500
6337000
6336500
6336000
AUH1996000035
AUH1996000036
AUH1996000034
AUH1996000029
AUH1996000027
AUH1996000028
AUH1996000020
AUH1996000024
AUH1996000017
AUH1996000015
AUH1996000016
AUH1996000019

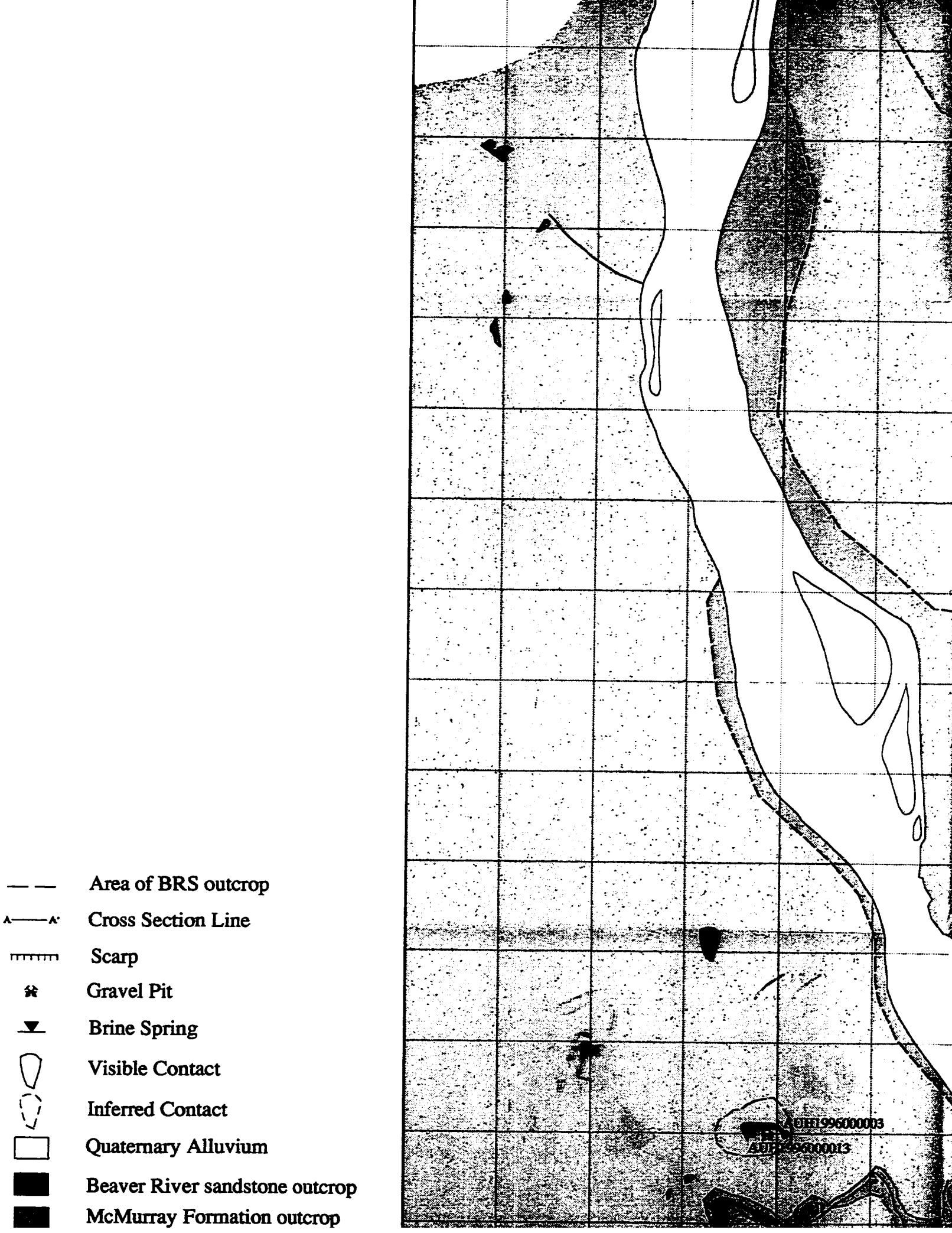
Area of BRS outcrop
A—A' Cross Section Line
Scarp
Gravel Pit
Brine Spring
Visible Contact
Inferred Contact
Quaternary Alluvium
Beaver River sandstone outcrop
McMurray Formation outcrop
AOFI199600003
AOFI199600013


AUH1996000017
AUH1996000015
AUH1996000016
AUH1996000018
AUH1996000019
AUH1996000014
6337500
6337000
6336500
6336000
6335500
6335000
6334500
6334000
6333500
6333000
6332500
6332000
6331500
6331000

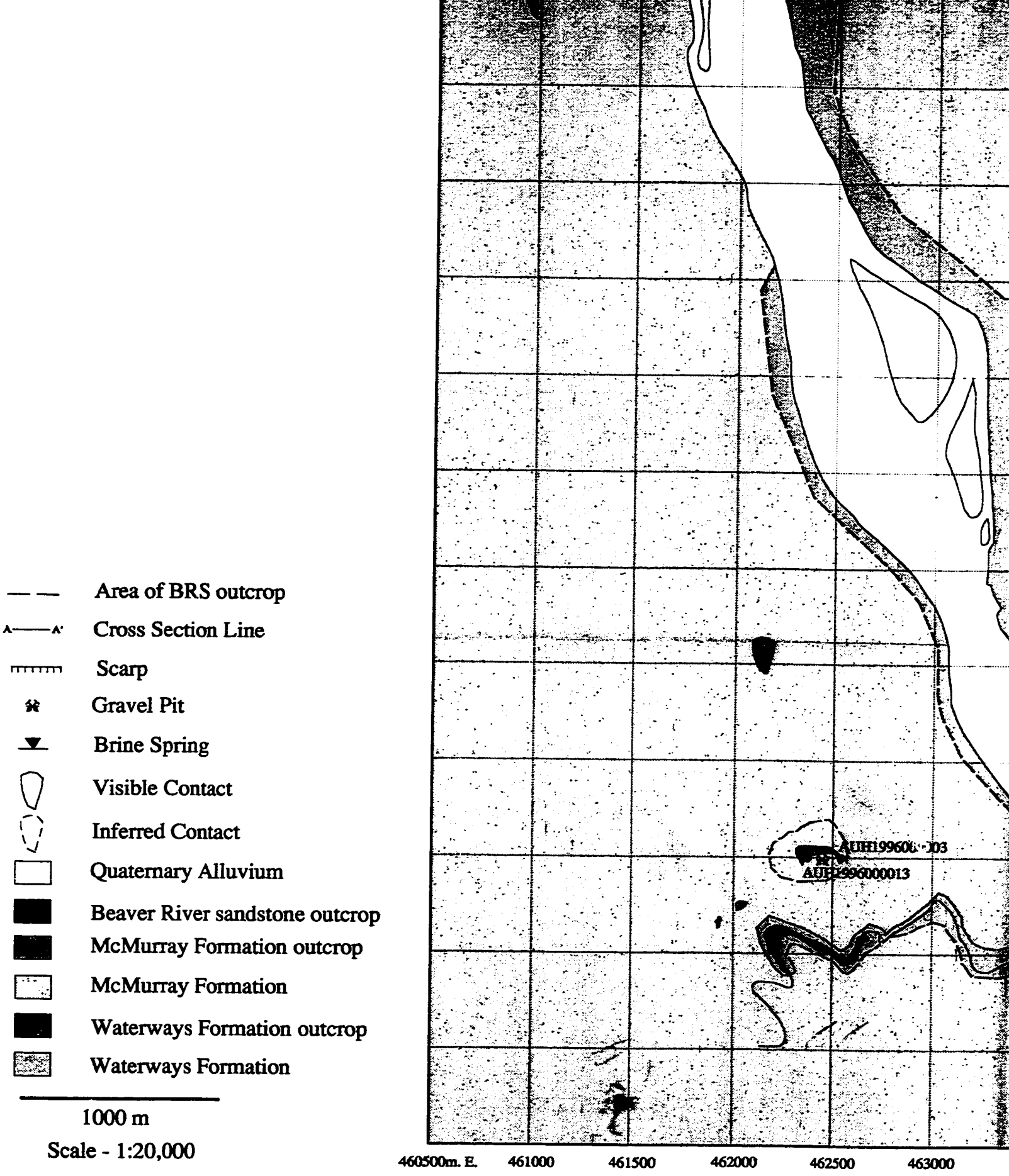

Figure 2.3 Geological map of study area s

Brian Tsang, Department of Ge

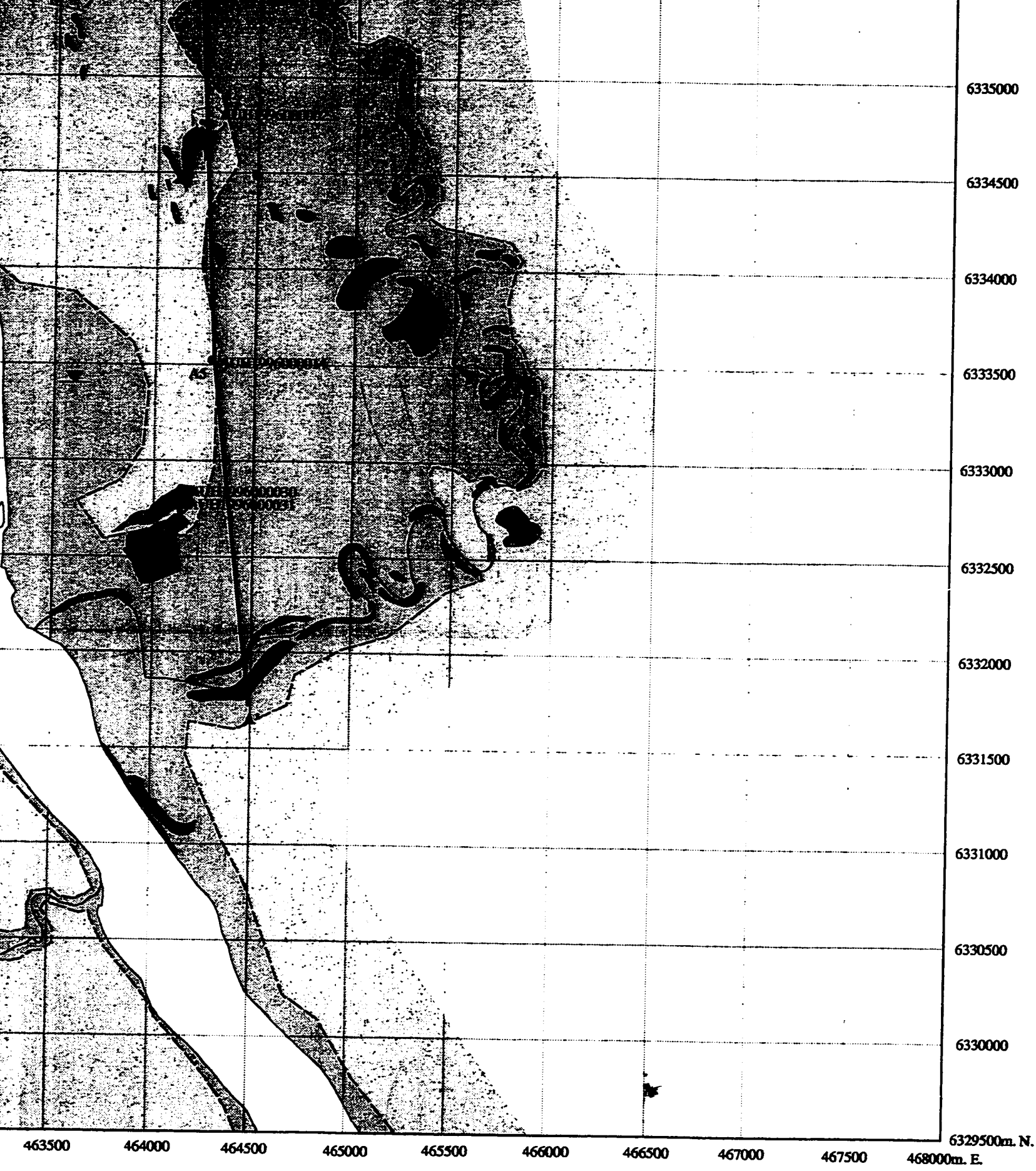

showing sample locations, outcrop positions and cross section lines.
Geology and Geophysics, University of Calgary, 1998.

IMAGE EVALUATION
TEST TARGET (QA-3)

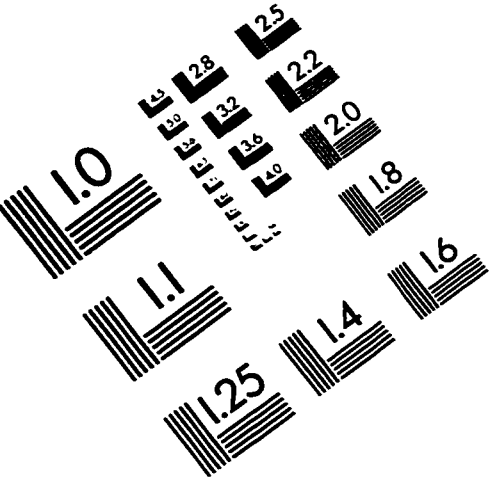

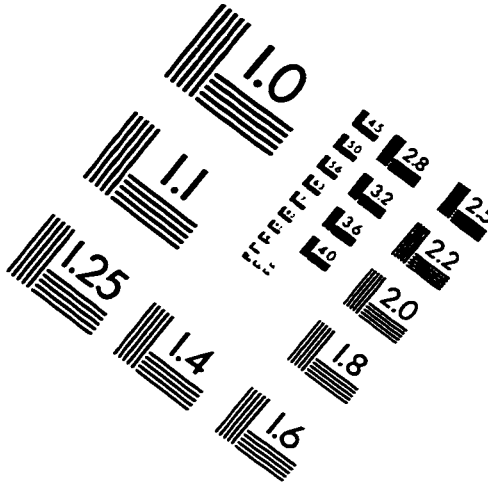

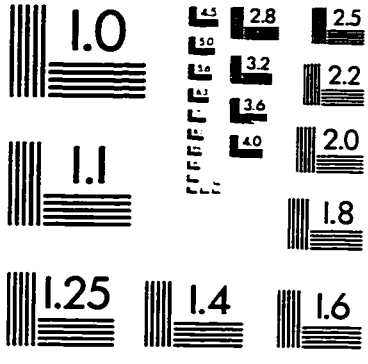

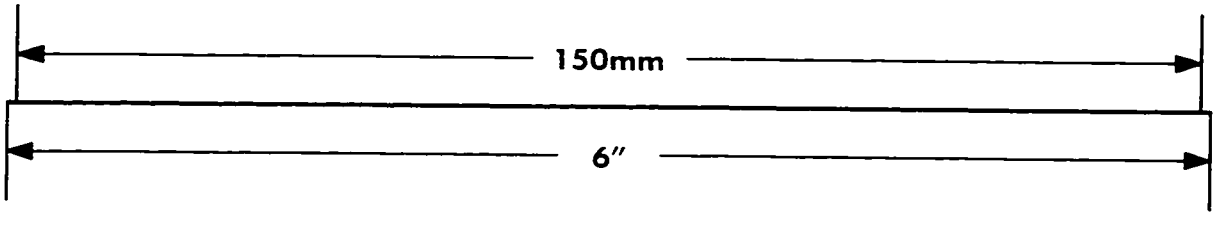

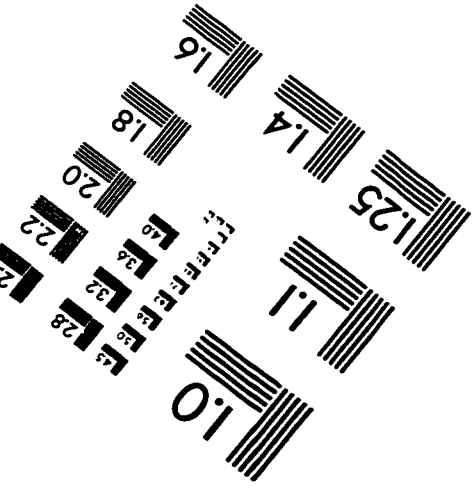

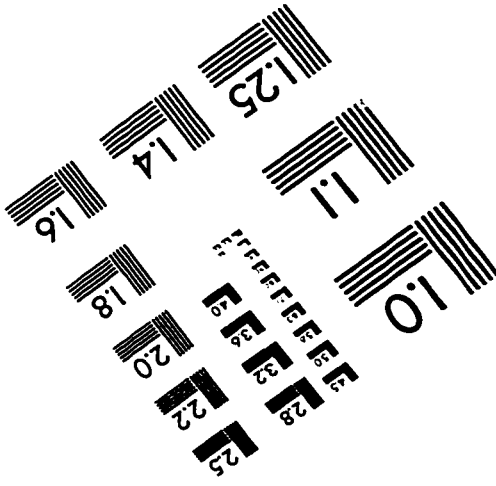

APPLIED IMAGE, Inc
1653 East Main Street
Rochester, NY 14609 USA
Phone: 716/482-0300
Fax: 716/288-5989